Kite Dynamics for Ship Propulsion

George Michael Dadd

A dissertation submitted for the degree of
Doctor of Engineering
at the University of Southampton

Tutors Dr D. Hudson, Prof. A. Shenoi

February 2012
Draft printed on February 26, 2013

Kite Dynamics for Ship Propulsion

George M. Dadd

Kite propulsion has emerged as an attractive means to harness wind power in a way that yields environmental and financial benefits. An understanding of the dynamics that affect kite motion and the resulting forces is required to facilitate the design and optimization of kite propulsion systems.

In this thesis results from two line tension models are compared with experimentally recorded time histories for dynamic kite flight. New methodologies for investigating kite performance are established. The first zero mass model assumes that the kite and lines are weightless. The second, lumped mass model, considers the kites mass and thus makes use of the equations of motion. It is found that the two different models converge to the same result in the limit where the kite mass tends to zero. The zero mass model has been shown to compare favourably with experimental results.

A method for parameterising figure of eight shape kite trajectories and for predicting kite velocity is presented. Results are shown for a variety of manoeuvre shapes, assuming realistic performance characteristics from an experimental test kite. Using a 320m^2 kite, with 300m long flying lines in 6.18ms^{-1} wind, a time averaged propulsive force of 16.7 tons is achievable. A typical kite force polar is presented and a new sensitivity study is carried out to identify the importance of various parameters in the system. Small horizontally orientated figure of eights shape kite trajectories centred on an elevation of 15° are preferred for maximising propulsive benefit. Force is found to be highly sensitive to aspect ratio. Increasing aspect ratio from 4 to 5 is estimated to yield up to 15% more drive force.

Finally, a scheme for synthesising fuel savings due to kite propulsive assistance is developed. This necessitated an investigation of added resistance components and altered propeller and engine performance. The effects of wind speed and ship steaming velocity are established. Slower steaming velocities are favourable to maximising fuel saving benefit. A case study is presented using real ships log data for a 32,000 dead weight ton ship on a North Atlantic voyage. Average fuel saving conditions are established for the year, leading to an estimated fuel savings rate of 2.7 tons per day and a daily return of £1220 at £448 per ton fuel.

PUBLICATIONS

Chapters 3 is based on work published in:
Dadd, G.M., D.A. Hudson and R.A. Shenoi (2010), Comparison of Two Kite Force Models with Experiment, *Journal of Aircraft*, 47 (212-224), DOI: 10.2514/1.44738

Chapter 4 is based on the work published in:
Dadd, G.M., D.A. Hudson and R.A. Shenoi (2011), Determination of kite forces using three-dimensional flight trajectories for ship propulsion, *Renewable Energy*, 36 (2667-2678), doi:10.1016/j.renene.2011.01.027

DECLARATION OF AUTHORSHIP

I, **George M. Dadd** declare that the thesis entitled

Kite Dynamics for Ship Propulsion

and the work presented in the thesis are both my own, and have been generated by me as the result of my own original research. I confirm that:

- this work was done wholly or mainly while in candidature for a research degree at this University;
- where any part of this thesis has previously been submitted for a degree or any other qualification at this University or any other institution, this has been clearly stated;
- where I have consulted the published work of others, this is always clearly attributed;
- where I have quoted from the work of others, the source is always given. With the exception of such quotations, this thesis is entirely my own work;
- I have acknowledged all main sources of help;
- where the thesis is based on work done by myself jointly with others, I have made clear exactly what was done by others and what I have contributed myself;

Signed:

Date:

ACKNOWLEDGEMENTS

I would like to give special thanks to those who have made this thesis possible:

Dr. Dominic Hudson and Professor Ajit Shenoi, who accepted the roles of first and second academic supervisors and who gave their continued support. I am particularly grateful for their patience and freedom granted to borrow time for the months spent in Namibia and for the opportunity to conduct this research.

Dr John Wellicome, for providing the foundation on which this thesis is based and who's intuition on this subject I found to be exceptional.

Malcolm Barnsley, for his wisdom and inspiration, and also to Paul Larsen and Helena Darvelid for showing me the unconventional path to sailing through involvement with their record breaking speed sailing boat, Sailrocket.

Dr. Katy Sheen, Dr. Rachel Nicholls-Lee, Peppy and Graham Dadd who each gave their time to assist in editing.

Terry Webster who offered his expertise and time supervising the machining of various instrumentation components.

Wulfson Unit for Marine Technology and Industrial Aerodynamics (WUMTIA), who were the industrial sponsors for the work and whose staff helped greatly by offering equipment, vehicles, and assistance for developing the instrumentation systems.

Defence Science and Technology Laboratory (DSTL) who commissioned the fuel savings predictions as part of a wider investigation on marine renewables.

Contents

List of Figures

List of Tables

NOMENCLATURE

Notation	Parameter	Units
a	effective aspect ratio (rudder theory)	
A_{BL}	projected area of lines and bridles	[m^2]
A_K	projected kite area	[m^2]
	aspect ratio	[ms^{-2}]
A_R	rudder area	[m^2]
a_K	acceleration	[ms^{-2}]
$\mathbf{C}$	circumferential force, vector	[N]
C	ship course angle (compass axis)	[degrees]
C	circumferential force, magnitude	[N]
$\mathbf{c}$	circumferential force, unit vector	[N]
C_A	horisontal kite force amplifaction factor	
C_{CE}	non dimension centre of effort	
C_D	drag coefficient	
C_{D0}	drag coefficient at $\alpha = 0^\circ$	
C_{Dc}	cross flow drag coefficient	
C_{DBL}	kite line drag coefficient	
C_{DR}	rudder drag coefficient	
C_F	aerodynamic force coefficient (kite dynamics)	
C_F	hydrodynamic friction resistance coefficient	
C_I	Induced resistance coefficient	
C_{IR}	rudder induced drag coefficient	
C_k	chord of kite	[m]
C_L	lift coefficient	
C_{L0}	lift coefficient at $\alpha = 0\circ$	
C_{LR}	rudder lift coeficient	
C_R	ship residuary resistance coeficient	
C_S	hydrodynamic ship sideforce coeficient	
C_T	line tension coefficient (kite dynamics)	
C_T	total resistance coefficient (ship resistance)	
C_X	drive force coefficient	
C_Y	lateral aerodynamic force coefficient	
$\mathbf{D}$	aerodynamic drag force vector	[N]
dt	time step	[s]

Notation	Parameter	Units
D	drag force magnitude	[N]
D	propellor diameter	[m]
D_BL	drag due to bridle and lines	[N]
E	euler rotation matrix	
E	energy	[J]
e	aerodynamic planform efficiency factor	
$\mathbf{f}$	horizontal aero force unit direction vector	[N]
$\mathbf{f_1}, \mathbf{f_2}$	components of f in ship axis	[N]
$\mathbf{F}$	aerodynamic force vector	[N]
F	aerodynamic force vector magnitude	[N]
Fn	Froude number	
F_x	drive force	[N]
F_Y	lateral aerodynamic force	[N]
f, f_2, g	f, g generic functions	
g	acceleration due to gravity (taken as 9.81ms-2)	[ms^{-2}]
H	pole of trajectory sphere	
J	propellor advance ratio	
K_T	propellor thrust coeficient	
KQ	propellor torque coeficient	
L	lift force magnitude	[N]
$\mathbf{L}$	aerodynamic lift force vector	[N]
L	lift magnitude, inclusive of errors	[N]
L	ship water line length	[m]
$\mathbf{l}$	aerodynamic lift force unit vector	[N]
$\mathbf{m}$	vector normal to great circle (left to right sweeps)	[m]
m_1, m_2, m_3	components of vector $\mathbf{m}$	[m]
M_K	lumped mass of kite and bridles	[kg]
$\mathbf{N}$	Net force vector acting on the kite	[kg]
$\mathbf{n}$	vector normal to great circle (right to left sweeps)	[m]
$\mathbf{n_1}, \mathbf{n_2}, \mathbf{n_3}$	components of vector $\mathbf{n}$	[m]
n	exponent	
n	rate of reovolution (propeller theory)	[s^{-1}]
O	orogin of trajectory sphere	
P	Pole of small circle sweep	
P	power	[W]
Q	Pole of small circle sweep	
Q	propeller torque	[Nm]
R	kite position vector magnitude (line length)	[m]
R_F	friction resistance	[N]
$\mathbf{r_0}$	small circle pole position vector	[m]
$\mathbf{R}$	kite position vector	[m]
Re	Reynolds number	
$\mathbf{r}$	kite position unit vector	[m]

Notation	Parameter	Units
S	wetted area	[m^2]
$\mathbf{T}$	line tension vector	[N]
T	traverse time	[s]
T	Thrust (propeller theory)	[N]
$\mathbf{U}$	onset velocity vector	[ms^{-1}]
U	onset velocity magnitude	[ms^{-1}]
U	intersection node on trajectory	
V	intersection node on trajectory	
$\mathbf{v}$	apparent wind velocity unit vector	[ms^{-1}]
V_a	velocity of advance (propellor theory)	[ms^{-1}]
V_A	apparent wind velocity magnitude for kite when static	[ms^{-1}]
$\mathbf{V_ac}$	apparent wind vector (compass axis)	[ms^{-1}]
$\mathbf{V_A}$	apparent wind velocity vector at the static when static	[ms^{-1}]
V_K	kite velocity vector magnitude	[ms^{-1}]
$\mathbf{V_K}$	kite velocity vector	[ms^{-1}]
$\mathbf{V_sc}$	ship velocity vector (compass axis)	[ms^{-1}]
V_S	ship velocity magnitude	[ms^{-1}]
$\mathbf{V_tc}$	true wind vector (compass axis)	[ms^{-1}]
V_T	true wind velocity	[ms^{-1}]
V_{Tref}	reference velocity at altitude	[ms^{-1}]
V_t	true wind vector magnitude	[ms^{-1}]
$\mathbf{w}$	wind unit direction vector	[m]
W	intersection node on trajectory	
X, Y, Z	global Cartesian wind axis system	
x, y, z	x, y, z Cartesian position coordinates	[m]

Notation	Parameter	Units
α	semi-vertex cone angle	[degrees]
α_1	semi-vertex cone angle at P	[degrees]
α_2	semi-vertex cone angle at Q	[degrees]
α	angle of attack	[degrees]
α_e	effective angle of attack	[degrees]
α_k	built-in kite angle of attack	[degrees]
α_t	tangent angle of attack	[degrees]
β	azimuth angle of air onset velocity (kite dynamics)	[degrees]
β	apparent wind angle (ship theory)	[degrees]
δ	variable angle	[degrees]
δ	velocity error	[ms^{-1}]
∂	partial derivative	
γ	elevation angle of air onset velocity	[degrees]
γ_C	true wind angle (compass axis)	[degrees]
ε	aerodynamic drag angle	[degrees]
λ	leeway angle	[degrees]
Λ	rudder sweep angle	[degrees]
θ	elevation angle	[degrees]
μ	substitution variable	
μ	dynamic viscosity of water	
η_1, η_2, η_3	transformation rotation angles about X, Y and Z	[degrees]
η_o	open water propellor efficiency	
Ω	pitch angle of gimballed kite attachment arm	[degrees]
ω	angular velocity	[rad s^{-1}]
ϕ	azimuth angle	[degrees]
ψ	yaw angle of gimbaled kite attachment arm	[degrees]
$_a$	density of air (1.19kgm^{-3}at20$\circ$, 1bar)	[kgm^{-3}]
σ	variable angle	[degrees]
τ	variable angle	[degrees]
υ	kinematic viscosity of air	[m^{2}s^{-1}]
ζ	variable angle	[degrees]

Chapter 1

Introduction

1.1 Background

Kites have hitherto been the subject of a low volume of research for ship propulsion and electric power production, but are now receiving growing interest in view of these commercial applications. Recent developments for ship propulsion, such as in autopilot kite control (Erhard & Struch, 2012) and in launch and recovery systems (Wrage, 2007a) have enabled them to be used commercially for trans-oceanic voyages, yielding financial savings through reduced fuel costs. Alongside yielding financial savings for ship operators, the use of kite power helps minimise the harmful effect that shipping has on the environment. These benefits are achieved using the wind; an entirely renewable energy source which is in abundant supply for a large proportion of the world's oceans. Kites are one method that can be used for capturing this abundant energy supply at altitude. This thesis investigates the performance of kites from a technical perspective, and thus enables the calculation of potential fuel savings, and likely profitability of this type of ship propulsion system. Particular emphasis

is given to obtaining an understanding of the kite dynamics because the literature surrounding this aspect of the wider propulsion problem is relatively sparse.

1.1.1 Aims and Objectives

The aim of the work is to establish a validated mathematical model for evaluating the flight performance of tethered kites when flown around three dimensional trajectories. This is achieved through the following objectives:

- To use a purpose specific test rig to measure static kite flight performance and to record dynamic flight trajectories.
- To predict kite flight performance theoretically using two different mathematical models, and then to compare these with experimental results.

The subsequent aim was enable to prediction of fuel savings during a ship voyage given real ship log data and to evaluate potential fuel savings. This is achieved with the following objectives:

- To combine the validated kite performance prediction model with ship manoeuvring theory.
- to use the model to quantify the fuel saving potential in a variety of different conditions using historic wind data and thus to provide a fuel saving polar diagram.
- to carry out a case study using real ship log data on a particular voyage and calculate the potential fuel savings.
- to establish the potential pay back period for a kite propulsion system from a financial perspective.

1.1.2 Financial incentive

If wind power, either alone or combined with engine power, is to be attractive, it must result in enhanced profitability for the ship owners. The capital outlay must be acceptable, and the period in which the capital investment is recovered through fuel savings must be comparable with other potential investment opportunities available to the ship operators. Since the financial performance of engine propulsion are linked to the price of fuel oil, the attraction of kite power systems, as a way to supplement engine power, is also strongly linked to the price of oil. Oil price is influenced by global supply and demand as well as being affected by political issues and world affairs. At the time of writing, Iran threatens to close the Strait of Hormuz, a channel at the mouth of the Persian Gulf, through which 20% of the worlds oil supply is transported. It is reported that oil prices could increase by up to 50% in a matter of days if the straight were to be closed (TheWeek, 2012). The current price of a barrel of oil is $123.09, which compares to an inflation adjusted price in the year 2000 of $35.88, more than a threefold increase (www.oilprice.com, 2012). Wind power is particularly attractive at times of shipping overcapacity when slow steaming, favourable to wind assistance, becomes the preferred option for ship operators (Crowdy, 1980).

With the introduction of emissions taxes being likely, improved profitability may also be derived through reduced emissions. Schlaak *et al.* (2009) look at the potential world market for the application of kites for wind ship propulsion. They find that international shipping accounts for 2-3% of global CO_2 emissions, 5-7% of SO_2 and 11-13% of NO_X. Technical feasibility allows retrofitting of kite systems to around 60,000 out of a total 90,000 ships. Of these ships, around 24,000 operate at shipping speeds attractive for harnessing wind power using kites Schlaak *et al.* (2009).

1.1.3 Historical perspective

Hobbs (1986) gives an excellent account of historical research on kites. Much of the earlier work was conducted leading up to the invention of the aeroplane (1885-1905).

Further research was undertaken during 1938-1942 when they were developed for use as an aircraft barrage. After the Second World War the parawing kite, designed by Francis Rogallo, was developed for the US space programme. These kites were mainly developed for controlled landings of space capsules. In 1964, the parafoil kite was introduced by Domina Jalbert, having two skins to form an aerodynamic profile and vents close to the leading edge for achieving inflation via leading edge stagnation pressure. Domina Jalbert's parafoil has seen the most significant development, having been used for manned and unmanned flight, dropping cargo from the air as well as use as tethered aerofoils for providing traction for recreational use and for ship propulsion.

Propulsion using kites was first documented in 1827 when George Pockock used them for towing carriages on land. In 1903, S.F Cody was reported to have crossed the English Channel using kites to tow a small dinghy. Bryant & Brown (1942) considered the stability characteristics of kites using stability analysis. After the Second World War, attempts were made to develop an early high performance kite of glider type design but it was commented that ensuring stability became increasingly difficult for kites with higher performance in terms of the lift to drag ratio (L/D). An attempt was also made to build a kite of high efficiency having glider type design. The development of a kite of high efficiency was reckoned to be so formidable a problem that interest in the subject inevitably declined.

In 1982, Ian Day won the world speed sailing record on a boat called Jacobs ladder, achieving 25.03Kts using a stack of Flexifoil recreational kites attached to a tornado catamaran hull. A practical investigation on the use of kites was conducted by Duckworth (1985) at the British Petroleum Research institute. Launch feasibility was proven by demonstration, by firing parachutes into the air using compressed air canisters. Based on these trials, and using a computer simulation, it was found that 7% of fuel could be saved on average. However, the estimated system cost was then £1M and this prohibited further research. Although very large sail areas were considered (25,000m^2 on a 30,000 dead weight ton ship) the propulsive mode was by means of pure aerodynamic drag and the benefits of force amplification due to dynamic kite

flight were not appreciated. In 2001, the German company Skysails was founded by Stephan Wrage and Thomas Meyer who established a kite ship test facility in Wismar. The first commercial ship voyage was completed March 2008 using a 160 square meter kite. The voyage was sailed from Germany to Venezuela, then to the United States and finally to Norway. Whilst the kite was in use, the ship was reported to have saved 10-15% fuel ($1000 to $1500 per day) (www.Skysails.com, 2012). Skysails use a crane for assisting the launch of the kite. Dave Culp, founder of company KiteShip in California, brought the OutLeader rule-legal spinnaker replacement kite to worldwide yachting in 2002 (www.kiteship.com, 2012).

1.1.4 General aspects of a kite propulsion system

The Para foil type kite is most common for traction applications (figure 1.1). The sine wave and the figure of eight shown in figure 1.2 are examples of commonly used dynamic flight manoeuvres. Each manoeuvre provides a different function used for sailing at different angles to the wind. The sine wave employs a vertical up and down motion to maximize propulsive drive when on points of sail close to the wind. When moving, this manoeuvre inscribes a path that resembles a sine wave when viewed in fixed earth coordinates. The figure of eight is suitable for maximising propulsive drive when sailing in a downwind direction. Circular flying motions are typically prohibited due to undesirable twisting of the flying lines.

Significant force amplification arises for dynamic kite flight as a result of the increased onset velocity due to the motion of the kite. The maximum onset velocity is found as the wind velocity at the kite multiplied by a factor approximately equal to the lift to drag ratio, (L/D) (Lloyd, 1980). Thus, with the aerodynamic force increasing with the square of the onset velocity, for a typical L/D ratio equal to five, a

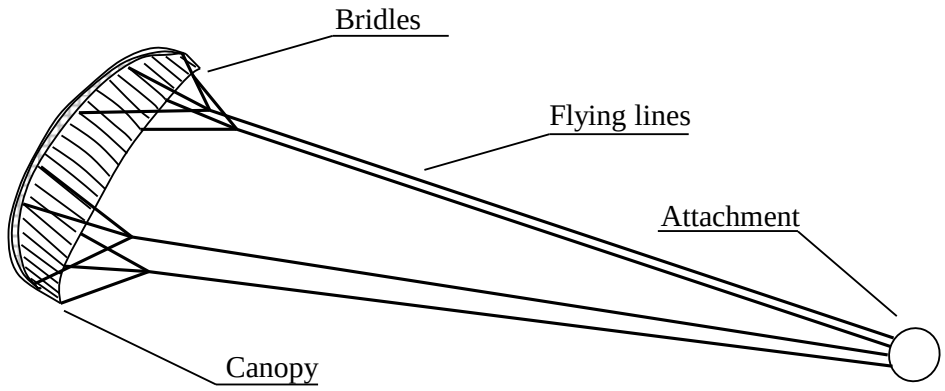

Figure 1.1 Parafoil Kite

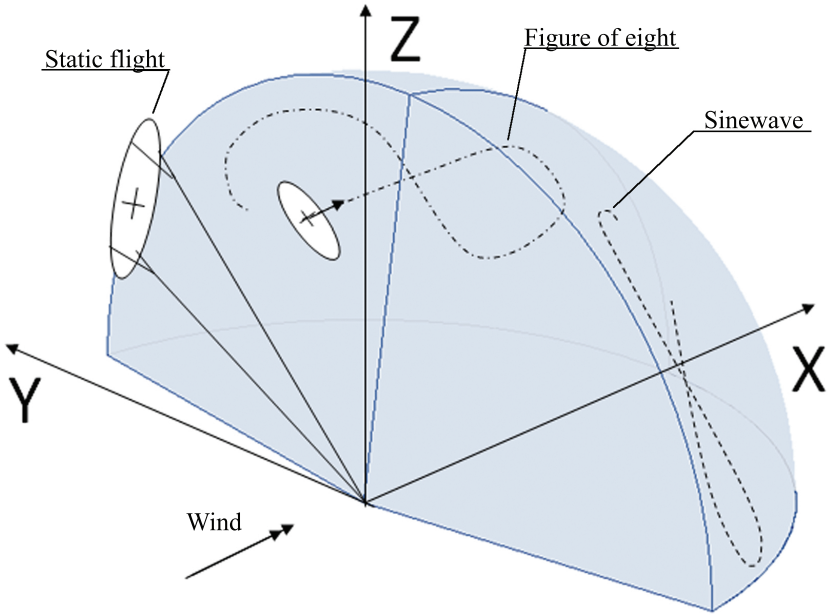

Figure 1.2 FE and example flying manoeuvres

maximum lift force in the order of 25 times that of the static kite or sail is achievable. Because a large component of the kites onset velocity is created in the cross wind direction due to the motion of the kite itself, the kite is able to produce a downwind drive force that is composed predominantly of lift rather than drag.

The kite has significant practical advantages which make its commercial application attractive. Since the line tension acts through its tether at deck level, the heeling moment arm (between the centre of hydrodynamic and aerodynamic centres of effort)

is reduced greatly compared to other conventional sailing rigs. Further, the towing kite may be mounted at the bow (Wrage, 2007a) and does not require a large support structure such as a mast, so can be retrofitted without affecting the existing deck layout or operation. Additional performance benefit can be realised by raising the propulsive kites higher in the atmospheric boundary layer enabling exploitation of stronger winds at altitude. However, for propulsion, this must be traded with a reduced forwards drive force component arising from an increased elevation angle.

There are practical disadvantages to the use of kites that must be avoided if they are to continue successful use on shipping fleets. These difficulties arise primarily with launch and recovery reliability. In particular, excessive bow motions on many ships induce an undesirable vertical wind component that makes it very difficult to maintain steady line tension and this impairs the stability of the kite. The consequences of a crash are uncertain; at the least it would cost the ship operators time to recover the fallen kite, and worse the kite would sustain significant damage and render the system unusable if there is no replacement kite.

1.1.5 Previous Research

Wellicome (1985) compares suitable propulsive devices for wind ship propulsion, including soft sails, high lift aerofoils (with lift coefficient, $C_L \sim 3$), high lift Flettner rotors and kites. In terms of the drive force achievable per unit area, kites were shown to outperform almost all other viable wind propulsion concepts. When a lift coefficient of 0.65 was used, the kite was only outperformed by the high lift aerofoil close to the wind and was shown to be the only device capable of generating large drive force coefficients downwind.

As well as developments in kite assisted ship propulsion, work is also currently ongoing for the generation of electrical power (Lansdorp, 2005; Ockels, 2001; Podgaets & Ockels, 2006; Williams, 2006). Williams (2006) describe a system in which the flying

line rotates a drum as it unwinds driving a generator to create power using the wind. The kite system is modelled as a collection of point masses connected by inelastic rods. Lagranges equations are used to define the system through energy consideration. In the computer simulation, a feedback controller is implemented to follow a reference trajectory. A similar approach is adopted to assess the performance and optimize the flying motions of an alternative kite driven vertical axis generator (Williams *et al.*, 2007a) and also for towing a vehicle in a cross wind direction (Williams *et al.*, 2007b). Further work by Williams *et al.* (2007c) addresses a tracking controller that is numerically implemented to manoeuvre a kite in the presence of gusts. The angle of attack is controlled to maintain a desired tether tension whilst the tether length is varied.

Williams *et al.* (2007d) consider the actuated steering control of an experimental test kite, first using drag flaps, and then via manipulation of the kite line attachment along tracks at the tip of the kite. Preliminary work has also been conducted to model the flexibility of the kite canopy itself by considering it to be two jointed flat plates Williams & Ockels (2007). Ockels (2001) gives consideration to the power production and economic issues associated with a particular design concept for electricity generation. The concept makes use of several kites on a continuous, looped flying line. Research into applications of new materials and kite construction methods is also ongoing. Breukels & Ockels (2007) investigate the application of composites as well as optimizing bridle configurations from a structural perspective for the development of an inflatable kite plane. Jackson (2005) looks specifically at improving kite performance by optimizing the shape and twist distribution using lifting line theory applied to a tensioned kite canopy.

Since kites do not readily lend themselves for testing in a wind tunnel due to prohibitively long flying lines and stability issues at small scale, testing can be most cost effectively conducted at full scale. Alexander & Stevenson (2001a) developed a test rig for measuring kite performance in natural wind that was mounted on the roof of a car. In addition, work has been conducted that examines the force balance for

a kite. For example, the static flying position of the kite can be predicted from its aerodynamic properties (Alexander & Stevenson, 2001b). Stevenson *et al.* (2005) and Stevenson & Alexander (2006) developed a testing method for establishing kite L/D by flying the kite in a complete horizontal circle. These experimental studies focused on static flight performance, rather than on the characteristics of dynamic flight.

Existing dynamic kite models may be distinguished as utilizing two distinct principles; those which are based upon equilibrium between kite forces and line tension (Naaijen & Dallinga, 2006; Wellicome & Wilkinson, 1984) and those which employ Newtons equations of motion (Williams *et al.*, 2007a,b,c,d; Williams & Ockels, 2007). Additionally, a model is described by Schlaak *et al.* (2009) in which the energy extracted from the wind is related to the swept area of the kite and the power density of the wind. The rate of energy extraction is obtained empirically based on experiments with a flown kite. The precise functional relationships are not expressly defined. The model is used to establish estimates of global fuel savings achievable for wind assisted ships on different wind routes. Wellicome & Wilkinson (1984) conducted a purely theoretical study of kite manoeuvring to determine the time-averaged force components when undergoing various flying patterns. By neglecting the influence of mass and by assuming instantaneous equilibrium between the aerodynamic forces and the line tension, it was shown that the onset velocity (U) at the manoeuvred kite can be approximated as a function of the apparent wind at the tether base (V_A) the kite spherical position coordinates (θ, ϕ) and the aerodynamic drag angle (ϵ) using

$$U = V_A \frac{\cos\theta \cos\phi}{\sin\varepsilon} \tag{1.1}$$

The aerodynamic drag angle (ϵ) is the angle subtended between the lift and drag force vectors.

Naaijen & Dallinga (2006) developed a dynamic kite force model for investigating the performance of ships propelled with kites. Under various operating conditions, the potential fuel savings were determined. The dynamic model used the kite position

vector, the true wind and the kite velocity to obtain the onset flow. Then, given the performance in terms of L/D, the kite velocity is determined numerically as that which makes the aerodynamic force vector parallel with the flying lines. The magnitude and direction of the aerodynamic force vector can then be determined. This approach implies instantaneous equilibrium.

A limitation of kite performance models that utilise the equations of motion is that close correlation with real flight performance is difficult to obtain. Perturbations in the natural wind cannot all be accurately represented in a simulation and accumulative drift between the simulated state and the real state is inevitable. Furthermore, in practice, accurately replicating a theoretically defined trajectory is hard to achieve for providing experimental validation through comparison.

However for kite performance models which are based on the principle of instantaneous equilibrium, onset velocity and thus lift force can be analytically established based on kite position (see equation 1.1). Validation by comparison with experimental results can be readily obtained if the kite position relative to the wind, and the wind speed is measured. To date, a dynamic model for predicting time histories of line tension during dynamic flight has not been validated experimentally. The determination of drive forces using a validated kite performance model is required to enable ship velocity prediction, for design, for synthesising fuel savings and for optimising kite systems for the best propulsive effect. In addition, a kite performance model can be used to implement carefully considered kite trajectories for a desired force output.

1.1.6 General aspects of kite propulsion

Lift and drag calculation

In conventional aerodynamics, the lift and drag vectors ($\mathbf{L}$) and ($\mathbf{D}$) are the orthogonal components of the aerodynamic force ($\mathbf{F}$), perpendicular and parallel to the

onset wind velocity (**U**). The magnitudes L and D, are given in terms of the density of air (ρ), the projected area of the kite (A) and the onset wind velocity (U) by

$$L = \frac{1}{2}\rho A U^2 C_L \tag{1.2}$$

$$D = \frac{1}{2}\rho A U^2 C_D \tag{1.3}$$

and expressed in their non-dimensional forms by

$$C_D = \frac{D}{0.5\rho U^2 A} \tag{1.4}$$

$$C_L = \frac{L}{0.5\rho U^2 A}. \tag{1.5}$$

C_L and C_D are the lift and drag coefficients. The magnitude of the line tension or equivalently, the aerodynamic force vector is given and expressed in their non dimensional forms by

$$T^2 = F^2 = D^2 + L^2 \tag{1.6}$$

or

$$C_F = \frac{F}{0.5\rho U^2 A}. \tag{1.7}$$

The aerodynamic lift and drag coefficients are given by expressions of the form

$$C_L = f(\alpha_e, \mathrm{Re}\,.) \tag{1.8}$$

and

$$C_D = g(\alpha_e, \mathrm{Re}). \tag{1.9}$$

The relationship described by equations 1.8 and 1.9 are commonly obtained by experiment, and can be viewed for a variety of wing sections in Abbott & Doenhoff (1959). It is noted that due to changing Reynolds number, the section drag, for example, varies between $cd = 0.0063$ and $cd = 0.0072$ (NACA 4415, $3{\times}10^6$ <Re< $9{\times}10^6$, $cl = 0.4$) where cl and cd are the two dimensional section drag coefficients. With the total three-dimensional kite drag coefficients being in the order of C_D=0.15 (Steven-

son *et al.*, 2005) the influence, of changes in *cd*, on C_D due to changing Reynolds number is relatively minor. Thus, equations 1.8 and 1.9 can reasonably be simplified to $C_L = f(\alpha)$ and $C_D = g(\alpha)$.

Wind velocity components

Various wind components are present in the arguments in this thesis and a discussion of these will help the reader distinguish between them. The true wind velocity, $\mathbf{V_T}$, can be measured directly using an anemometer. The most common reference height for its measurement is 10m. The apparent wind velocity, $\mathbf{V_A}$ is obtained as the vector sum of the true wind, $\mathbf{V_T}$, and the wind due to the motion of the ship, $-\mathbf{V_S}$, see figure 1.3 and equation 1.10. The apparent wind angle β is between the ships track, and the apparent wind. The true wind angle, γ is between the ships track and the true wind.

$$\mathbf{V_A} = \mathbf{V_T} - \mathbf{V_S} \tag{1.10}$$

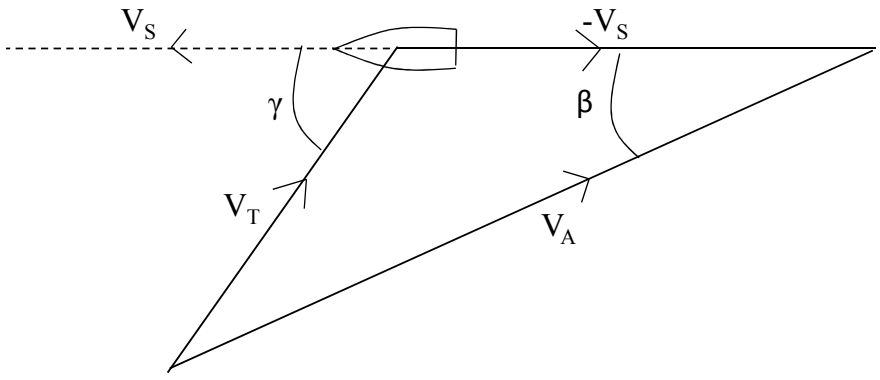

Figure 1.3 Components of apparent wind

In consideration of kite forces, the onset velocity vector $\mathbf{U}$ is used in equations 1.2 to 1.5. This takes into account the apparent wind velocity and a wind component due to the motion of the kite, $(-\mathbf{V_K})$, see equation 1.11.

$$\mathbf{U} = \mathbf{V_A} - \mathbf{V_K} \tag{1.11}$$

It should be noted that when flight tests are conducted on a stationary testing platform, $\mathbf{V_A} = \mathbf{V_T}$. Therefore, to be consistent, the wind experience by the kite system at the tether attachment, at 10m altitude, is always referred to as the apparent wind velocity, irrespective of whether the kite attachment is moving or stationary. It should also be noted that because the kite traverses different altitudes during dynamic flight, a suitable correction should first be applied to $\mathbf{V_A}$ to account for the effect of changing altitude. This altitude corrected apparent wind is referred to as the 'apparent wind at the kite, as though static'.

Forces acting on the kite

Typically in dynamic simulations of moving parts, forces associated with mass play a significant role in the determination of body motions. Examples of these forces dependent on mass include weight, force due to acceleration and centripetal force. In the case of kite motions, aerodynamic forces are commonly an order of magnitude larger than forces due to mass and it may be safe to neglect these completely without significantly impairing the predicted kite motions and resulting line tension. This is implied by equation 1.1 for determining the onset velocity for a moving kite, in which mass is not present. The extent to which it is safe to neglect terms of mass for assessing kite motions is investigated more closely by the work presented in section 3.1, where results are compared, including and excluding mass.

Initially, the forces acting on a kite are considered with terms of mass neglected as shown in figure 1.4. The kite line tension directly opposes the net aerodynamic force such that the system is in force equilibrium. Thus, when zero mass, or equivalently,

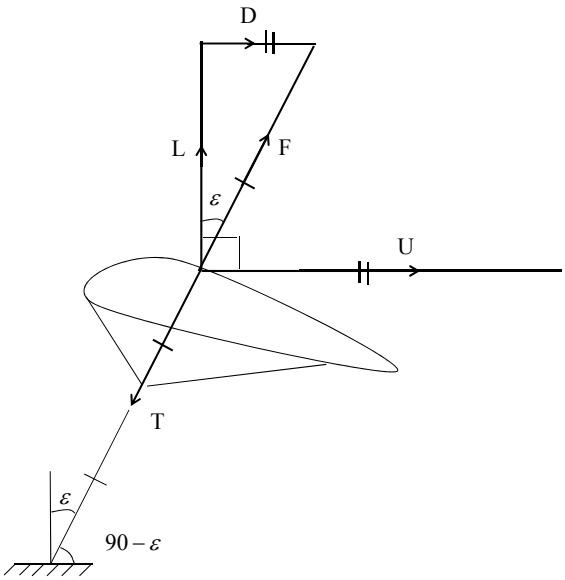

Figure 1.4 Forces acting on the statically flown kite under the assumption of zero mass

instantaneous equilibrium is assumed, the aerodynamic force, **F**, and the line tension vector, **T**, are equal and opposite, as illustrated.

To gain insight into the mechanism of kite flight, one can consider what happens if the kite is not in state of equilibrium. If the aerodynamic force in figure 1.4 swings rearwards the kite decelerates, whilst if the aerodynamic force swings forwards, the kite accelerates. Provided the ratio of lift and drag in figure 1.4 remains constant, the aerodynamic force **F** maintains the same angle relative to the onset velocity, **U**. Thus, the direction of **F**, and hence the acceleration, is directly dependant on the direction of **U**.

In turn, **U** is dependant on $\mathbf{V_K}$, through equation 1.11, such that for a given kite position, and hence for a given orientation of the line tension vector, **T**, there is a particular kite velocity at which force equilibrium occurs. The behaviour of the parameters present in the argument is such that if the kite is below this equilibrium velocity, the aerodynamic force swings forwards and the kite accelerates, whilst if the kite is above this equilibrium velocity the aerodynamic force swings aft and the kite

decelerates.

If, as has been previously stated, the inertia of the system is very low, the kite will be able to accelerate or decelerate almost immediately such that equilibrium is maintained to a very close approximation as the kite traverses a manoeuvre. This hypothesis is exemplified through the mathematical models and results presented in chapter 3.

In figure 1.4, the orthogonal components of F, perpendicular and parallel to the onset velocity **U** are **L** and **D**. The angle subtended between the lift vector and the aerodynamic force vector is the drag angle, ε.

Through vector algebra, $\mathbf{T} + \mathbf{L} = -\mathbf{D}$, such that the lift and the line tension together produce a force which tends to induce kite acceleration forwards. The drag force opposes this and must be overcome if a positive net force, forwards, is to generate kite acceleration during dynamic flight. The L/D ratio, or equivalently the drag angle, is therefore a measure of the kite performance in terms of its ability to generate kite speed.

From geometric considerations in figure 1.4, the drag angle and the L/D ratio are related by

$$\varepsilon = \tan^{-1}\left(\frac{1}{L/D}\right) \tag{1.12}$$

which when combined with equation 1.1, demonstrates that higher L/D results in higher onset velocity, thus improving the lift generating capability. Figure 1.4 also illustrates how the kite performance in terms of its drag angle, and thus L/D, can be measured experimentally. The drag angle is obtained by direct measurement of the angle, $90 - \varepsilon$, when flown statically in the vertical position, or or the left and right side of the wind. L/D is then obtained using equation 1.12. This principle is used in order to obtain the kite performance characteristics during experimental validation.

1.1.7 Structure of the thesis

Chapter 2 describes the development of an experimental test rig and this is used to establish the aerodynamic performance characteristics of an experimental test kite. Methods that are required for recording dyanmic flight time histories are outlined and some preliminary results are presented for a simple dynamic flight manoeuvre.

Chapter 3 presents the derivation for equation 1.1 (Wellicome & Wilkinson, 1984) and this forms the basis of kite performance simulation using the 'zero-mass' model. It was necessary to establish the validity of the assumption of zero-mass and this is achieved by formulating a new kite performance model that includes mass and therefore enables direct comparison. Performance comparisons are made between the zero mass model and experimentally recorded kite trajectories. The limitations and likely errors in the modelling approach are identified. The chapter provides insight into the mechanisms of kite flight using the point mass model and the zero mass model comparisons. It concludes that the use of the zero mass model is suitable for establishing kite force time histories based on equation 1.1.

Chapter 4 describes how theoretical kite trajectories are parameterised by following the work of Wellicome & Wilkinson (1984). Modification to the trajectory parameterisation is made by allowing the trajectories to be systematically varied using Euler rotation matrices. Equation 1.1 only allows determination of onset velocity (and hence line tension) based on kite position, further theory is therefore defined to identify the velocity of the kite its self, and thus to allow the time integration of aerodynamic forces around a predefined trajectory. The time integration of a family of trajectories is carried out to present a new kite force polar. The effects of vertically orientated trajectories compared to horizontal ones are shown together with influence of the increased wind at altitude. A new optimisation study is carried out to assess the importance of kite elevation (θ), kite aspect ratio($\mathcal{AR}$), and kite angle of attack (α_e) on time averaged line tensions. Further experimental tests are used to validate the determination of kite velocity by comparing a purely theoretically defined manoeuvre to that of a similar experimentally recorded one.

Chapter 5 demonstrates the calculation of potential fuel savings using the developed kite performance from chapters 3 and 4. The kite performance is considered for two different kite geometries in order to demonstrate the influence on delivered thrust. A case study is presented for a typical 30,000 dwt ship for determining the potential kite delivered power. The apparent wind due to the motion of the ship and due true wind conditions is considered separately and used as an input into the kite performance model. The effect of the kite on ship resistance is also considered through its influence on induced drag. The chapter also presents the likely effect of additional kite thrust on engine and propeller performance.

Chapter 6 summarises the conclusions of the thesis.

Chapter 2

Experimental Methods for Recording Kite Flight Trajectories

The work outlined in this chapter is based on the masters dissertation thesis by the same author (Dadd, 2005). It details the experimental apparatus, callibration and testing methods used for measuring static kite performance characteristics, C_L and C_D and also for obtaining recorded time histories for line tension and kite position angles during dynamic kite flight.

2.0.8 Apparatus

A system capable of measuring time histories of the full-scale kite force vector during flight is shown in figure 2.1 in a schematic form. Angular displacement transducers (model spectrol 157 manufactured by Vishay) were configured on a gimballed flying arm. The kite was flown from the end of the arm such that it aligned according to the line tension (see figure 2.2). The potentiometers measure the two Euler angles pitch

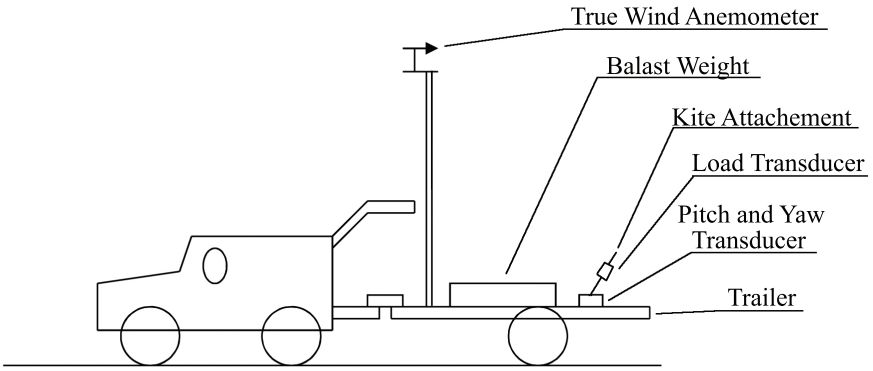

Figure 2.1 Schematic layout of kite testing apparatus

and yaw which are sufficient to define the kite line tension vector orientation and the approximate kite position. The load cell (model serial No 17605762, manufactured by LCM systems) was used to obtain the line tension. It has a rated full range of 98100N with specified accuracy ±0.03%.

The wind velocity transducer (ST40 Rota vector type anemometer, manufactured by Raymarine) was mounted on a 6m aluminum mast in order to minimize the influence of disturbances caused by ground obstructions. It was attached to the trailer via a detachable support and stays were used to improve fixation. The wind velocity signal was damped using a 3 second average period. This was the default setting for the instrument.The apparatus was mounted on a welded support for the instrumented gimbals as shown in figure 2.3.

2.0.9 Data aquisition

The data acquisition system comprised an amplifier, an analog to digital converter (AD card) and a laptop computer, together with data acquisition program Turbo AD WUMTIA (1986). A schematic diagram for the configuration of the acquisition system is shown in figure 2.4. The amplifier (model Modular 600, manufactured by

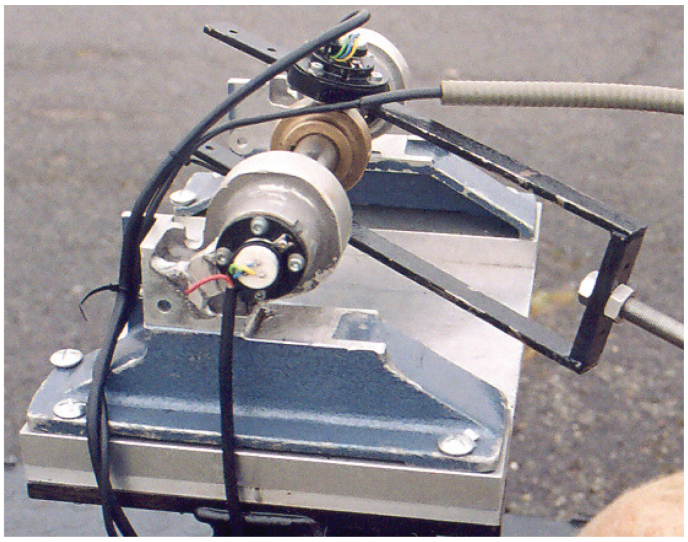

Figure 2.2 gimballed angular displacement transducers, load transducer and kite attachment

Figure 2.3 The towed dynamometer trailer

RDP) has two dual channel sub-units with model numbers RDP-611 and RDP-621. The inverter (model Handy Mains 200 Watt Inverter) was used to convert the car battery voltage from 12 volts to the 240 volts required by the amplifier and the computer.

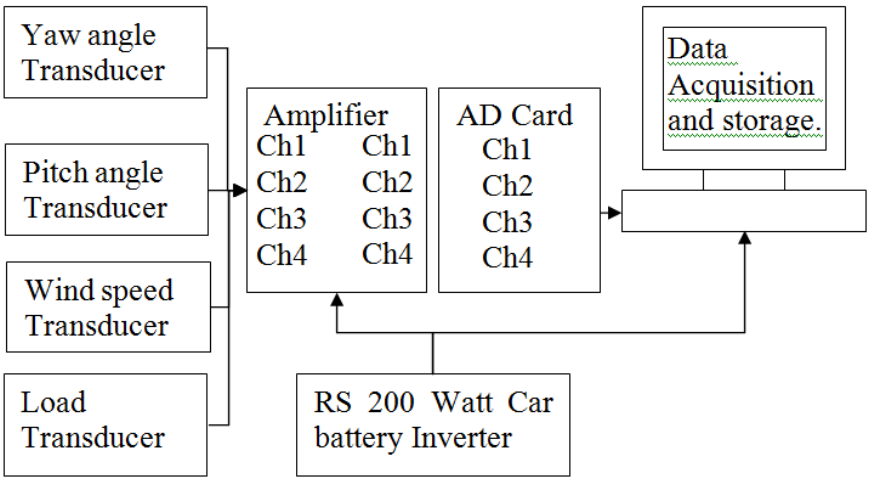

Figure 2.4 Schematic view of data acquisition system.

2.0.10 Calibration

The load cell and the potentiometers were each calibrated independently with the intention of configuring the system so that the best resolution and hence best accuracy could be obtained over the expected range of angles and loads induced by the kite. The calibration procedure, which follows, details in turn the methods used to calibrate the load cell and the potentiometers. Statistical quantities which describe the accuracy of the complete data acquisition system are also given.

2.0.11 Load transducer calibration

The load on the arm was systematically increased using several 20kg hanging masses. To obtain maximal resolution, the amplifier gain and zero settings were adjusted so that the loads ($0 <$ load $<$ 200kg) produce an output ($-5 <$ Volts < 5) that closely matched the full range of the A-D card. Loads are hence discretized into the largest possible number of bits (4096) for maximum resolution. The system is re-zeroed before each test or calibration to offset drift caused by small changes in the

electrical or physical properties of the system. A high value measurement of 180kg is established and the corresponding reading, in bits, is captured using acquisition software. Then a low value measurement of 0kg, is established and the corresponding reading is captured. A 10 second average is used at a capture frequency of 10Hz to remove the introduction of error due to noise. A straight line curve (in the form $Load = rate \times bits + constant$) is fitted to these data points to allow conversion of the recorded data in bits to the desired load.

2.0.12 Angle transducer calibration

Using a similar process to that of the load cell calibration, the amplifier output voltage is adjusted to fall within the usable range of the AD card while using the full range of the potentiometers. The arm is set to its mid position, 0°, using a digital protractor (model PRO 3600), with a resolution of 0.01° . The amplifier zero is adjusted to produce mid-range reading of 2048 bits. The arm is then set to $-90°$ corresponding to its most starboard position. The amplifier gain setting is adjusted to set the correct range. A low value measurement of $-90°$ and a high value of 90° are acquired to complete the calibration. A straight line curve fit is conducted to convert the recorded data in the bits to the desired angle in degrees. Figure 2.5 shows adjustment of the attachement arm using the digital protractor.

2.1 Validation of the measurement system

The results output by the acquisition system are made up of two parts; a portion representing the true value of the measured variable and another, hopefully much smaller portion, representing the combined errors. In order to interpret the results output by the dynamometer, one has to identify the range of values in which the error could lie. A statistical approach is adopted to identify the accuracy with which measurements can be made with a given confidence limit. Validation of the pitch transducer is identical to that of the yaw transducer.

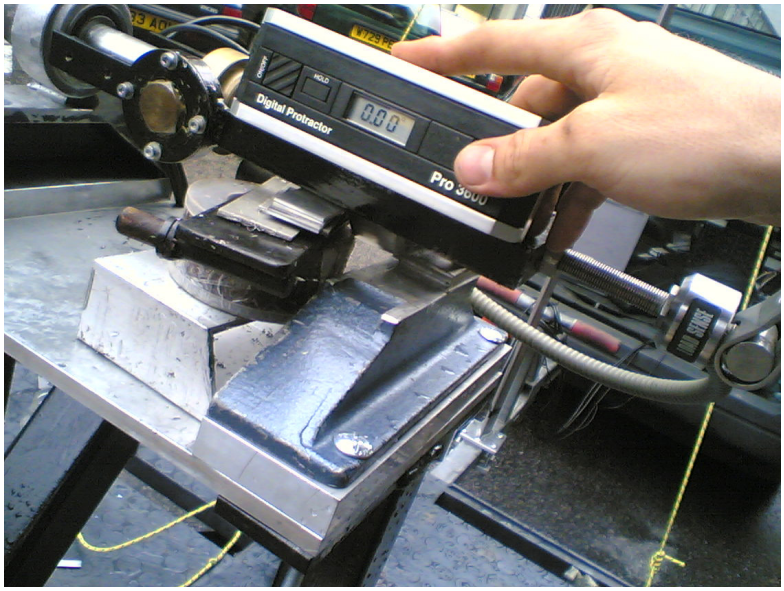

Figure 2.5 A digital inclinometer is used to set the angle of the arm during calibration

Number of samples	60
Mean absolute error	10.1N
Standard deviation	12.3N
95% confidence interval (for one sample)	24.0N
99% confidence interval (for one sample)	31.7N

Table 2.1 Load tranducer measurment statistical values

2.1.1 Load transducer validation

The calibrated dynamometer is used to take a series of measurements of several exactly defined loads. They are systematically increased and decreased using masses between 0kg and 180kg in increments of 20kg. Each sample is obtained for a capture period of 10 seconds, at 10Hz, giving rise to a time-averaged measurement. The process is repeated three times to increase the number of samples to 60 in total. Assuming a normal distribution, the mean and the standard deviations are calculated using standard statistical formulae (Calvert & Farrar, 1999) as well as the 95% and 99% confidence levels. These statistical quantities, presented in table 2.1, illustrate the nature of the spread of values about their mean and hence define the accuracy with which measurements can be made.

Number of samples	375
Mean absolute error	1.11°
Standard deviation	0.673°
95% confidence interval (for one sample)	1.32°
99% confidence interval (for one sample)	1.73°

Table 2.2 Angle transducer accuracy

2.1.2 Angle transducer validation

A procedure similar to that for the load transducer is adopted. A digital inclinometer, accurate to 0.01°, is used to define a range of angles between −90° and 90° at intervals of 45°. At each angle, 25 measurements are taken. The process is repeated three times. Table 2.2, summarises the statistical quantities based on the combined data of all three sets.

2.2 Testing methods

2.2.1 Spatial definition of the flight envelope

The spatial orientation of the flight envelope was established prior to each test in order to orientate the axis system for analysis. To do this, the kite was flown to its starboard most equilibrium position, with one wing tip close to the ground for 10 seconds. This enabled a point on the starboard most edge of the flight envelope to be defined using a time averaged result. The kite was then moved slowly to the zenith position, and then to the port most position, again pausing for 10 seconds. In the analysis of flight trajectories, the downwind axis (X axis) was taken to be the bisector of these vertices since the kite makes the same angle to the wind on both sides of the flight envelope.

2.2.2 Kite Control

Control of the flown kite was achieved manually via steering lines passed through a shackle mounted on the load cell. Care was taken to apply an equal opposing force to the left and right flying lines so the line was fed through the shackle with minimal force, added manually. For figure of eight flights, manual control inputs were only required at the point in each figure of eight in which the direction of turn was reversed since the friction in the system was sufficient to maintain the desired rate of turn. Whilst the control forces are not measured, it is noted that they are small compared to the kite induced loads and thus no correction is applied to the results.

2.2.3 Converting measured gimball angles to cartesian coordinates

The Euler angles output by the gimbaled potentiometers were converted to Cartesian position coordinates using

$$\begin{aligned} x &= R\cos\Omega\cos\Psi \\ y &= R\sin\Psi \\ z &= R\cos\Omega\sin\Psi \end{aligned} \tag{2.1}$$

where Ω is the pitch angle of the first gimballed potentiometer, and Ψ is the yaw angle measured by the second gimballed potentiometer.

The required spherical coordinates (θ, ϕ) were obtained assuming the flying line to be perfectly straight using

$$\phi = tan^{-1}\left(\frac{y}{x}\right) \tag{2.2}$$

$$\theta = tan^{-1}\left(\frac{z}{\sqrt{x^2+y^2}}\right) \tag{2.3}$$

2.3 Test kite particulars

The measured particulars for the test kite (Felifoil Blade III, 3m^2) are shown in table 2.3. The kite planform is shown in figure 2.6.

Table 2.3 Measured kite geometry

Station/m	Chord/m
0	0.86
1	0.78
1.1	0.76
1.2	0.73
1.3	0.70
1.4	0.64
1.5	0.59
1.6	0.49
1.7	0.38
1.8	0.24
1.88	0

Table 2.4 Kite particulars for Flexifoil Blade III 3m

Span	3.8m
Area	2.984 m^2
$\mathcal{AR}$	4.86
Thickness to chord ratio	15%
Line length (4 lines)	28.0m each
bridle configuration total length	41.6m
Bridle and flying line diameter	1mm

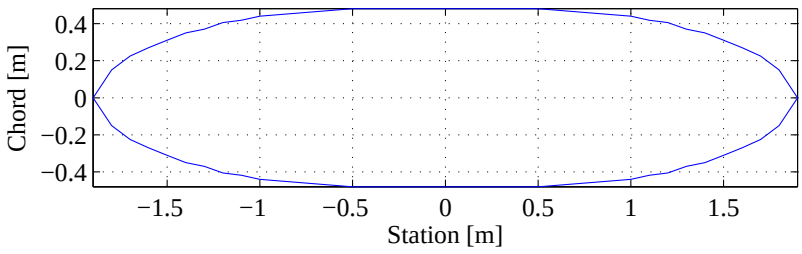

Figure 2.6 kite planform

2.4 Example Results

This sections presents preliminary results acquired using the data acquisition system for a simple flight path. The recorded x, y and z coordinates are plotted in figure 2.7. The flight envelope is also shown, representing the region of the sky in which the kite can be flown, this region is determined using the theory presented in chapter 3. Figure 2.8 shows the spherical position angles θ and ϕ obtained using equation 2.2 and equation 2.3. These values are later used for analysing kite trajectories theoretically. Here, $\theta = 0$ and $\phi = 0$ defines the X axis, parallel to the direction of the wind. θ is the angle of elevation, in the vertical plane and ϕ is the angle of azimuth, in the horizontal plane. The line tension is plotted in figure 2.9 and the measured wind speed is plotted in figure 2.10.

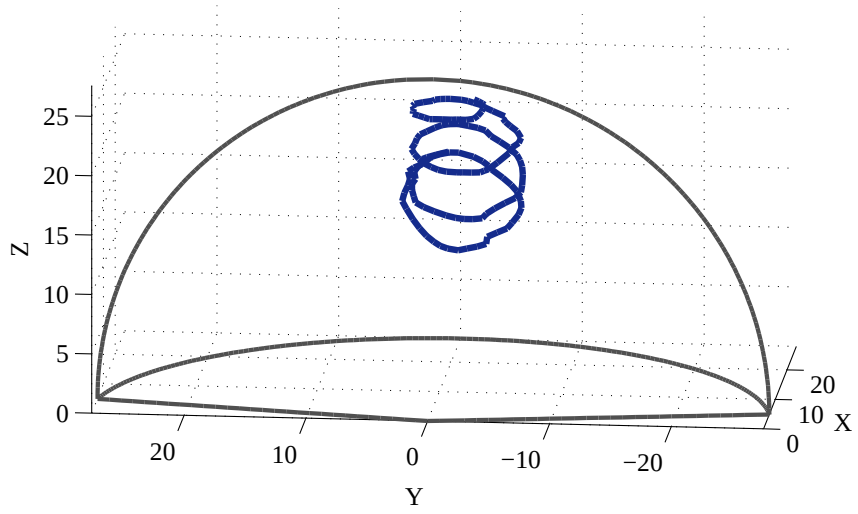

Figure 2.7 Three dimensional position plot for consecutive flown circles.

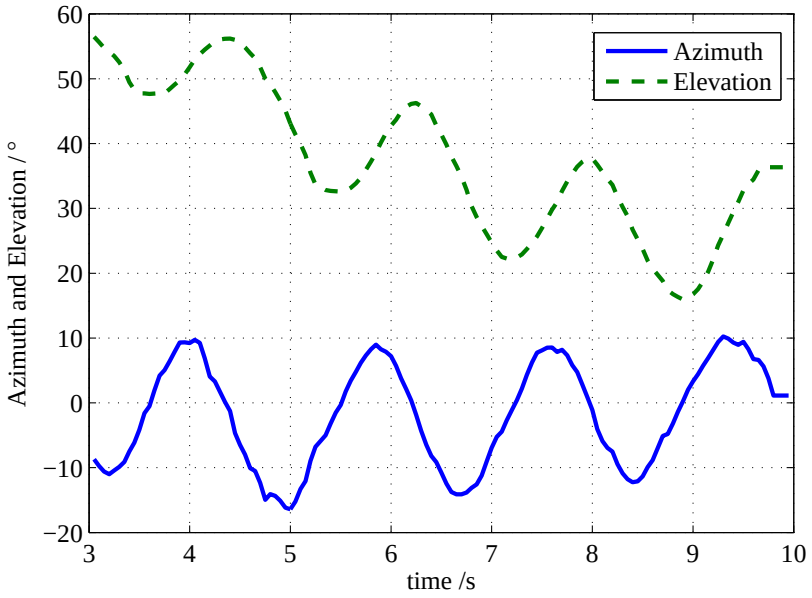

Figure 2.8 Measured Position angles

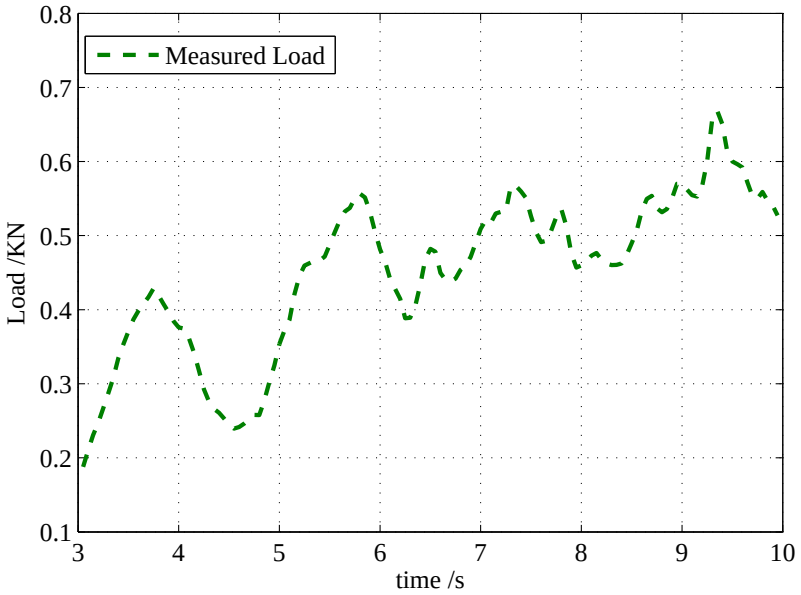

Figure 2.9 Measured line load

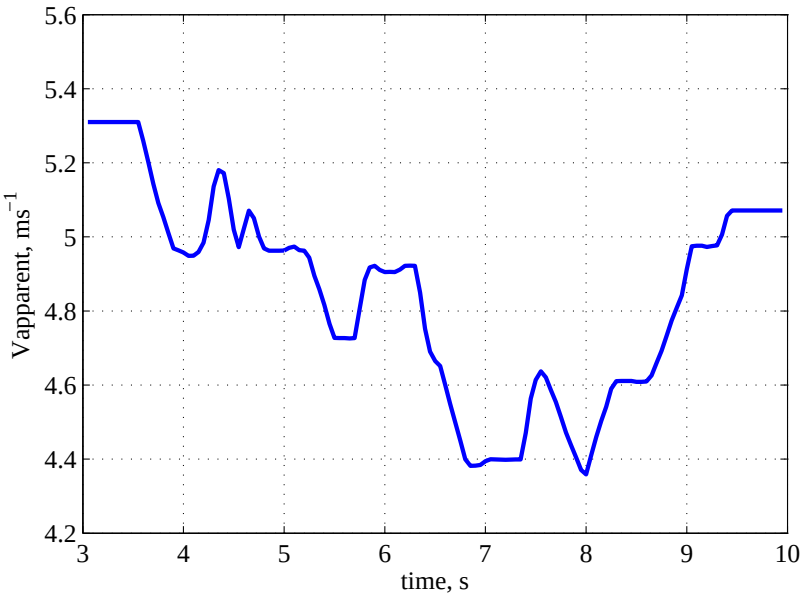

Figure 2.10 Measured wind velocity

2.4.1 Static flight tests

In order to establish the performance characteristics for the kite during static flight, measurements of kite position angles, line tension and wind speed were taken with the kite airborne and stationary. The test rig was towed to maintain an apparent wind of 15 knots, determined using the anemometer display. The flight envelope definition was conducted using artificially created winds, in very light airs, as described in (section 2.2.1). The drag angle, ε was obtained using the recorded position angles and line tension during the wind window defiition. From these data, the drag angle is measured directly (see figure 1.4) using several measurments on the left and the right hand side of the flight envelope. These measurements were used to infer the aerodynamic force vector and thus obtain **L** and **D**. The onset wind velocity magnitude U was obtained directly from the anemometer reading. C_L and C_D were calculated according to equations 1.4 and 1.5 enabling determination of L/D. 21 sample measurments were taken in order to establish the confidence limits. The confidence limits which are computed according to Calvert & Farrar (1999), are shown in appendix A. The 95% confidence interval represents the range in which a subsequent measurment is likely to fall, with a probability of 0.95 and thus provides a measure of the repeatability of the measurement.

Table 2.5 Statically measured performance characteristics for the test kite

	ε	L/D	C_F	C_L	C_D
N samples	21	21	21	21	21
Mean	9.55	6.07	0.78	0.776	0.128
Standard Deviation	1.48	0.88	0.115	0.116	0.012
95% Confidence interval	0.63	0.38	0.049	0.050	0.005
99% Confidence interval	0.83	0.50	0.05	0.065	0.006

2.5 Discussion and conclusions

A system capable of measuring kite position angles, line tension, and wind velocity at the tether has been developed. The use of the system has been demonstrated

by presenting results for a basic manoeuvre. It can be seen that the line tension fluctuates as the kite traverses different regions of the flight envelope. The next chapter investigates how the kite line tension can be predicted. There are limitations of the system and the measurement of kite performance and these are discussed in greater detail in chapter 3. The repeatability of the system for measurements of load and position angles has been established. Load can be measured to $\pm$ 24N with 95% confidence, over a calibrated range of 0 to 1800kN. Position angles can be measured to $\pm$ 1.32° with 95% confidence, over a calibrated range of 180°.

Chapter 3

Comparison of Two Kite force Models With Experiment

In this chapter, theoretical methods for modelling the expected towing line tension for kites are investigated. The aim is to establish whether or not the assumption of zero mass and thus immediate equilibrium can be used effectively to predict kite onset velocity and resulting line tension. This is achieved by comparing the zero mass model of Wellicome & Wilkinson (1984), which does not consider the effect of kite mass on kite motions, to a newly developed model for flight in two dimensions. The new model includes the effect of kite mass. By investigating the influence of mass for a simple case in two dimensions it can be established to what extent the zero mass model might be influenced, in three dimensions by the zero mass assumption.

The subsequent aim is to demonstrate the use of the zero mass model and to provide validation by comparison with experimental results. Comparisons between all three of the point mass model, the zero mass model, and experiment are attempted

simultaneously. The time histories are shown to display similar trends however different results are inevitable due to the use of different aerodynamic characteristic inputs for each of the respective models. Thus, separate comparisons are subsequently made; the first is between the zero mass model and the lumped mass model, with matched aerodynamic performance inputs; The second is between the zero mass model and experiment, with the aerodynamic operating point experimentally derived from static flight performance measurements.

3.1 Mathematical Models

In this section, the zero mass and the lumped mass models are explicitly presented. General aerodynamic concepts pertinent to the current study together with introductory concepts in kite dynamics are also described herein.

3.1.1 Wind Model

In natural conditions, the apparent wind speed at a static kite can fluctuate significantly. Wind statistics can be used to predict the variation in kite performance. At heights of up to 30m, the wind speed tends to fluctuate 10% to 25% of the mean and the variation in the wind direction can be 10° to 15° either side of the mean (Hobbs, 1986). In addition to this spatial variability of the wind, vertical variability is present in the atmospheric boundary layer where the wind velocity is slowed by viscous effects. In the lower atmosphere, the wind speed at height (Z) may be approximated by a power law in terms of the true wind speed (V_{Tref}) at a reference height (Z_{ref}) Claughton *et al.* (1998),

$$V_T = V_{T_{ref}} \left(\frac{Z}{Z_{ref}} \right)^n . \tag{3.1}$$

A typical value for the exponent is n = 1/7.

3.1.2 Zero Mass Model

With a view to providing a simplified model for kite manoeuvring, Wellicome & Wilkinson (1984) formulated the zero-mass analysis. The simplifying assumptions are that;

1. the kite manoeuvres on a spherical surface of constant radius.

2. the kite mass, the cable mass and the cable drag are all negligible.

Since gravitational and inertial forces are neglected and the flying line is assumed to be straight, the aerodynamic kite force ($\mathbf{F}$) and the line tension ($\mathbf{T}$) reach equilibrium instantaneously so that they always remain co-linear. The air onset velocity can be expressed as the vector sum of the apparent wind at kite altitude ($V\mathbf{v}$) and the onset due to the kite velocity ($R\dot{\mathbf{r}}$),

$$\mathbf{U} = U\mathbf{u} = V\mathbf{v} - R\dot{\mathbf{r}}, \tag{3.2}$$

where R, U and V are magnitudes and $\mathbf{r}$, $\mathbf{u}$ and $\mathbf{v}$ are the unit vectors for the kite position, onset velocity and apparent wind velocity at the kite as though static. It is noted that the apparent wind at the kite is equal to the true wind velocity at that altitude if the tether base attachment is not moving. However, it is referred to as an apparent wind velocity because later, further consideration is given to a moving tether attachment such that additional velocity components are added. The aerodynamic force magnitude (figure 1.4) is given by

$$F = L\sec\varepsilon = \frac{1}{2}\rho_a A_K U^2 C_L \sec\varepsilon = \mu U^2, \tag{3.3}$$

the lift force magnitude is given by

$$L = \frac{1}{2}\rho_a A_K U^2 C_L = \mu U^2 \cos\varepsilon, \tag{3.4}$$

and the drag force magnitude is given by

$$D = \frac{1}{2}\rho_a A_K U^2 C_D = \mu U^2 \sin\varepsilon, \tag{3.5}$$

where ρ_a is the density of air, A_K is the kite area and μ is a substitution variable ($\mu = \frac{1}{2}{}_a A_K C_L \sec\epsilon$). By vector addition

$$\mathbf{F} = F\mathbf{r} = L\mathbf{l} + D\mathbf{u}, \tag{3.6}$$

where $\mathbf{l}$ is a unit vector perpendicular to $\mathbf{u}$ so that $\mathbf{l} \bullet \mathbf{u} = 0$. Substituting for F, L and D:

$$\mu U^2 \mathbf{r} = \mu U^2 \cos\varepsilon \mathbf{l} + \mu U^2 \sin\varepsilon \mathbf{u} \tag{3.7}$$

or

$$\mathbf{r} = \mathbf{l} \cos\varepsilon + \mathbf{u} \sin\varepsilon. \tag{3.8}$$

Taking the scalar product with onset unit direction,

$$\mathbf{r} \bullet \mathbf{u} = \mathbf{l} \bullet \mathbf{u} \cos\varepsilon + \mathbf{u} \bullet \mathbf{u} \sin\varepsilon, \tag{3.9}$$

therefore

$$\mathbf{r} \bullet \mathbf{u} = \sin\varepsilon. \tag{3.10}$$

By taking scalar products with the position unit vector, equation 3.2 becomes:

$$U \mathbf{u} \bullet \mathbf{r} = U \sin\varepsilon = V \mathbf{v} \bullet \mathbf{r} - R\dot{\mathbf{r}} \bullet \mathbf{r}. \tag{3.11}$$

Since motion is confined to the surface of a sphere, the kite velocity is tangential to its surface such that $\mathbf{r} \bullet \dot{\mathbf{r}} = 0$. It follows that

$$U = \frac{V \mathbf{v} \bullet \mathbf{r}}{\sin\varepsilon} \tag{3.12}$$

A Cartesian right handed system is chosen with the wind parallel to the X axis. The position angles of $\mathbf{U}$ are β and γ and the position angles of $\mathbf{R}$ are θ and ϕ as shown in figure 3.1. With reference to figure 3.1, the unit vectors $\mathbf{v}$, $\mathbf{r}$ and $\mathbf{u}$ are expressed in terms of their position angles as

$$\begin{aligned} \mathbf{v} &= \{1, 0, 0\} \\ \mathbf{r} &= \{\cos\theta\cos\phi, \cos\theta\sin\phi, \sin\theta\} \\ \mathbf{u} &= \{\cos\gamma\cos\beta, \cos\gamma\sin\beta, \sin\gamma\} \end{aligned} \tag{3.13}$$

$\dot{\mathbf{r}}$ is then obtained by differentiation of $\mathbf{r}$ as

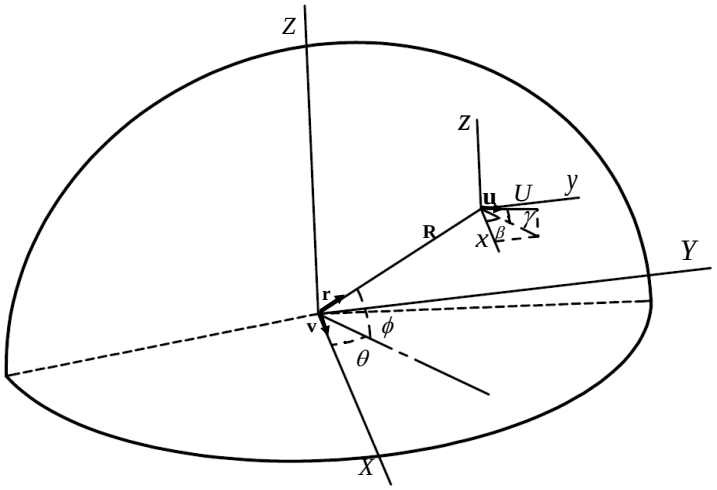

Figure 3.1 Flight envelope showing position angles and onset velocity

$$\dot{\mathbf{r}} = \left\{ -\cos\theta\sin\phi\dot{\phi} - \sin\theta\cos\phi\dot{\theta}, \cos\theta\cos\phi\dot{\phi} - \sin\theta\sin\phi\dot{\theta}, \cos\theta\dot{\theta} \right\}. \tag{3.14}$$

Substituting into equation 3.2 yields

$$\begin{aligned} &U\left\{\cos\gamma\cos\beta, \cos\gamma\sin\beta, \sin\gamma\right\} = \\ &\left\{V + R\cos\theta\sin\phi\dot{\phi} + R\sin\theta\cos\phi\dot{\theta}, R\sin\theta\sin\phi\dot{\theta} - R\cos\theta\cos\phi\dot{\phi}, -R\cos\theta\dot{\theta}\right\} \end{aligned} \tag{3.15}$$

From equation 3.13, $\mathbf{r} \bullet \mathbf{v} = \cos\theta\cos\phi$, such that equation 3.12 can be expressed as

$$U = V_A \frac{\cos\theta\cos\phi}{\sin\varepsilon}, \tag{3.16}$$

which completes the derivation of equation 1.1 introduced in section 1.1.4 (Wellicome & Wilkinson, 1984).

Because **F** and **T** are collinear under the assumption of instantaneous equilibrium, it is implied that L/D is unchanging during dynamic flight. This can be observed in figure 1.4 in which the direction of **F** is seen to depend on **U**, **L** and **D** and hence L/D. By implication, the aerodynamic force coefficients during dynamic flight and static flight are the same and can be established experimentally via static measurement.

The Reynolds number effects that influence C_L and C_D with changing kite velocity are not included in the zero-mass model. If C_L and C_D are known quantities, the aerodynamic lift and drag forces acting on the kite can be determined using equations 1.2 and 1.3 together with the onset velocity U from equation 3.16. The line tension can be established using equation 1.6.

It was considered necessary to examine the validity of the assumption of instantaneous equilibrium and so the alternative lumped mass model was established for investigating kite flight along a two dimensional trajectory. Here, two dimensional refers to a trajectory that remains in one plane.

3.1.3 Two-Dimensional Point Mass Model

The point mass model was developed for comparison to the zero-mass models to establish the effect of including terms of mass. It is based on the equations of motion for a kite and considers the kite as a point mass, located at the end of a flying line. For typical flying line lengths, the weight and the drag acting on the line are negligibly small when compared to the aerodynamic forces acting on the kite. The flying line is therefore assumed to be perfectly straight, and weightless. The net forces acting on the kite are calculated for a known set of aerodynamic characteristics; C_L and L/D for different α and its current aerodynamic state determined by the kite velocity, position and the apparent wind at the kite as though static.

Due to the small kite mass, and the large radius of curvature, centrifugal forces are very small compared to aerodynamic forces and are therefore safely neglected. Similarly, the forces associated with the added mass of air as the kite traverses are also negligibly small in the context of the aerodynamic force and are not considered.

The initial conditions are input by the user. For example, the kite velocity is set to zero, with the kite in the horizontal position, $\theta = 0$, at time $t = 0s$ in natural wind, $V = 10\text{ms}^{-1}$. From these, and knowing the aerodynamic characteristics for the kite the force acting is established. From the calculated net force, an instantaneous acceleration is obtained. This acceleration is assumed to remain constant during a small time step. The resulting velocity and displacement at the end of the time step are calculated. The process is continued until kite motion along a pre-defined flight path is completed.

This process differs from the zero-mass model as it determines the outputs as a function of time and current aerodynamic state, rather than solely a function of position. The aerodynamic force is not assumed to remain collinear with the line tension under the assumption of instantaneous equilibrium. Instead, kite motion is freely determined and the resulting angle of attack and the corresponding C_L and C_D are established at each time step. In the zero mass model, these parameters are fixed at their static flight values. The forces acting in the lumped mass model are shown in figure 3.2a). These include the line tension ($\mathbf{T}$), the aerodynamic force ($\mathbf{F_A}$), the weight ($M\mathbf{g}$), the force due to acceleration (M_a). The flight envelope (FE) which determines the limiting positions of the kite during practical flight, is also shown in the figure. It should be noted that $\mathbf{F_A}$ is the resultant of $\mathbf{L}$ and $\mathbf{D}$.

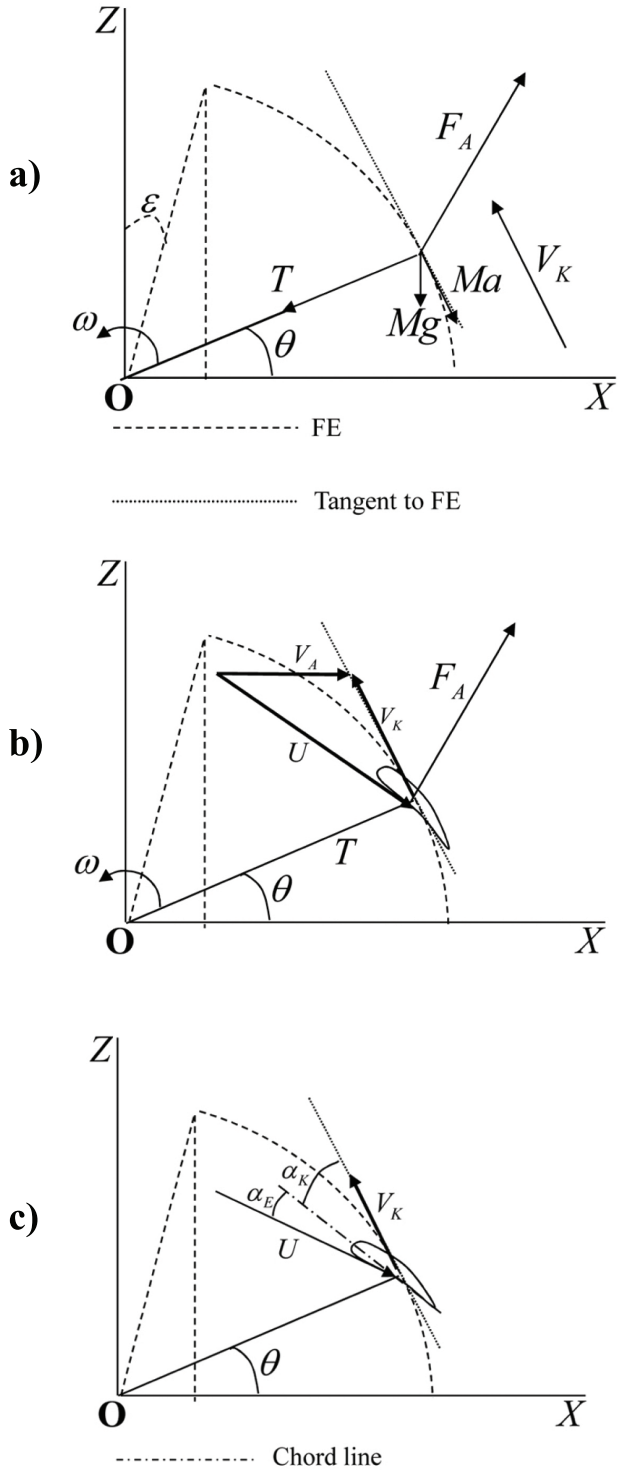

Figure 3.2 Parameters in the lumped mass model: a) forces, b) velocity components; and c) components of angle of attack

Figure 3.2b) shows the wind velocity components $\mathbf{U}$, $\mathbf{V_A}$ and the kite velocity $\mathbf{V_K}$. Figure 3.2c) shows the effective angle of attack (α_e) subtended between the kite chord line and the onset velocity $\mathbf{U}$. The angle subtended between the kite chord line and the kite velocity vector is called the built-in angle of attack (α_K). This angle is a known geometric constant that is later determined photographically for an experimental test kite. It is dependant on the way that the kite is mounted to the flying lines. The velocity vector is tangent to the circumferential path. The kite velocity is

$$\mathbf{V_k} = R\dot{\mathbf{r}} \tag{3.17}$$

The kite position unit vector, $\mathbf{r}$ is

$$\mathbf{r} = (\cos\theta, \sin\theta) \tag{3.18}$$

The onset velocity is

$$\mathbf{U} = \mathbf{V_A} - \mathbf{V_K} \tag{3.19}$$

By taking the dot product of $\mathbf{U}$ and $\mathbf{V_K}$, the angle subtended between them ($\alpha_K + \alpha_E$) can be established.

$$\mathbf{U} \bullet \mathbf{V_K} = -UV_K \cos(\alpha_e + \alpha_K) \tag{3.20}$$

therefore

$$\alpha_e = \cos^{-1}\left(-\frac{\mathbf{U}\bullet\mathbf{V_K}}{UV_K}\right) - \alpha_k. \tag{3.21}$$

The lift and drag coefficients, C_L and C_D are obtained as

$$C_L = f(\alpha_e, \mathrm{Re}) \tag{3.22}$$

and

$$C_D = g(\alpha_e, \mathrm{Re}) \tag{3.23}$$

where f and g are properties of a given kite geometry and may, for example, be

obtained from wind tunnel experiments. The lift and drag force magnitudes are

$$L = qC_L A_K \tag{3.24}$$

and

$$D = qC_D A_K \tag{3.25}$$

where $q = \frac{1}{2}\rho U^2$. The weight of the kite is

$$\mathbf{W} = M_K \mathbf{g} \tag{3.26}$$

The net force acting on the kite is given by

$$\mathbf{N} = \mathbf{L} + \mathbf{D} + \mathbf{W} \tag{3.27}$$

The kite line is incapable of supporting any bending moment or shear force. It is assumed to have zero weight and drag such that it adopts a straight line form. Therefore line tension $\mathbf{T}$ only reacts the radial components of the net force $\mathbf{N}$. The circumferential components of the net force lead to the acceleration of the kite. The line tension is given by the projection of the net force onto the radial direction as

$$\mathbf{T} = T\mathbf{r} = (\mathbf{N} \bullet \mathbf{r})\,\mathbf{r} \tag{3.28}$$

The circumferential component of net force has a unit direction vector at right angles to the position vector given by

$$\mathbf{c} = \begin{pmatrix} 0 & 1 \\ -1 & 0 \end{pmatrix} \mathbf{r} \tag{3.29}$$

The magnitude of the circumferential component is equal to the projection of the net force onto the circumferential direction, given by

$$C = \mathbf{N} \cdot \mathbf{c} \tag{3.30}$$

The circumferential force is thus

$$\mathbf{C} = C\mathbf{c} \tag{3.31}$$

The linear acceleration is obtained using Newtons second law of motion as

$$\mathbf{a} = \frac{\mathbf{C}}{M_K} \tag{3.32}$$

The angular acceleration is

$$\dot{\omega} = \frac{C}{M_K R} \tag{3.33}$$

The new angular velocity after time step, Δt is obtained using a first order integration approach.

$$\omega_n = \omega_{(n-1)} + \dot{\omega}_{(n-1)}\Delta t \tag{3.34}$$

The new linear kite velocity is

$$V_{K(n)} = \omega_{K(n)} R \tag{3.35}$$

The new elevation is

$$\theta_{(n)} = \theta_{(n-1)} + \omega_{(n-1)}\Delta t \tag{3.36}$$

The preceding formulation is sufficient to define the kite performance for a given instant in time along a straight line flight path in the vertical plane. This model does not therefore permit the determination of kite forces along more complicated figure of eight trajectories. Predictions for straight flight are sufficient to enable comparisons to be made with the zero mass model, and for comparison with experimental results, provided that the recorded flight trajectory also closely approximates a straight path. In practice, traversing a kite along a straight line can be difficult to achieve.

Once the lumped mass model simulation has converged to a condition of static flight, the static flight kite opperating point can be obtained. This occurs when the kite has come to rest at the edge of the flight envelope.

The point mass model makes use of a first order forwards integration scheme (equation 3.34). This has been shown to be suitable provided that the time step is small. For example, changing the time step from 0.02 to 0.01 seconds is seen to have negligable influence on the output results.

3.2 Implementation of theoretical models

3.2.1 Zero mass model implementation

Prediction of kite onset velocity using the zero-mass model was calculated using equations 3.2 to 3.16. Lift, drag and hence line tension were then obtained using equations 1.2 through 1.6. The calculation required the provision of a series of instantaneous kite position angles, around a prescribed manoeuvre. For a purely theoretical study, the flight paths could have been selected arbitrarily. In the present study, the process was implemented using real recorded kite flight paths so that the experimental results could be directly compared. It should be noted that where results are plotted with time on the abscissa, the time is established according to the experimentally recorded results. This is to say that the theretical determination of kite line tensions plotted with time is not yet feasible with the theory presented so far. This is later developed in chapter 4.

3.2.2 Lumped mass model implementation

A flow chart describing the implementation of the lumped mass model is shown in figure 3.3. It follows equations 3.17 through 3.36. This process was implemented for a simple two-dimensional manoeuvre using different values for the kite mass, thus allowing the implications of the zero-mass assumption to be assessed through direct comparison of the two models.

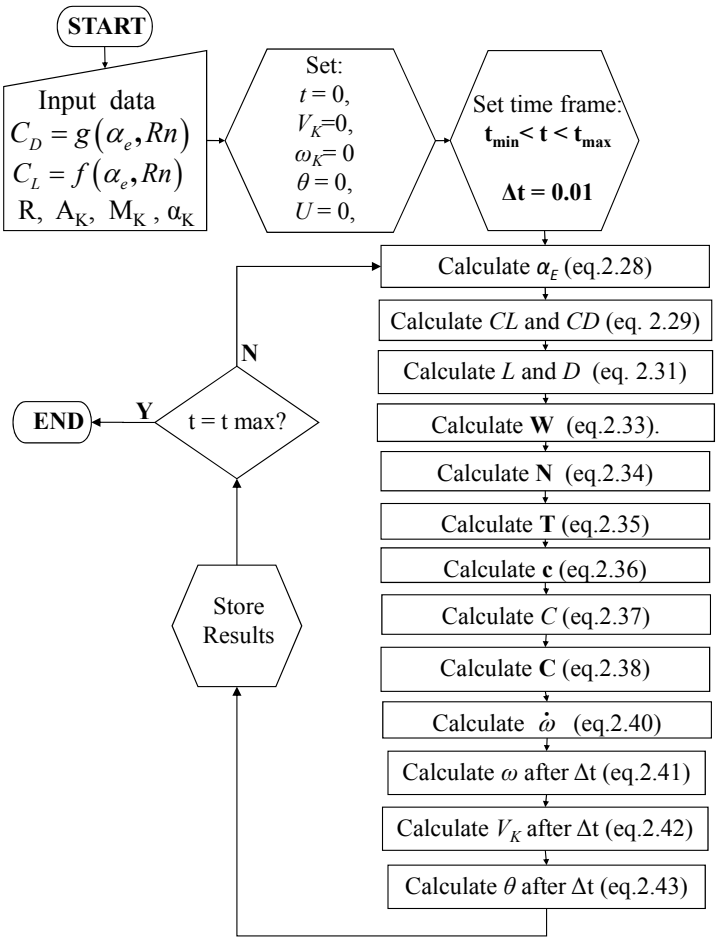

Figure 3.3 Flow chart for lumped mass model implementation

In practical flight, a hot launch manoeuvre satisfies the requirements for flight along a straight path in a vertical plane. The kite is positioned directly downwind facing upwards and is flown directly towards the zenith position. This simple manoeuvre may also be replicated experimentally with relative ease.

The built-in angle of attack, in figure 1.4, was obtained photographically for the current test kite by taking a side view of the un-deformed kite when inflated by the natural wind (fig. 3.4). It was determined by measuring the angle between the tensioned flying lines and the chord using MATLAB plotting tools (Mathworks, 2009). The leading edge and a point on the trailing edge were used as reference points for the chord line.

Figure 3.4 Illustration of measurment of built-in angle of attack

To determine the variation of the lift and drag coefficients with angle of attack, flight performance characteristics of the experimental test kite (Flexifoil Blade III, 3m^2) were required, as described by equation 3.22 and 3.23, for C_L , C_D and L/D to be obtained for any α_e, by means of a look-up table. The compliant nature of foil kites makes testing at different angles of attack in a wind tunnel problematic, thus in the absence of such data for the test kite, an approximation was derived using experimental results (Tangler, 1984) for a NACA 4415 foil section. This foil was selected to closely match that of the test kite and furthermore, the experimental results satisfied the unusual requirement that the performance data be known for very large effective angles of attack, up to deep stall. This was required because initially, the kite is presented to the wind in deeply stalled condition.

It is important to note that by developing an aproximate or assumed lift and drag polar to represent the performance of the kite, it is not expected that results will exactly match experimental flight trajectories. However, it will be possible to investigate the behaviour of the individual parameters during a dynamic flight trajectory and to compare the broard trends with an experimentally recorded trajectory. Separately, it will be possible to make comparisons between the lumped mass model and the zero mass model. The static flight performance parameters are changed from the experimental values to reflect those of the point mass model with the assumed lift and drag polars.

Significant factors that influence the point mass polar diagrams for C_L and C_D are included, namely the effect of modified aspect ratio and the inclusion of bridle line drag.

The following paragraphs describe the adjustments that were made to the NACA 4415 lift and drag data in order to create the aproximated lift and drag polars for the test kite.

The experimental test kite is relatively flat and as such, no correction has been applied to account for the curvature. The relative importance of the line drag in the overall balance of forces is small and as such has not been included. However, since the bridles are numerous, and located at the kite such that the onset velocity is amplified by the motion of the kite their contribution to drag has been included.

The data (Tangler, 1984) were presented for an aspect ratio of 6; therefore a correction was made to adjust the data for the experimental test kite with an aspect ratio of 4.86 using equations 3.37 and 3.38 (Abbott & Doenhoff, 1959).

$$C_D^{'} = C_D + \frac{C_L^2}{\pi}\left(\frac{1}{AR' - \frac{1}{AR}}\right) \tag{3.37}$$

$$\alpha^{'} = \alpha + \frac{C_L}{\pi}\left(\frac{1}{AR' - \frac{1}{AR}}\right) \tag{3.38}$$

These equations correspond, respectively, to the drag coefficient and angle of attack (radians) of a wing of aspect ratio $AR^{'}$. A further correction to the NACA 4415 performance data was made to account for bridle line drag. It was assumed that during dynamic flight, the onset velocity remained approximately normal to the bridle lines, such that the drag can be expressed as

$$D_{BL} = \frac{1}{2}\rho U^2 A_{BL} C_{D_{BL}} \tag{3.39}$$

The drag coefficient of a cylinder of infinite aspect ratio is taken to be 1.2 (Hoerner, 1965). The combined drag coefficient for the NACA 4415 foil together with the

lines and bridle was approximated by equation 3.40. Subscripts BL and K denote parameters corresponding to the bridle lines and kite respectively.

$$C_D = \frac{(A_{BL}C_{D_{BL}} + A_K C_{D_K})}{A_K} \tag{3.40}$$

The modifications described by equations 3.37 through 3.40 were applied to the experimental aerofoil data from Tangler (1984) to derive the assumed kite performance characteristics shown in table 3.1. The assumed flight performance characteristics in table 3.1 are shown together with the original data in figure 3.5 for angles up to 25°.

Table 3.1 Assumed kite performance characteristics

$\alpha_e[^\circ]$	C_D	C_L	L/D	$\epsilon[^\circ]$
-5	0.051	-0.00	-0.358	10.2
0	0.067	0.337	4.864	14.3
5	0.086	0.692	8.015	7.2
10	0.117	0.939	7.991	7.1
15	0.158	1.137	7.292	7.9
20	0.231	1.147	5.132	11.6
25	0.341	0.893	2.746	21.3
30	0.497	0.789	1.614	32.2
35	0.611	0.770	1.263	38.4
40	0.712	0.735	1.035	44.1
45	0.812	0.701	0.867	49.1
50	0.914	0.686	0.752	53.1
55	1.010	0.635	0.631	57.8
60	1.102	0.552	0.501	63.4
5	1.176	0.455	0.388	8.9
70	1.244	0.349	0.281	74.3
75	1.295	0.223	0.173	80.2
80	1.333	0.080	0.061	86.6

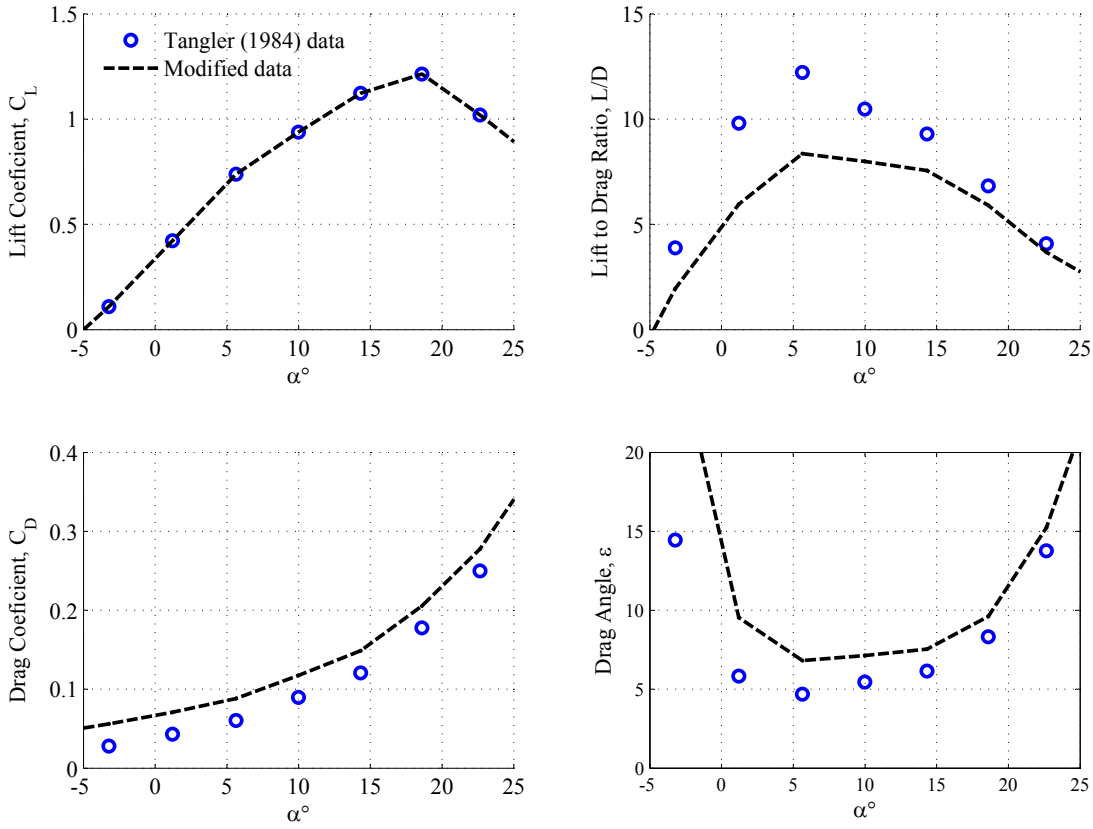

Figure 3.5 Assumed kite performance characteristics

3.3 Experimental Methods

Results output by the zero-mass model (Wellicome & Wilkinson, 1984) and the lumped mass model are compared with experimentally recorded kite trajectories. The apparatus, system calibration, validation and testing methods used to capture the experimental data are outlined in Chapter 2.

3.3.1 Testing

Comparison of experimental results with the lumped mass model required that a two dimensional manoeuvre was flown. The hot launch manoeuvre satisfies this requirement (see section 3.2.2).

Comparison with the zero-mass model is made for three dimensional figure of eight manoeuvres, typical of ship propulsion. The flight tests for this comparison were conducted in approximately 7m/s true wind.

To record the figure of eight trajectories, the flight envelope was first defined by pausing at three vertices along the line of static equilibrium (see chapter 2). Subsequently, a figure of eight motion was flown using approximately 70% of the horizontal and vertical extent of the flight envelope for each complete cycle. The wind strength, kite position angles, and line tension were each recorded with time, using the data acquisition equipment outlined in chapter 2.

3.3.2 Method of experimental analysis

For comparison of the zero-mass, and the lumped mass models with experiment it was necessary to process quantities from the experimentally measured variables using

the theory from the zero mass model. The experimentally measured onset velocity was calculated using equation 3.2 which differentiates between consecutive position angles to obtain the absolute kite velocity. The first term ($V\mathbf{v}$), was derived directly from the anemometer. A correction for the atmospheric boundary layer was applied using equation 3.1. The unit vector specifying the direction of the wind was taken to be, $\mathbf{v} = (\ 1 \quad 0 \quad 0\ )$, coincident with the X axis. It is noted that the alignment of the X axis is defined from the flight envelope definition procedure in chapter 2. The second term, $R\dot{\mathbf{r}}$, was obtained through application of equation 3.14 using the experimentally measured values for θ and ϕ . The time derivatives were obtained using a first-order backward differencing scheme. The magnitude of the position vector is defined by the measured line length, 28.0m. Data was captured at a frequency of 20Hz. Because the kite velocity is calculated through differentiation of consecutive positon angles, signal noise is present in the onset velocity. A one second moving average filter was used to smooth the onset velocity U between t-0.5s and t+0.5s. This smoothing period is sufficient to remove fluctuations due to electrical noise whilst not distorting the results significantly. Further details on smoothing and data filtration are given in Dadd (2005). The measured line load was directly recorded using the load cell.

3.4 Results and Discussion

In this section results are presented in the order itemised below

1. *Static performance measurements.* These data provide the aerodynamic performance characteristic values for input in the zero-mass model.

2. *Onset velocity prediction using zero-mass theory.* These results illustrate the behaviour of the zero-mass onset velocity using the input static performance measurements.

3. *Line tension comparison (hot launch).* These results provide comparison between experiment, the zero-mass model, and the lumped mass model.

4. *Effect of kite mass.* Zero mass input kite performance characteristics are adjusted to better enable close comparison with the lumped mass model (for the same static C_L and C_D), thus the influence of kite mass on line tension is demonstrated.

5. *Analysis of the lumped mass model.* These results examine closely how various parameters vary during a hot launch. The analysis provides further insight into flight behaviour, when mass is considered.

6. *Experimental results with comparison to zero-mass theory.* These results compare predicted line tensions for horizontally orientated figure of eight flight trajectories.

3.4.1 Static Kite Performance Measurements

For implimentaton of the zero mass model, experimentally measured static performance characteristics for the test kite (Flexifoil blade III), described in section 3.3, are shown in table 2.5. The mean values with 95% confidence limits are $\varepsilon = 9.55 \pm 0.3$, $L/D = 6.07 \pm 0.05$ and $C_L = 0.77 \pm 0.5$.

For implimentation of the lumped mass model, the in-built angle of attack for the test kite is determined photographically in accordance with the implementation of the lumped mass model (section 3.1.3) as $\alpha_K = -9°$. Here, the minus sign denotes a nose down attitude for the kite relative to the tangent line on the surface of the flight envelope.

3.4.2 Onset velocity prediction using zero-mass theory

Onset velocities were predicted as a function of kite position using zero-mass theory of section 3.1. The statically measured kite performance drag angle, $\varepsilon = 9.55$, is used with a wind speed of 10m/s. Figure 3.6 shows in polar form how the onset velocity varies for different positions of the kite relative to the wind in the horizontal

XY plane and in the vertical XZ plane. The onset velocity predictions in the XZ plane correspond to those which are expected during the hot launch (later used for experimental comparison for lumped mass model). The theoretical limiting positions of the kite are indicated by the line of static equilibrium. When the kite reaches this line, the kite comes to rest.

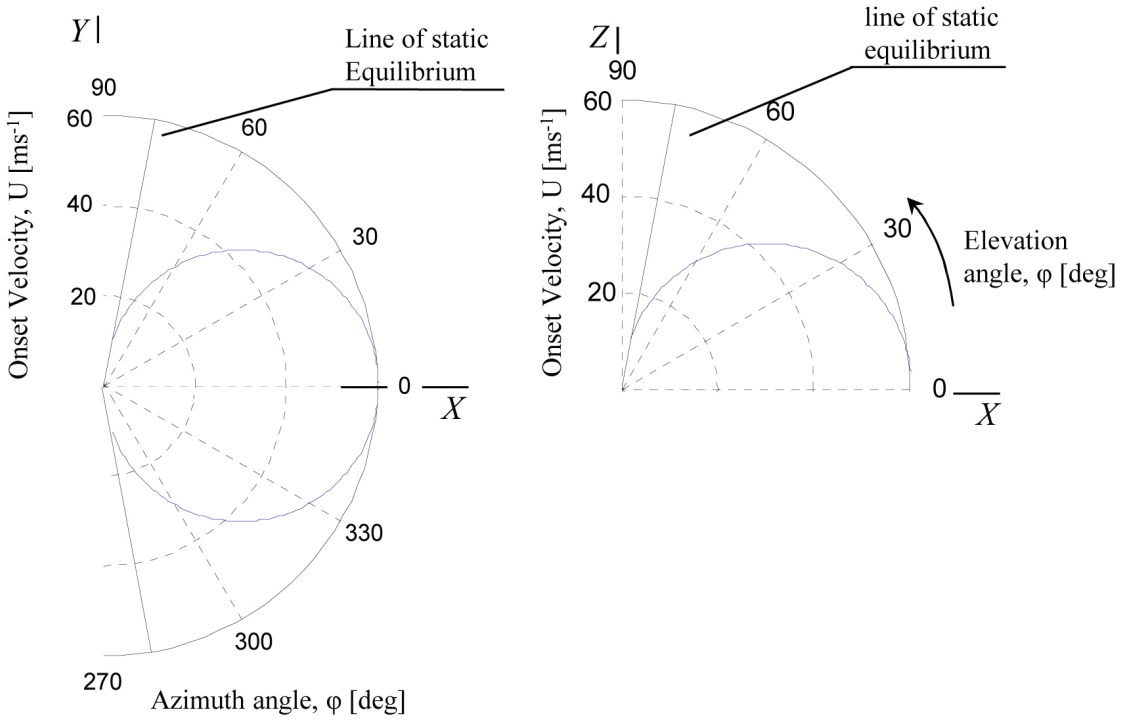

Figure 3.6 Onset velocity polar (plan view and side view)

3.4.3 Performance comparison for a 2D hot launch trajectory

Loads were predicted for a hot launch manoeuvre using the lumped mass and the zero-mass model and compared with experimental load in figure 3.8. The tests were conducted on a stationary platform in natural winds. In figure 3.9, the zero mass onset velocity is shown together with the measured onset velocity, U, and the measured comonents of onset velocity, V_K, and V_A. In figure 3.10, the statically measured lift coefficient is shown, together with the lift coeficient inferred from the measured load and the measured kite velocity, using equation 1.2. These figures presents one of 6 hot launch tests, selected because the flown kite reaches un-stalled flight relatively early and the trajectory is reasonably well centred in the flight envelope.

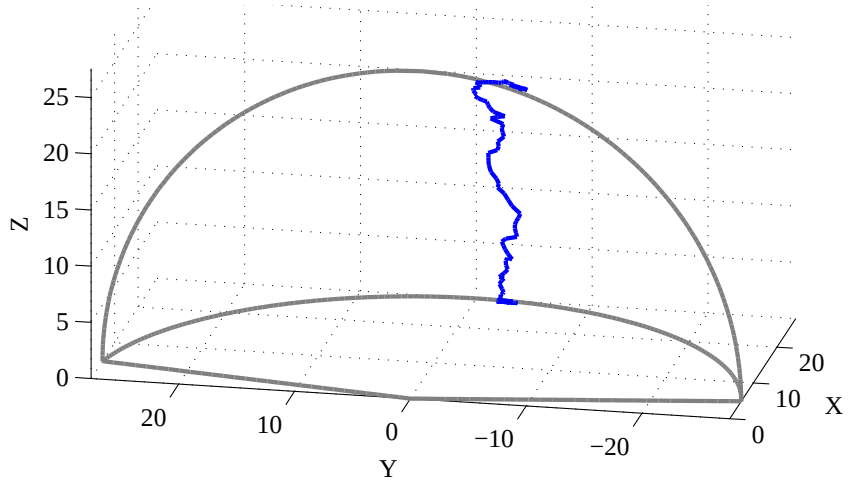

Figure 3.7 Trajectory for hotlaunch

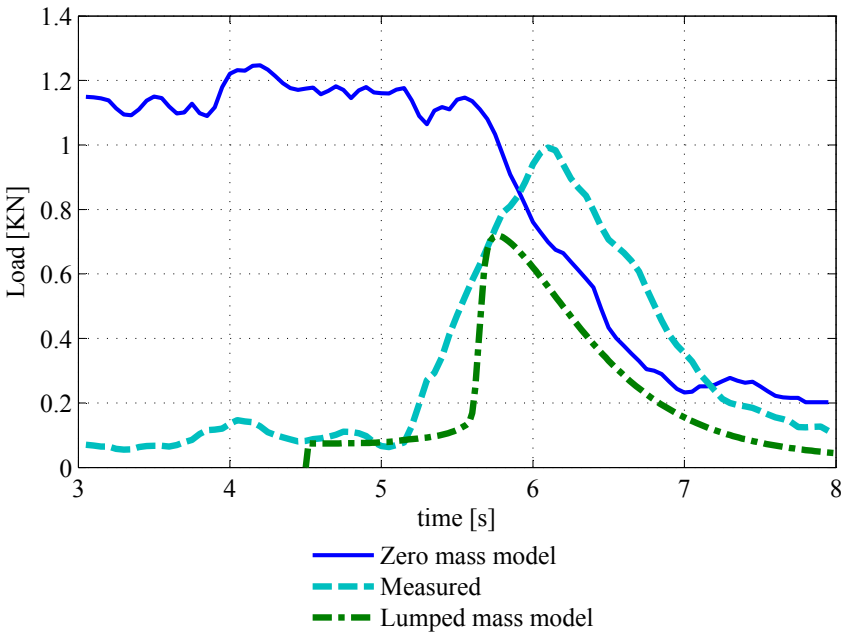

Figure 3.8 Experimenetal and Theortical Line load time histories

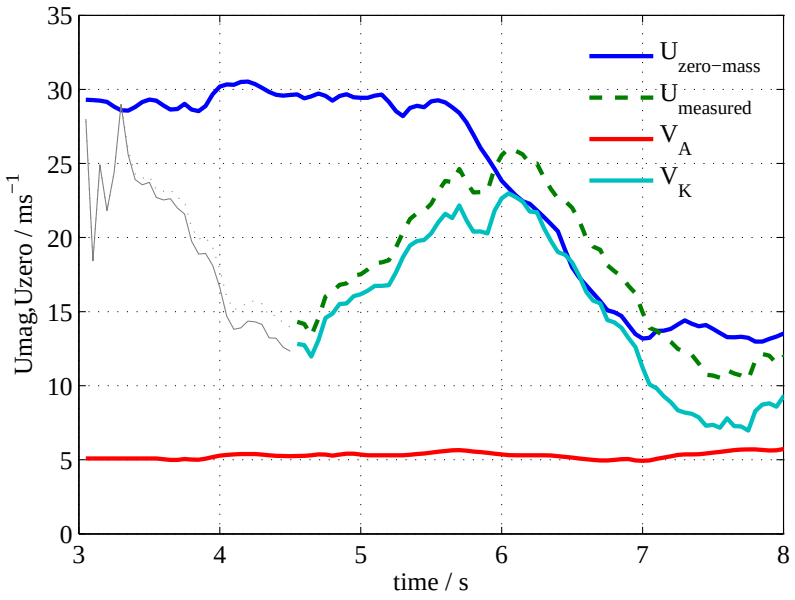

Figure 3.9 Experimental and Theoretical velocity components

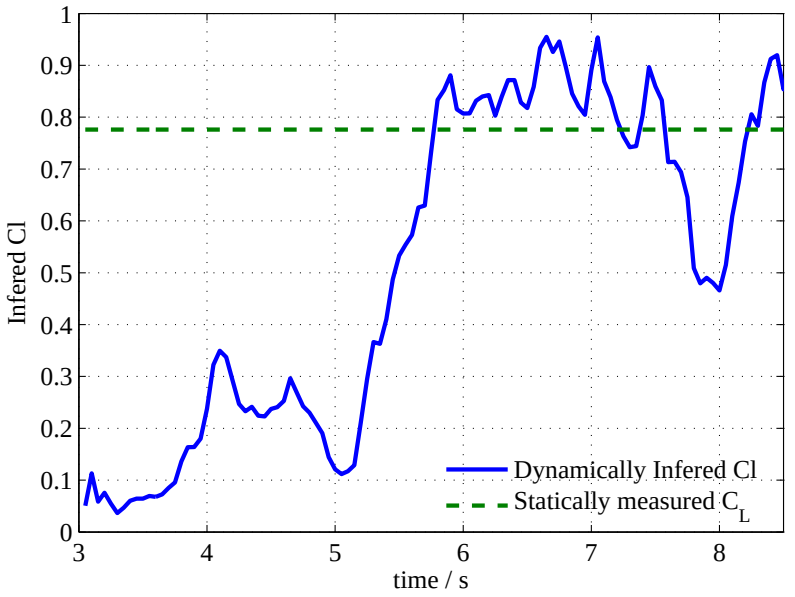

Figure 3.10 Statically measured C_L Experimental C_L. The experimental value is calculated from dynamic load and velocity corresponding to figure 3.8

In figure 3.8, The zero mass theortical load based on measured kite position is compared with the lumped mass theoretical load. It is seen that after $t = 6$s, there are similar trends , however, there are significant differences:

1. The peak lumped mass line tension is lower than the zero-mass line tension. This is because C_L and C_D are determined differently; the zero-mass model utilizes the statically measured C_L and C_D as an input, whereas the lumped mass model yields L/D and C_L as an output, which are recalculated during flight, depending on the assumed kite performance data in figure 3.5.

2. The lumped mass model correctly captures the load rise during flight initiation as the kite accelerates and becomes unstalled. The zero-mass model assumes that the kite is already fully initiated such that the kite has instantly accelerated up to its natural equilibrium velocity, even prior to launch. This is indicated by the erroneously high line load for $t < 5s$. In practice, when the kite is launched in this manner some time elapses before the kite moves through a condition of stalled flight.

3. The experimental rate of load increase is lower than the lumped mass rate of load increase. A likely cause is the different aerodynamic coefficients in the model compared to the real kite. A potential contributing factor could be the influence of unsteady aerodynamic effects on the experimental load. Where the angle of attack is changing rapidly Mcroskey (1982) and Green & McD Galbraith (1985) showed that normal fully stalled bluff body behaviour extends to lower angles of attack than would be expected if the angle of attack was varied slowly. The bluff body response ensues until steady state flow is fully established.

4. In natural winds on land, the wind profile may not be adequately accounted for by equation 3.1. This equation is used to correct the measured wind velocity for altitude according to a one-seventh power law. This exponent corresponds to typical conditions at sea. In practice, the wind shear depends on atmospheric conditions and may vary. Additional eddies in the wind are likely to be present due to interference with ground obstructions upstream of the test site.

5. The real flight path is not straight, and not perfectly located within the X-Z plane. This is due to the aforementioned difficulties in accurately traversing a pre-determined flight path via manual control. In practice, flying a pre-defined trajectory is difficult to achieve and differences between the intended trajectory and the flown trajectory are inevitable.

In figure 3.9 the time history velocity components U, V_A and V_K resemble the predicted velocity compments in figure 3.12 b).

Prior to $t = 4.5s$ it can be seen that the measured line tension indicates that the kite is not yet airborne and the measured kite velocity is eronious due to the swing of the flying arm as it aligns with the line tension at launch initiation. These data are shown greyed out.

The lift coeficient in figure 3.10 is seen to increase as the kite becomes unstalled, and although the measured value is eratic due to measurment noise in onset velocity measurment, the lift coeficient is seen to plateau once the kite flight has initiated close to the statically measured value ($C_L = 0.776 \pm 0.05$). If behaviour reflects the zero mass theory, in which the drag angle, ε, is fixed, it would be expected to see C_L remaining steady once initiated flight is achieved. This is not seen conclusively here however due to the irratic nature of the experimentally measured parameters that contribute to the calculation of C_L. Further investigation of the behavior of C_L is made theoretically in section 3.5.

The afformentioned limitations associated with the comparisons between the zero mass model and the lumped mass model make it hard to draw useful conclusions on the validity of these theories using this approach. Two alternative comparisons can be made which overcome some of the aforementioned limitations.

Firstly, of the two models, the zero-mass model can be most easily compared to experiment because recorded trajectories can be input into the model retrospectively. It is not required that a pre-determined trajectory be matched by manual flight, such as is the case when attempting to replicate the hot launch in the lumped mass model.

In fully initiated flight, such as for a three dimensional continuous trajectory in which the kite has reached close equilibrium of forces, the potential problems of unsteady behaviour at launch and wind effects in close proximity to the ground are overcome.

Secondly, A separate investigation can be made in which the lumped mass model is compared to the zero-mass model but with the zero-mass aerodynamic performance values adjusted to match those of the lumped mass model. These alternative comparisons are now made in the following sections.

3.4.4 Effect of kite mass

For assessing the importance of kite weight (and the impact of neglecting it completely), the zero-mass kite performance model parameters were changed to match those used for the lumped mass model ($C_L = 0.40$ and $L/D = 5.73$). These were output from the lumped mass model after allowing it to run until a static flight condition was reached. A variety of simulations were then completed to predict line load during hot launch:

1. zero-mass model, mass neglected.
2. lumped mass model, mass neglected (set to 0.0001Kg)
3. lumped mass model, mass = half kite weight (0.55Kg/2)
4. lumped mass model, mass = kite weight (0.55Kg)
5. lumped mass model, mass = double weight (1.1Kg)

Figure 3.11 compares the loads resulting from the zero-mass and the lumped mass models plotted to a base of θ. It can be seen that results are increasingly dissimilar during early launch for higher mass, but load predictions converge later for all cases. For kite mass closer to zero, convergence occurs earlier. In the limit where $M = 0$, the results are practically identical. It is noteworthy that setting the kite mass to 2M prevents the model from running unless the kite is initiated with 6ms^{-1} velocity.

This arises because at launch, the kite is deeply stalled and the lift produced in this condition is not sufficient to overcome the weight of the kite.

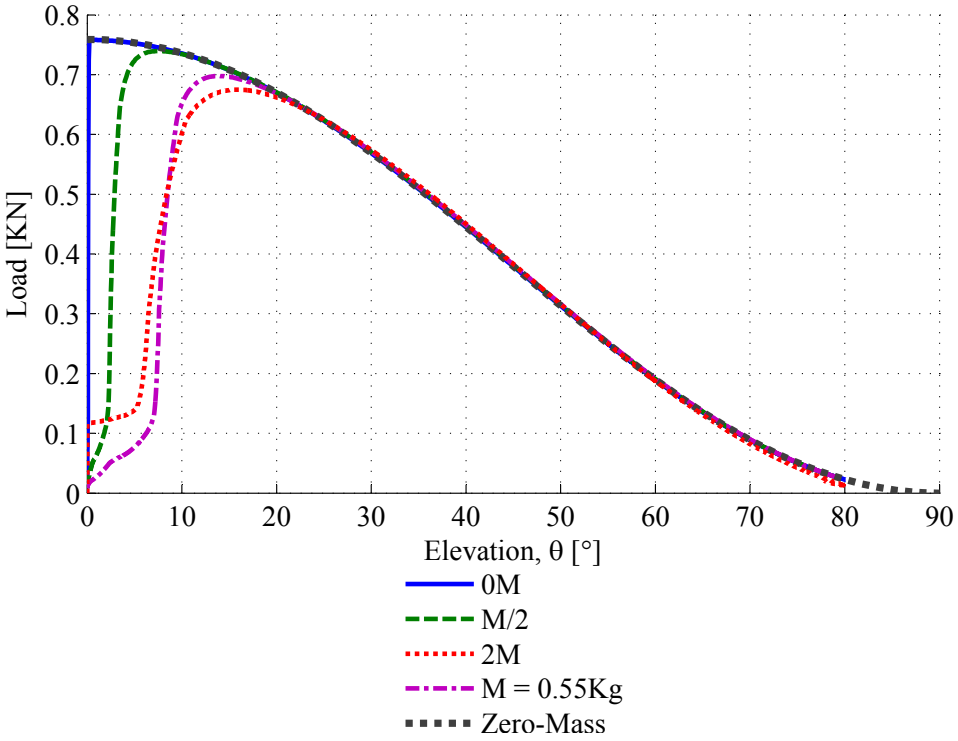

Figure 3.11 Lumped mass force versus elevation, for different kite mass

It is observed that the zero-mass model predicts velocity and hence positive line load until $\theta = 90°$, whilst the lumped mass model predicts that the kite comes to rest at $\theta = 80°$. In this respect the lumped mass model correctly predicts the limiting position angles of the flight envelope, whereas the zero-mass model requires that they be artificially imposed.

3.5 Analysis of the lumped mass model

A closer analysis of the parameters arising through the lumped mass model is given in this section. Figure 3.12 presents the time histories for a) elevation; b) kite velocity, onset velocity and apparent wind velocity; c) acceleration; d) effective angle of attack; e) drag angle; f) lift to drag ratio; g) lift and drag coefficients; and h) lift, drag and line tension. These detailed results are presented for the true kite mass of the experimental test kite, M=0.55Kg and M=0.0001Kg. The latter of the two cases closely approximates zero-mass.

When mass is neglected (denoted 0M in the figures), the effective angle of attack (α_E), the drag angle (ε), the lift to drag ratio (L/D) and the lift and drag coefficients (C_L and C_D) are all seen to arrive immediately at their respective values and are unchanging thereafter.

Where the true kite mass is considered (denoted by M in the figures), the elevation is seen to rise slowly at first before rising quickly at $t \approx 1.5$s (figure 3.12a). The effective angle of attack reduces from 80° to 20°, during which time the kite remains fully stalled (figure 3.12d). This stalled part of the manoeuvre is characterized by low L/D and low line tension (3.12f and 3.12h). After $t \approx 1.5$s the kite becomes unstalled and the lift increases very rapidly (figure 3.12h). Immediately after $t \approx 1.5$s, high acceleration ensues until the kite approaches its natural velocity at $t \approx 1.75$s, indicating close equilibrium of forces (figure 3.12c). The term 'natural velocity' is used to describe the kite speed predicted using the zero-mass assumption.

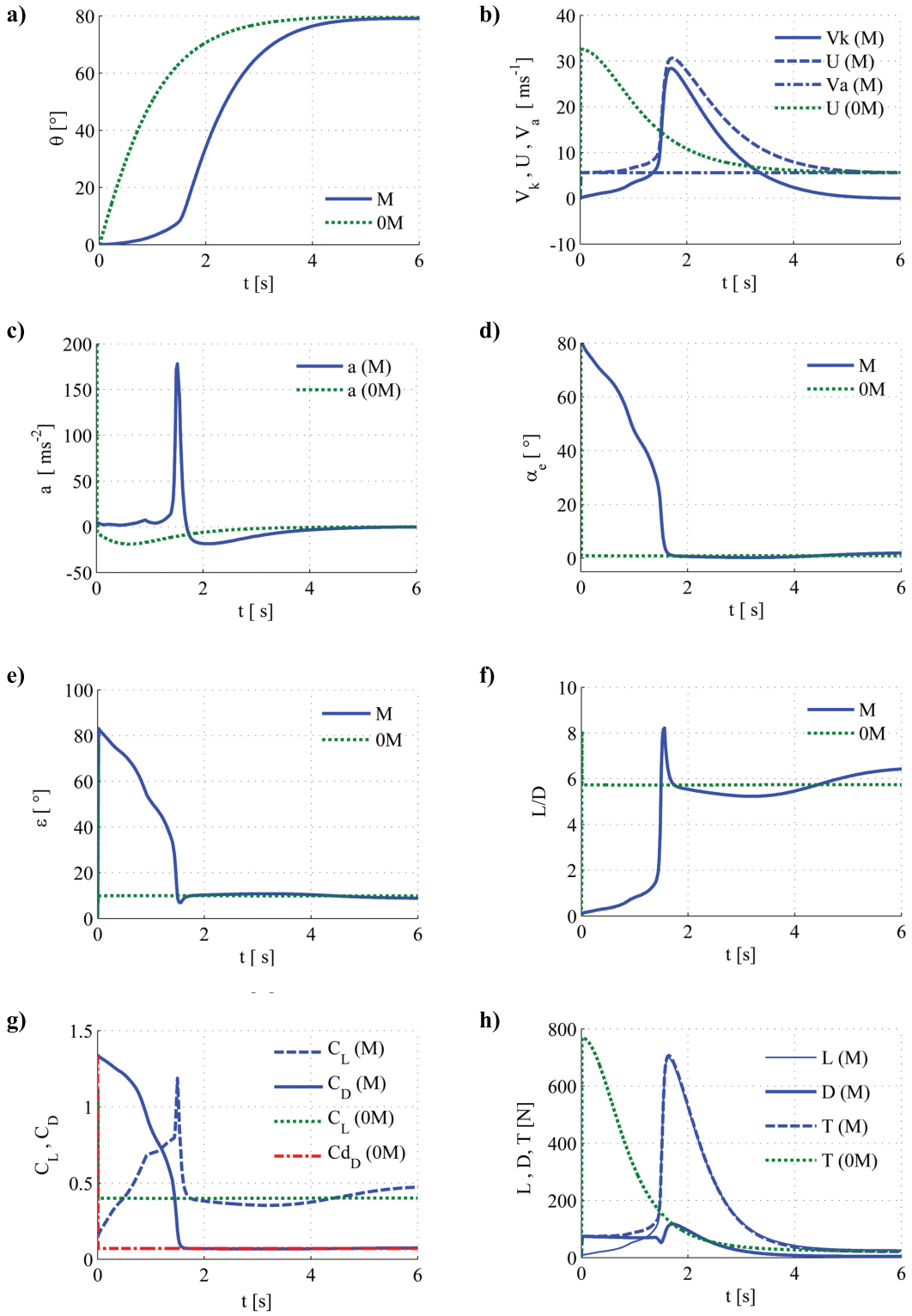

Figure 3.12 Variation of parameters in the point mass model during hot launch

Once the natural velocity is reached, the line tension follows the same trend for both cases ($M = 0.55$Kg and $M = 0.0001$Kg). Due to the time delay caused by the initial stall recovery, the difference in the line tension is best viewed in figure 3.11, where the result is plotted with elevation on the abscissa. Increased kite velocity results in a change in the angle of the onset wind velocity relative to the kite canopy. This can be appreciated by considering figure 3.2b), in which the vectors $\mathbf{V_A}$ and $\mathbf{V_K}$ determine the direction of the onset velocity, U. For a constant L/D, the angle of the aerodynamic force vector, $\mathbf{F}$ is fixed relative to the onset velocity, and therefore dependent on $\mathbf{V_K}$. Increasing kite velocity ($\mathbf{V_K}$), swings $\mathbf{F}$ rearwards, whilst reducing $\mathbf{V_K}$ swings F forwards.

In the zero-mass regime, the natural velocity of the kite occurs when the aerodynamic force vector is co-linear with the flying line, and $\mathbf{F}$ and $\mathbf{T}$ are perfectly balanced. As the kite progresses along its manoeuvre, the natural velocity changes accordingly. In the point mass model, the inertial and weight forces which act on the kite modify this idealised force balance such that the equivalent zero-mass natural velocity is not exactly achieved. For example, figure 3.12 shows that for the standard mass case during post stall recovery, L/D varies between 5.23 and 6.42. The variation in L/D and C_L is such that it induces an acceleration towards the natural velocity. Comparison of line tensions prediction from zero and point mass models indicate that these variations makes negligible difference to line tension predictions during fully initiated flight (figure 3.11). The main influence of mass is to delay or prevent recovery from stalled flight. It can thus be concluded that it is reasonable to neglect mass for determination of line tensions during fully initiated kite flight.

3.6 Zero mass theory compared to experimental results

Having demonstrated the effective use of the zero-mass model in two dimensions, the zero-mass theory was used to develop line tension predictions for a more complicated manoeuvre in three dimensions. The selected manouvre is one of four recordings

of horizontally orientated trajectoires, selected because a large horizontal extent of the flight envelope is used. The horizontal extent of the trajectory is progressively reducing for consecutive trajectories. The minimum turn radius is relatively shallow which prevents significant distortion of the kite canopy that may influence the aerodynamic properties of the kite. The experimental and theoretical results are compared for the same trajectory herein. The zero-mass theoretical results are obtained according to the *Zero mass implementation* in section 3.2. The experimental results are obtained according to the *Experimental methods* in section 3.3. Figure 3.13 shows an experimentally recorded three dimensional path for a horizontally orientated figure of eight manoeuvre.

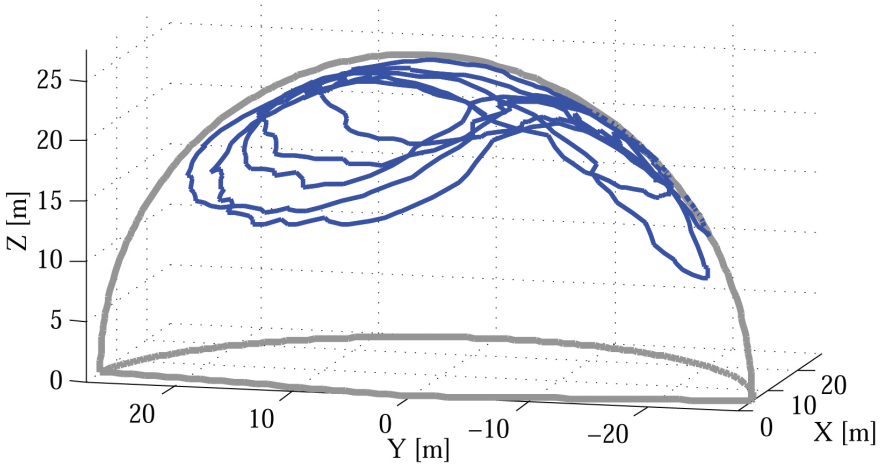

Figure 3.13 Three-dimensional path plot for experimentally recorded position angles

The experimental and theoretical time histories are presented in figures 3.14 to 3.17 inclusive. These figures show

1. Experimental position angles azimuth and elevation.
2. Experimental altitude corrected apparent wind velocity determined using the cup anemometer located near to the tether.
3. Experimental onset velocity obtained using measured ϕ, θ and V_A (see section 3.3.2) *and* Theoretical onset velocity, derived using the zero-mass equation 3.16.

4. Experimental line load, directly measured *and* theoretical line load based on U, equation 1.2 and equation 1.3.

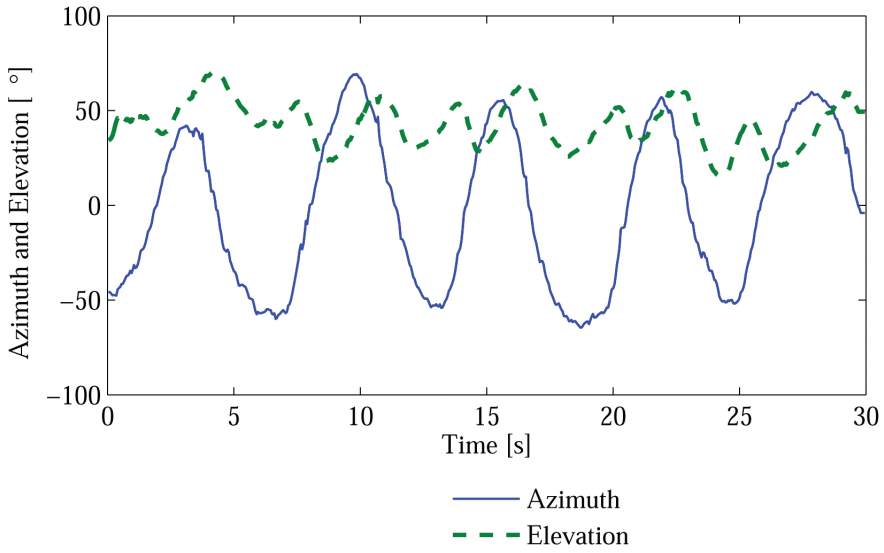

Figure 3.14 Experimental azimuth and elevation position angles

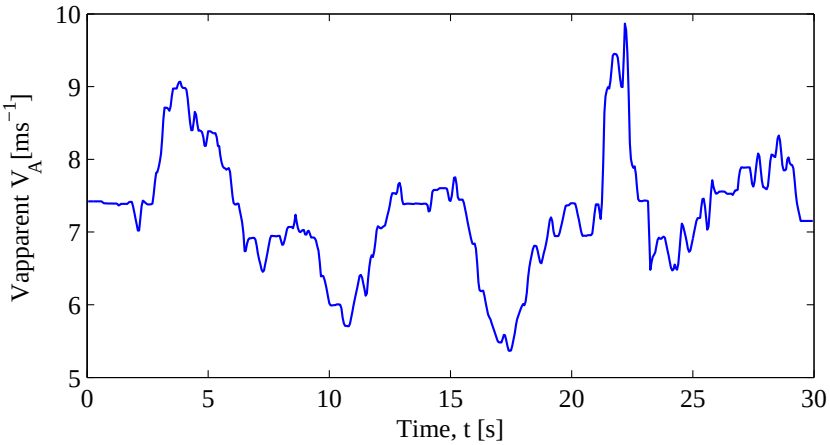

Figure 3.15 Experimental altitude corrected wind speed

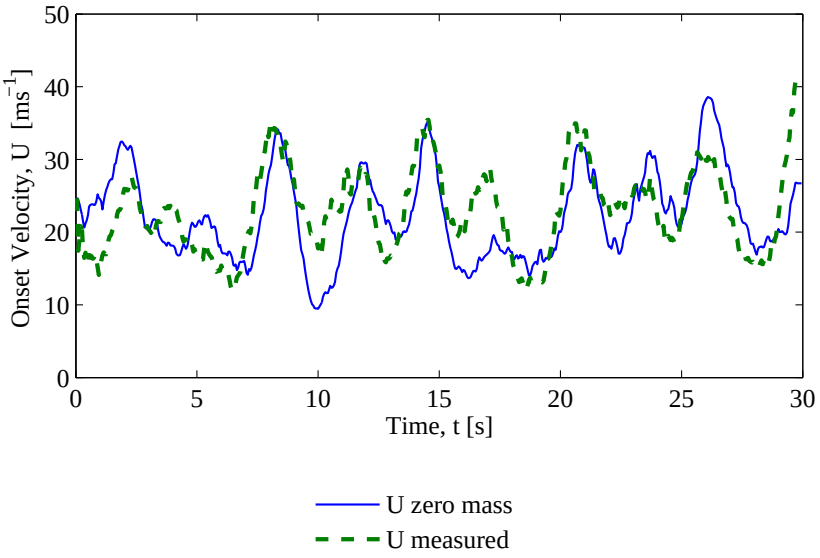

Figure 3.16 Experimental onset velocity; and zero-mass onset velocity

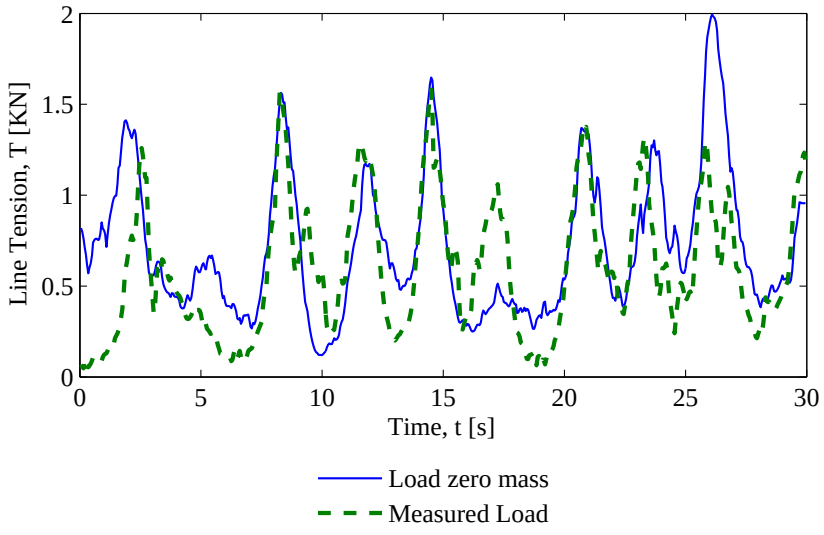

Figure 3.17 Experimental line tension; and zero-mass tine tension

There is good agreement between the line tension predicted using the zero-mass theory and the line tension measured directly using the load cell (figure 3.17). There are however exceptions during some periods, such as between $15s < t < 20s$, where the quality of the prediction is poor. To explain this, the inputs used in calculation of the zero-mass predicted line tension are themselves subject to errors which combine. Measured variables which are used as inputs for evaluating the zero-mass theoretical results include; altitude corrected wind velocity (V_A); kite position angles (θ, ϕ); the drag angle (ε); and lift coefficient (C_L) from static flight measurements.

Known causes that can contribute to the difference between measured and predicted line tensions are discussed in the following paragraphs. The measurement error for the position angles had been found by using 375 sample measurements of precisely defined arm positions, varied across the possible measurement range (Dadd, 2005). The standard deviation of the errors based on the sample set was 0.673°. Assuming a normal distribution and accurate calibration, the likely error is less than 1.32°, with 95% confidence, or less than 0.73% over the full 180° motion range of the gimballed transducers

The measured kite position is obtained by making the assumption that the flying lines remain perfectly straight. However, the drag force that acts along the length of the flying line induces a small curvature such that kite position is not precisely determined by the position angles at the line base. By considering the relative magnitude of line tension and line drag, curvature is estimated to be less than 0.9° during static flight and less during dynamic flight. The position error affects the zero-mass line tension prediction when compared to the load cell measurement however it does not affect the onset velocity calculation which also uses position angles as an input. This is because, provided the line curvature is unaltered for consecutive data points, the error does not contribute as it is negated through differentiation.

The apparent wind speed during dynamic flight tests was not constant but subject to natural variation. Changes in wind direction are also likely to be present due to

turbulence in the wind, although these direction changes are not directly measured in the current study. Instead, the direction was assumed to be constant, based on the flight envelope definition of section 3.3.1. The changing wind speed introduces spatial and temporal difference between the anemometer and the kite. This is to say that the anemometer measures the wind at one fixed position in space, whilst the kite traverses a variety of positions of differing horizontal and vertical extent, not all of which are accurately accounted for by application of equation 3.1, used to correct for the effect of the earths boundary layer. It was possible to estimate the feasible magnitude of this error by estimating the time elapsed for a wind particle to pass from the anemometer to the kite X coordinate, a distance downwind. The maximum recorded change in wind speed occurring during this elapsed time was found to be 20% of the mean. Taking a possible maximum wind measurement error of 20%, the calculated lift based on the wind measurement (L') can be compared to the possible true lift (L) by considering the estimated error ($\delta = 0.2U$). This is developed from equation 3.16:

$$\begin{aligned} L &\propto (U+\delta)^2 \\ \frac{L'-L}{L} &= \frac{\frac{1}{2}\rho \mathrm{A} C_L (2U\delta + \delta^2)}{L} \\ &= \frac{2U\delta + \delta^2}{U^2} \\ &= 2\left(\frac{\delta}{U}\right) + \left(\frac{\delta}{U}\right)^2 \\ &= 0.44 \end{aligned} \tag{3.41}$$

Equation 3.41 illustrates that a 20% difference between the true onset velocity and the theoretically predicted onset velocity leads to an estimated 44% difference between the measured and the theoretical lift. This tends to imply that high quality results require tests to be conducted using artificially created winds. Although infrequent, such artificially created winds can be created by towing the test rig on a still day, to generate the required wind speed. This method removes the spatial and temporal variations in the wind.

The load cell measurement had been shown to be less than 24.0N with 95% confidence (Dadd, 2005). Expressing this as a percentage of the calibrated load range (180Kg) yields a measurement error of 1.36%.

3.7 Conclusions

A test rig for measuring kite performance had been previously developed by the same author. The experimental methods have been newly implemented for measurement of static flight performance characteristics and for recording dynamic flight time histories. Measurement error is less than 1.32% for kite position angles and 1.36% percent for load measurement over the operable range, with 95% confidence.

For the test used in the current study (Flexifoil blade III 3m^2), the static performance parameters are $L/D = 6.07 \pm 0.5$ and $C_L = 0.77 \pm 0.05$. These are established with 95% confidence. It has been shown that higher L/D induces higher onset velocities, favourable to generating line tension.

The kite flies such that it seeks a natural velocity that is determined by the zero-mass theory, although in the presence of mass, it may not be achieved exactly. The significance of the assumptions that the kite and lines are weightless, and that L/D and C_L remain constant during dynamic flight, have been assessed by comparison to a new point mass model that considers mass and allows L/D and C_L to be freely determined. It has been demonstrated, that in the limit where $M = 0$, the two adopted models produce nearly identical results. For a kite of light construction, kite mass modifies flight so that L/D and C_L only vary slightly and thus can be assumed to remain constant at their static flight values to obtain a reasonable engineering approximation to kite flight. If the construction of the kite and lines is such that the weight is larger in comparison to the aerodynamic forces generated, then the point mass model is likely to be necessary to predict variations in L/D and C_L and thus kite performance.

The zero-mass theory has been used to demonstrate that dynamic performance in terms of the kite velocity and line tension can be predicted in a computationally inexpensive way by assuming that the kite is weightless, and that under this assumption, L/D and C_L remain constant during dynamic flight. The line tensions during dynamic manoeuvres have been predicted using the zero-mass theory and are shown to compare favourably with experimental results. In comparing the zero-mass model to experiments, there is a reliance on measured quantities for input, namely the wind velocity at the kite, the static flight drag angle, and the kite spherical position co-ordinates. This requires these quantities to be measured as accurately as possible. Through analysis of potential errors, it is likely that the most significant error affecting kite performance predictions is that caused by the spatial variability in the wind between the kite and the anemometer itself. Although these can be desirably reduced by making corrections, these are most effectively eliminated by conducting testing on still air days whilst generating the required apparent wind strength through a steady tow velocity.

Chapter 4

Determination of Kite Forces using Three Dimensional Flight Trajectories

Chapter 3 used the zero mass kite manoeuvring theory to predict kite line tension and other performance parameters. These results were compared with real kite trajectories that had been recorded using a purpose-specific kite dynamometer. The predicted and measured line tensions were shown to agree favourably for a steady flight path without very tight turn; that work focused on the validation of performance prediction for a given kite position, which enabled line tension to be obtained for a given instant in time. This was done using the zero-mass model, without directly knowing the kite velocity, V_K, such that it was not possible to obtain theoretically the rate of progression around the manoeuvre or a time averaged force prediction. Instead, the trajectories had been input using real recorded kite positions which included kite positions already plotted to a base of time, such that time progression around the manoeuvre was determined through experiment, and aerodynamic forces were obtained based on the onset velocity, U. This chapter focuses on the additional modelling required in order to determine kite velocity theoretically, an essential feature to enable the kite performance to be established as a function of time using purely theoretically defined input manoeuvre shapes.

4.1 Parameterisation of kite trajectory shapes

The trajectory parameterisation follows the work of Wellicome & Wilkinson (1984), however, it is further modified here to allow vertically and diagonally orientated trajectory shapes. The figure of eight flying manoeuvre shape can be mathematically defined as comprising two small circle sweeps for the ends of the manoeuvre and two great circle sweeps which connect the small circular ends (figures 4.1 and 4.2). The trajectory is defined by input parameters $(\theta_1, \theta_2, \phi_1, \phi_2, \alpha_1, \alpha_2)$ that define the size and location of the small circle ends.

The great circle sweeps are along the intersections of a plane passing through the origin with the sphere surface. The small circle ends are defined using a semi-vertex angle for the cone swept out by the radius, and the position of the circle pole at its centre.

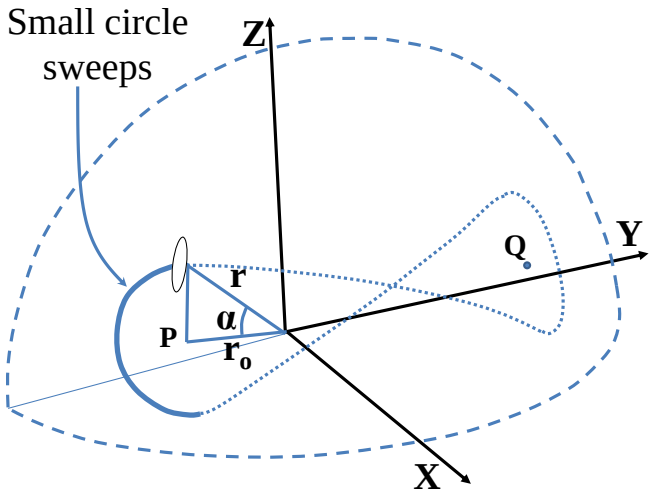

Figure 4.1 Small circle sweep geometry

The spherical position angles that define kite line position (ϕ and θ) are as shown in figure 4.2. The unit position vector of the kite is given by

$$\mathbf{r} = (\cos\theta\cos\phi, \cos\theta\sin\phi, \sin\theta). \tag{4.1}$$

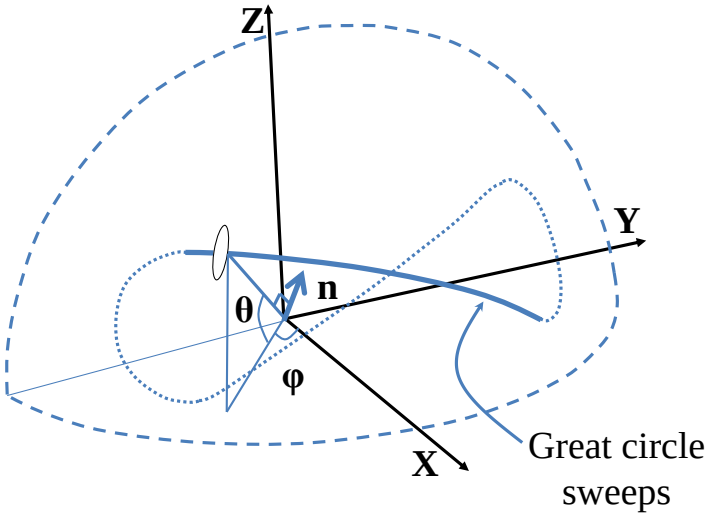

Figure 4.2 Great circle sweep geometry

The unit vector $\mathbf{n} = (n_1, n_2, n_3)$ is chosen normal to the plane of the great circle sweep such that $\mathbf{n} \bullet \mathbf{r} = 0$, which provides

$$n_1 \cos\theta \cos\phi + n_2 \cos\theta \sin\phi + n_3 \sin\theta = 0. \tag{4.2}$$

Equation 4.2 can be rearanged to give

$$\tan\theta = -\left(\frac{n_1}{n_2}\cos\phi + \frac{n_2}{n_3}\sin\phi\right). \tag{4.3}$$

Hence, equation 4.3 can be used to establish (θ,ϕ) ordinates on any great circle defined by $\mathbf{n}$. The direction of the kite is defined by the value of $\dot{\phi}/\dot{\theta}$, which can be determined by differentiation of 4.2,

$$\left(-\mathrm{n}_1 \cos\theta \sin\phi + \mathrm{n}_2 \cos\theta \cos\phi\right)\dot{\phi} + \left(-\mathrm{n}_1 \sin\theta \cos\phi - \mathrm{n}_2 \sin\theta \sin\phi + \mathrm{n}_3 \cos\theta\right)\dot{\theta} = 0, \tag{4.4}$$

such that

$$\frac{\dot{\phi}}{\dot{\theta}} = \frac{\sin\theta\left(\mathrm{n}_1 \cos\phi + \mathrm{n}_2 \sin\phi\right) - \mathrm{n}_3 \cos\theta}{\cos\theta(\mathrm{n}_2 \cos\phi - \mathrm{n}_1 \sin\phi)}. \tag{4.5}$$

For the small circle ends in figure 4.1, the pole P with position vector r_o defines the centre of the small circle sweep. The semi-vertex angle α defines the size of the circle. Points that lie on the small circular arc conform to

$$\mathrm{r} \bullet \mathrm{r}_o = \cos\alpha, \tag{4.6}$$

where

$$\mathrm{r} = (\cos\theta\cos\phi, \cos\theta\sin\phi, \sin\theta) \tag{4.7}$$

and

$$\mathrm{r}_o = (\cos\theta_o\cos\phi_o, \cos\theta_o\sin\phi_o, \sin\theta_o). \tag{4.8}$$

Therefore,

$$\cos\alpha = \cos\theta\cos\theta_o\cos(\phi - \phi_o) + \sin\theta\sin\theta_o \tag{4.9}$$

leading to

$$\phi = \phi_o \pm \cos^{-1}\left(\frac{\cos\alpha - \sin\theta\sin\theta_o}{\cos\theta\cos\theta_o}\right). \tag{4.10}$$

Hence, equation 4.10 can be used to establish (θ,ϕ) ordinates on any small circle sweep. The direction of flight, for the small circle ends, is determined through differentiation of equation 4.9 as

$$\frac{\dot{\phi}}{\dot{\theta}} = \frac{\cos\theta\sin\theta_o - \sin\theta\cos\theta_o\cos(\phi - \phi_o)}{\cos\theta\cos\theta_o\sin(\phi - \phi_o)}. \tag{4.11}$$

To fully define the manoeuvre geometry, two poles (P(θ_1, ϕ_1) and Q(θ_2, ϕ_2)) are required with corresponding semi-vertex angles (α_1 and α_2) for each of the small circle ends, as well as calculation of the two normal vectors, **n** and **m**, to define the great circle sweeps, right to left and left to right respectively. One must establish these manoeuvre segments as forming a continuous path by ensuring tangency at the respective joins. For this, consideration is given to the spherical triangle shown in figure 4.3, with a view to finding the ratios n_1/n_3 and n_2/n_3 which can later be used to ensure that tangency and continuity is correctly obtained.

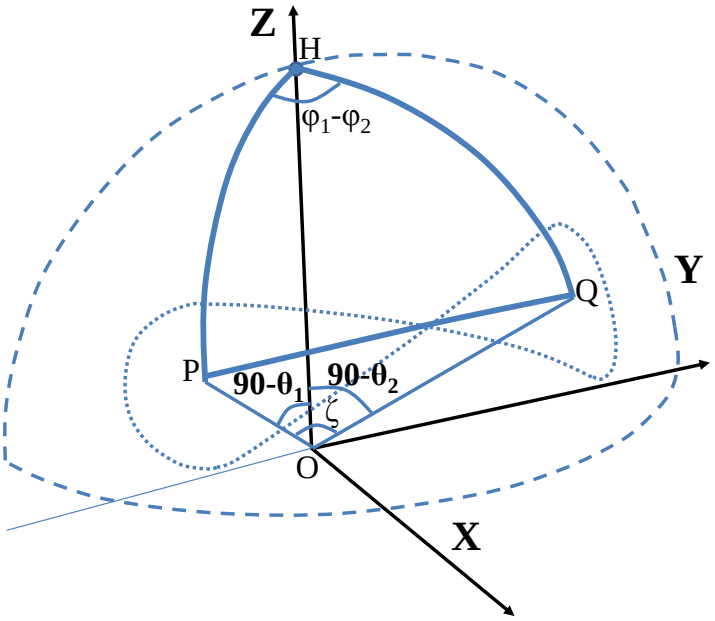

Figure 4.3 Spherical Triangle HPQ

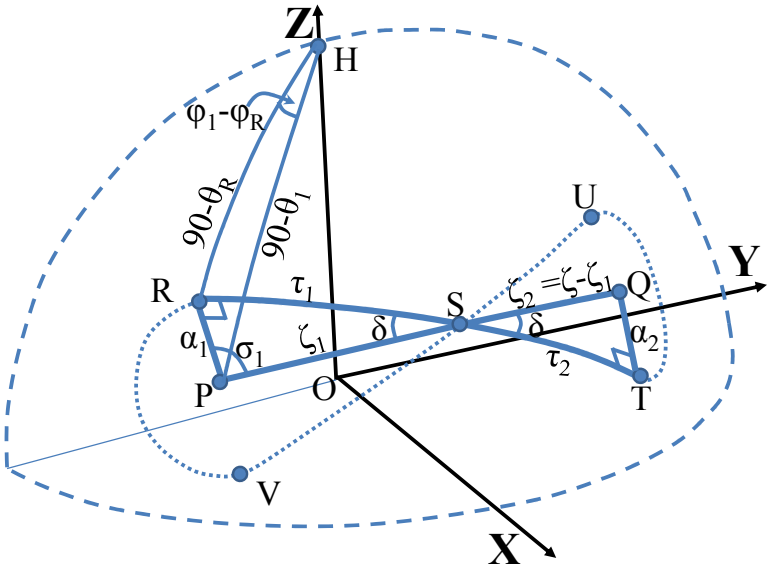

Figure 4.4 Spherical Triangles PRS, QST and HPR

PH and QH in figure 4.3 are great circles passing through the Z axis and PQ is another great circle passing through O. The angle subtended between OP and OH is $(90-\theta_1)$, the angle subtended between OQ and OH is $(90-\theta_2)$, the angle subtended between OP and OQ is ζ and the angle subtended between HP and HQ is $(\phi_1-\phi_2)$. Applying the standard spherical cosine formula to triangle HPQ, ζ can be found;

$$\cos\zeta = \cos(90-\theta_1)\cos(90-\theta_2) + \sin(90-\theta_1)\sin(90-\theta_2)\cos(\phi_1-\phi_2) \tag{4.12}$$

or

$$\cos\zeta = \sin\theta_1\sin\theta_2 + \cos\theta_1\cos\theta_2\cos(\phi_1-\phi_2). \tag{4.13}$$

Figure 4.4 shows the intersection node points (R, T, U and V) for the consecutive great circle and small circle sweeps, ζ_1 and ζ_2 are the angles subtended between OP and OS and between OQ and OS respectively. α_1, α_2, τ_1 and τ_2 equivalently represent their included angles with the origin. The angle formed by the intersection of PQ and RT is δ. The angle RPQ is σ_1, the angle HOR is $(90-\theta_R)$, the angle HOP is $(90-\theta_1)$ and the angle RHP is $(\phi_1-\phi_R)$. HR, HP, RP, PQ, RT and QT are all great circles. Triangle PRS and triangle STQ are right triangles. Applying the spherical sine formula to PRS,

$$\frac{\sin\alpha_1}{\sin\delta} = \frac{\sin\zeta_1}{\sin 90}, \tag{4.14}$$

$$\sin\delta = \frac{\sin\alpha_1}{\sin\zeta_1}, \tag{4.15}$$

and

$$\sin\delta = \frac{\sin\alpha_2}{\sin\zeta_2}. \tag{4.16}$$

Through equating 4.15 and 4.16 and using $\zeta_2 = \zeta - \zeta_1$, the value of ζ_1 is given by

$$\tan\zeta_1 = \frac{\sin\zeta\sin\alpha_1}{\sin\alpha_2 + \cos\zeta\sin\alpha_1}. \tag{4.17}$$

Applying the cosine formula to triangle PRS, τ_1 can be obtained with

$$\cos\zeta_1 = \cos\alpha_1\cos\tau_1 + \sin\alpha_1\sin\tau_1\cos 90 = \cos\alpha_1\cos\tau_1, \tag{4.18}$$

therefore

$$\cos\tau_1 = \frac{\cos\zeta_1}{\cos\alpha_1}. \tag{4.19}$$

Applying sine formula to triangle PRS, $\sigma 1$ is obtained using

$$\sin\sigma_1 = \frac{\sin\tau_1}{\sin\zeta_1}, \tag{4.20}$$

and employing the sine formula with triangle HPQ in figure 4.3 gives

$$\sin(HPQ) = \frac{\cos\theta_2\sin(\phi_1 - \phi_2)}{\sin\zeta}. \tag{4.21}$$

Then, HPR is given by

$$HPR = HPQ - \sigma_1. \tag{4.22}$$

Applying cosine formula to traingle HPR enables calculation of θ_R,

$$\cos(90 - \theta_R) = \cos\alpha_1\cos(90 - \theta_1) + \sin\alpha_1\sin(90 - \theta_1)\cos HPR, \tag{4.23}$$

therefore

$$\sin\theta_R = \cos\alpha_1\sin\theta_1 + \sin\alpha_1\cos\theta_1\cos(HPR). \tag{4.24}$$

Finally, applying the sine formula to trangle HPR allows ϕ_R to be solved using

$$\sin(\phi_1 - \phi_R) = \frac{\sin\alpha_1\sin(HPR)}{\cos\theta_R} \tag{4.25}$$

The use of equations 4.13 through 4.25 allows the locations the nodes θ_R and ϕ_R to be solved for a given input set [θ_1, ϕ_1, α_1, θ_2, ϕ_2, α_2] that define the manoeuvre shape. A similar set of equations can be developed to establish the values of θ_T and ϕ_T. These values for points R and T can be input in equation 4.2 and solved to establish the ratios $n1/n2$ and $n3/n2$. Thus equation 4.3 may be used to define a

series of data points along the great circle sweep, RT. A similar process is repeated to establish a series of positions along the other great circle sweep, UV. Points which lie on the small circular end about P are established using 4.10 and similarly for points that lie on the small circular end about Q.

Data points on the surface of the sphere which form a continuous and tangent curve around a figure of eight shape have now been defined. The parameterised trajectory may be transformed using Euler rotations to achieve a vertically or diagonally orientated figure of eight manoeuvre shape positioned at different angles relative to the onset wind. Rotations are applied to the position vector, r, first about the X axis, then about Y and about Z respectively in that order as

$$\mathbf{r'} = \mathbf{E_3 E_2 E_1 r} \tag{4.26}$$

The rotation angles η_1, η_2 and η_3 about X Y and Z respectively are user selected and the rotation matrices are $E1$ $E2$ and $E3$ given by

$$\mathbf{E_1} = \begin{bmatrix} 1 & 0 & 0 \\ 0 & \cos\eta_1 & \sin\eta_1 \\ 0 & -\sin\eta_1 & \cos\eta_1 \end{bmatrix} \tag{4.27}$$

$$\mathbf{E_2} = \begin{bmatrix} \cos\eta_2 & 0 & -\sin\eta_2 \\ 0 & 1 & 0 \\ \sin\eta_2 & 0 & \cos\eta_2 \end{bmatrix} \tag{4.28}$$

and

$$\mathbf{E_3} = \begin{bmatrix} \cos\eta_3 & \sin\eta_3 & 0 \\ -\sin\eta_3 & \cos\eta_3 & 0 \\ 0 & 0 & 1 \end{bmatrix} \tag{4.29}$$

$\dot{\phi}/\dot{\theta}$ is then determined numerically in place of 4.5 and 4.6. If only values of onset velocity and kite force are required for different points along the trajectory, one can follow the implementation of section 3.2, using the now theoretically defined values

for θ and ϕ, in this section. However the established onset velocity would not require, or allow the calculation of the kite velocity, V_K. If the requirement is to obtain time averaged quantities, then V_K must be determined to establish rate of propagation. Then it becomes possible to conduct a time integration of the various parameters of interest. The next section provides the means with which this is achieved.

4.2 Determination of kite velocity and time averaged quantities

This section is based on the work of Wellicome & Wilkinson (1984). The X, Y and Z components of 3.15 can be written separately as

X:

$$U\cos\gamma\cos\beta = V + R\cos\theta\sin\phi\dot{\phi} + R\sin\theta\cos\phi\dot{\theta} \tag{4.30}$$

Y:

$$U\cos\gamma\sin\beta = -\cos\theta\cos\phi R\dot{\phi} + \sin\theta\sin\phi R\dot{\theta} \tag{4.31}$$

Z:

$$U\sin\gamma = -\cos\theta R\dot{\theta} \tag{4.32}$$

Combining 4.32 with 3.16 yields an expression for $R\dot{\theta}$, for the velocity of the kite in the θ direction,

$$R\dot{\theta} = -V\frac{\cos\phi\sin\gamma}{\sin\varepsilon}. \tag{4.33}$$

Substituting equation 3.16 and 4.33 in 4.31 yields an expression for $R\dot{\phi}$, for the velocity of the kite in the ϕ direction,

$$R\dot{\phi} = -V\left[\frac{\tan\theta\sin\phi\sin\gamma + \cos\gamma\sin\beta}{\sin\varepsilon}\right]. \tag{4.34}$$

Equations 3.16 and 4.33 can be combined to yield an expression for the direction of the kite from kite flight dynamic considerations,

$$\frac{\dot{\phi}}{\dot{\theta}} = \frac{\tan\theta\sin\phi\sin\gamma + \cos\gamma\sin\beta}{\cos\phi\sin\gamma}. \tag{4.35}$$

4.30 combined with 3.16, 4.33 and 4.34 and after manipulation becomes

$$\sin\varepsilon = \sin\theta\sin\gamma + \cos\theta\cos\gamma\cos(\phi - \beta) \tag{4.36}$$

or

$$\beta = \phi \pm \cos^{-1}\left[\frac{\sin\varepsilon - \sin\theta\sin\gamma}{\cos\theta\cos\gamma}\right]. \tag{4.37}$$

For a stationary kite, $\gamma = \beta = 0$, so that substitution of these values into 4.37 enables determination of azimuth and elevation values along the line of static equilibrium that limits the motion of the kite. The time taken for the kite to manoeuvre from a point θ_A to θ_B can be obtained from

$$T = \int_{\theta_A}^{\theta_B} \frac{dt}{d\theta} d\theta = \int_{\theta_A}^{\theta_B} \frac{1}{\dot{\theta}} d\theta \tag{4.38}$$

and the time averaged aerodynamic force F is given by

$$F = \frac{1}{T}\int_{\theta_A}^{\theta_B} F dt = \frac{1}{T}\int_{\theta_A}^{\theta_B} \frac{F}{\dot{\theta}} d\theta. \tag{4.39}$$

The angle of elevation for the time averaged force F is determined as

$$\theta = \tan^{-1}\left(\frac{F_y}{\sqrt{\left({F_x}^2 + {F_y}^2\right)}}\right). \tag{4.40}$$

The azimuth angle for the time averaged force is determined as

$$\phi = \tan^{-1}\left(\frac{F_y}{F_x}\right). \tag{4.41}$$

The magnitude of force acting in the horizontal plane for useful ship propulsion is thus obtained as

$$F_{xy} = F\cos\theta \tag{4.42}$$

4.3 Implementation

Using the procedure outlined in section 4.1, a horizontally orientated figure of eight was defined as the default manoeuvre shape ($\theta_1 = -25, \phi_1 = 7, \alpha_1 = 8, \theta_2 = 25, \phi_2 = 7, \alpha_2 = 8$). Thie default trajectory was manipulated using Euler rotation angles, η_1, η_2 and η_3 shown in table 4.1. This manipulation produced 15 different trajectories, shown graphically in figure 4.5. The kite performance input parameters (C_L and L/D) had been previously obtained by experiment, shown in table 2.5. The kite area was now selected as $320\,\mathrm{m}^2$ and the line length was 300m.

The theory of section 4.1 and 3.1.2 was implemented using Matlab (Mathworks, 2009) to obtain purely theoretical predictions for; the kite position angles (θ, ϕ); the kite velocity (V_K); the onset wind position angles (γ,β); and the aerodynamic force, (F). The flow diagram in figure 4.6 shows the order in which calculations were conducted.

During the implementation it was found that there is more than one mathematically feasible solution, for example, equation 4.37 has two roots. For each point along the trajectory, it was necessary to select the solution that ensured that there were no discontinuities in the resulting time histories and that the proper sense of the force vector was achieved, such that line tensions are positive.

Table 4.1 Euler rotation angles for vertical trajectory manipulation.

Trajectory	η 1	η2	η3
1	105	35	67
2	102	35	60
3	100	35	50
4	98	35	40
5	96	35	30
6	94	35	20
7	92	35	10
8	90	35	0
9	88	35	10
10	86	35	20
11	84	35	30
12	82	35	40
13	80	35	50
14	78	35	60
15	75	35	67

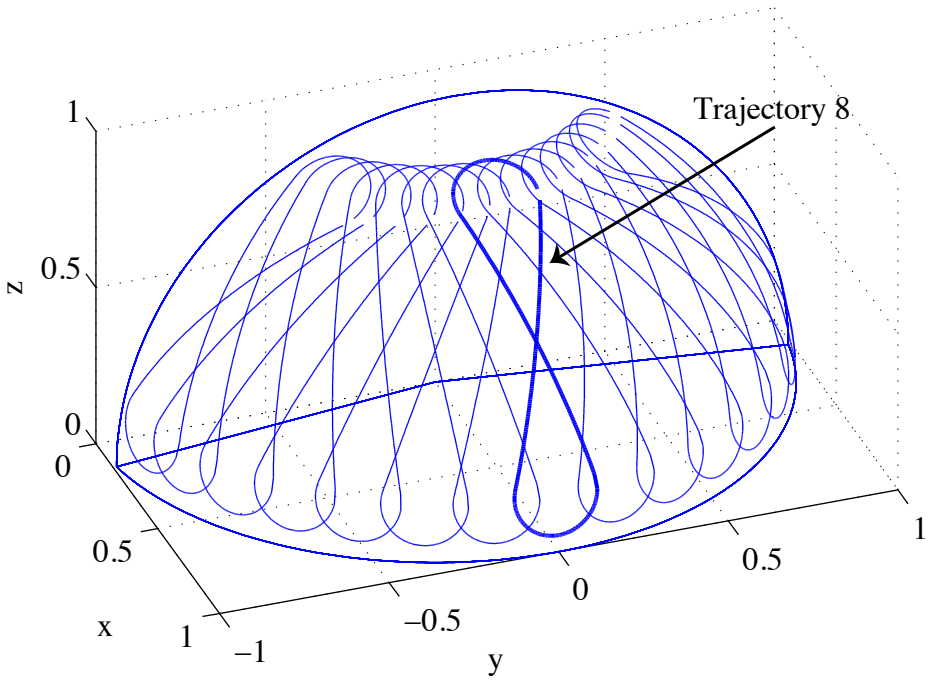

Figure 4.5 Vertical trajectories

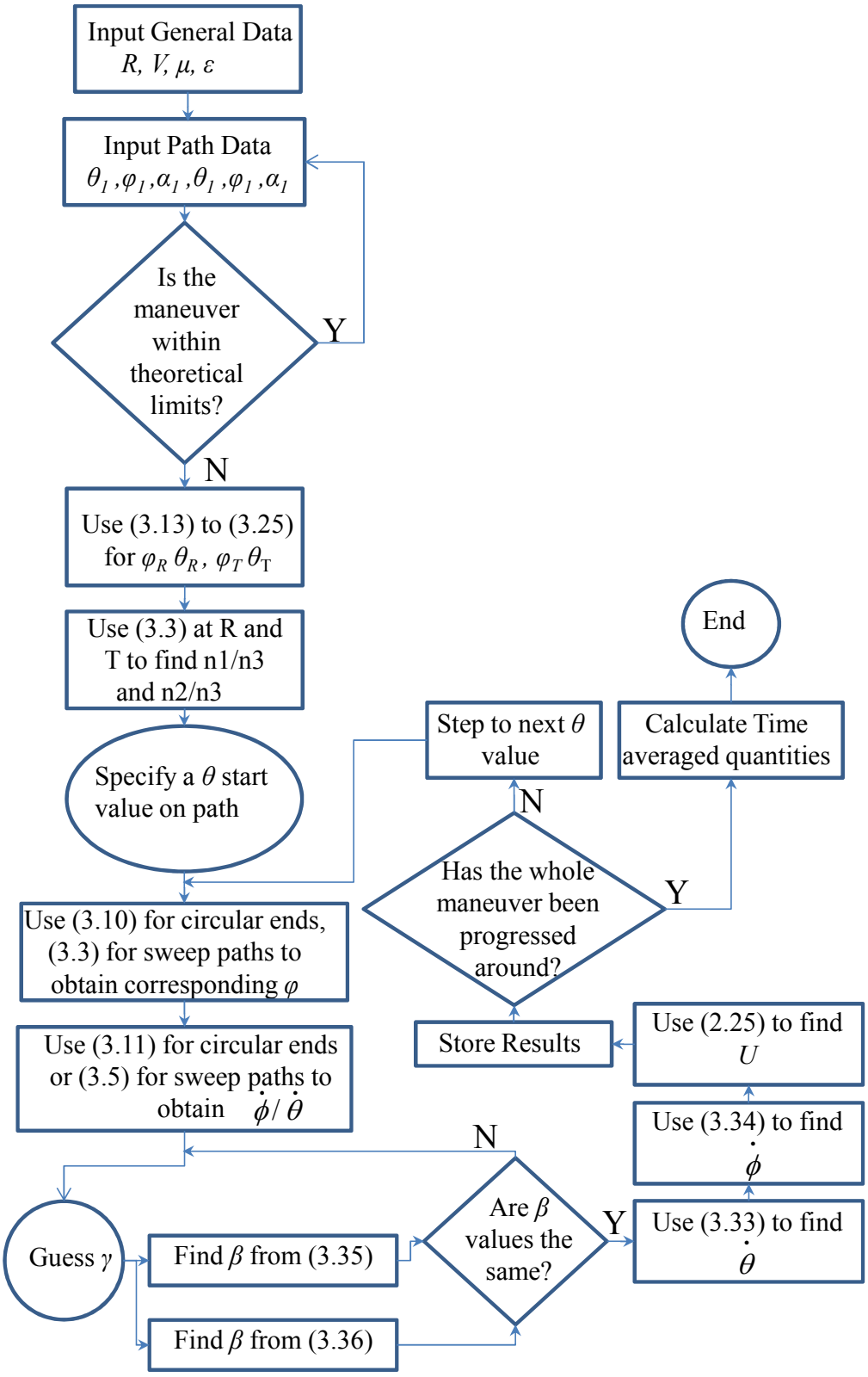

Figure 4.6 Implimentation flow diagram

4.4 Results

Example results using the implementation of section 4.3 were obtained for trajectory number 8, shown highlighted in figure 4.5. The results are;

1. trajectory position angles (θ, ϕ) in figure 4.7;
2. onset velocity and kite velocity (U, V_K) in figure 4.8;
3. onset wind position angles (γ,β) in figure 4.9;
4. and aerodynamic force, (F) in figure 4.10.

The determined relationship, between the input manoeuvre shape and the output force, provides a basis on which a desired load response can be attained. The theory could now be used for producing a control algorithm to regulate output kite force in a certain wind strength. Figure 4.8, for example, shows that the line tension varies between $0.3 \times 10^5 N$ and 2×10^5 N as it traverses along the figue of eight defined by figure 4.7.

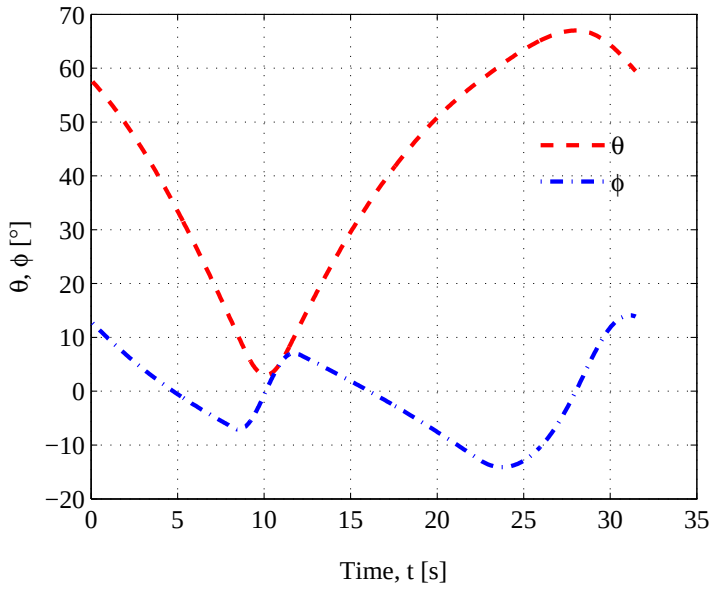

Figure 4.7 Azimuth and Elevation (trajectory 8)

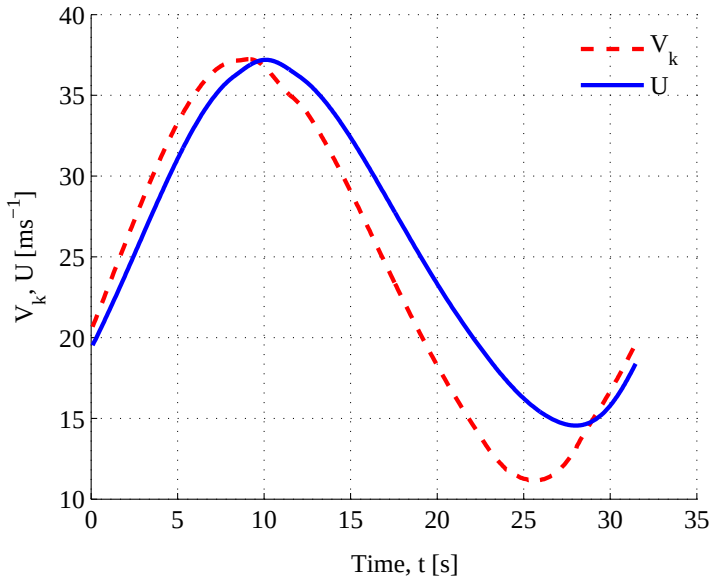

Figure 4.8 Onset velocity and kite velocity (trajectory 8).

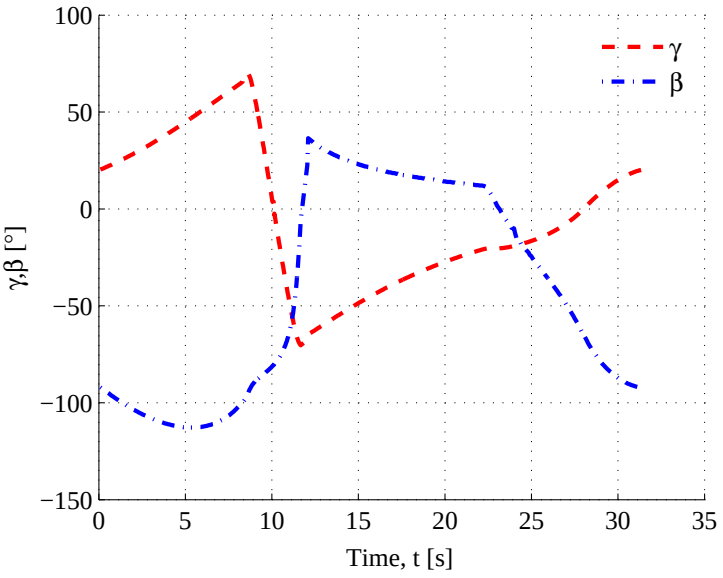

Figure 4.9 Elevation and Azimuth of onset velocity (trajectory 8)

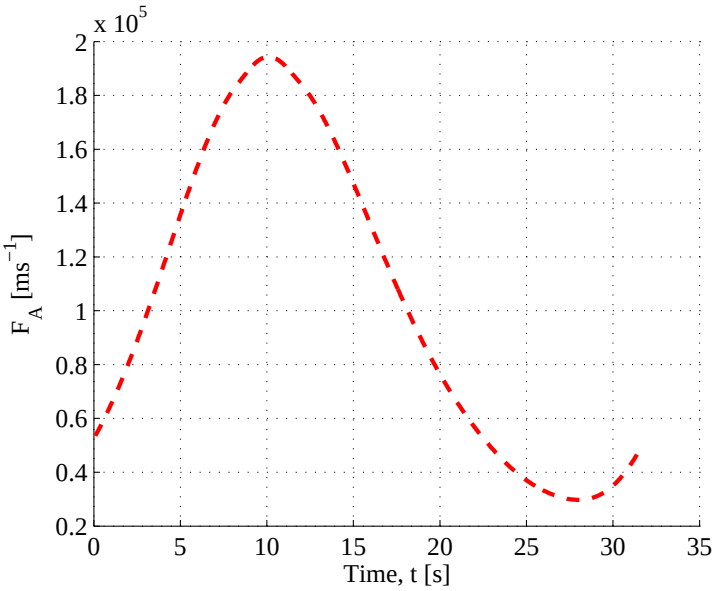

Figure 4.10 Aerodynamic Force (trajectory 8)

4.5 Experimental Validation

The method for calculating the onset velocity, and hence aerodynamic force, had been validated in chapter 3. It was now required to verify that the rate of propagation along the figure of eight, via V_K, had been correctly established. This was achieved by comparison to experimental trajectories. A figure of eight was recorded according to section 3.3. An equivalent theoretical trajectory was defined according to section 4.1 with input parameters, $\theta_1 = 41$; $\phi_1 = -41$; $\alpha_1 = 12$; $\theta_2 = 40.5$; $\phi_2 = 42$; $\eta_1 = 0$; $\eta_2 = 0$; and $\eta_3 = 0$. These trajectories are shown in figure 4.11. Small differences are apparent due to irregularities in the manual flight path and due to fluctuations in the recorded position angles. Results for the aerodynamic force were established in three ways;

1. F_A was calculated based on experimental position angles (θ,ϕ) input into the zero-mass model, thus propagation of the manoeuvre with time is determined experimentally;

2. F_A was measured directly, with time;

3. F_A was calculated for the theoretically defined manoeuvre, with time established via equation 4.38. This was based on only one of the angular velocity components that contribute to kite velocity V_K (i.e $\dot{\theta}$).

Figure 4.12 shows the results. It can be seen that the theoretical time for the kite to progress, closely matches that of the experimental kite trajectory. This serves to validate equations 4.30 through equation 4.38. The errors arising are discussed in chapter 3, section 3.6.

The percentage error, E, between the zero mass theoretical load (based on experimental position) and the measured line load is presented in figure 4.13. The root mean square deviation is expressed as a percentage of the experimental load range

such that

$$E = \frac{\sqrt{(F_{Aexp} - F_{Azm})^2}}{Max(F_{Aexp}) - Min(F_{Aexp})}, \tag{4.43}$$

where subscripts *exp* and *zm* denote experiment and zero mass respectively. The most significant error for experimentally determined kite trajectories was proposed to be due to spatial and temporal differences in wind speed across the flight envelope, which were not properly accounted for (see equation 3.41). The mean error, or root mean square deviation (RMSD) for this trajectory was 15.28, according to equation 4.43.

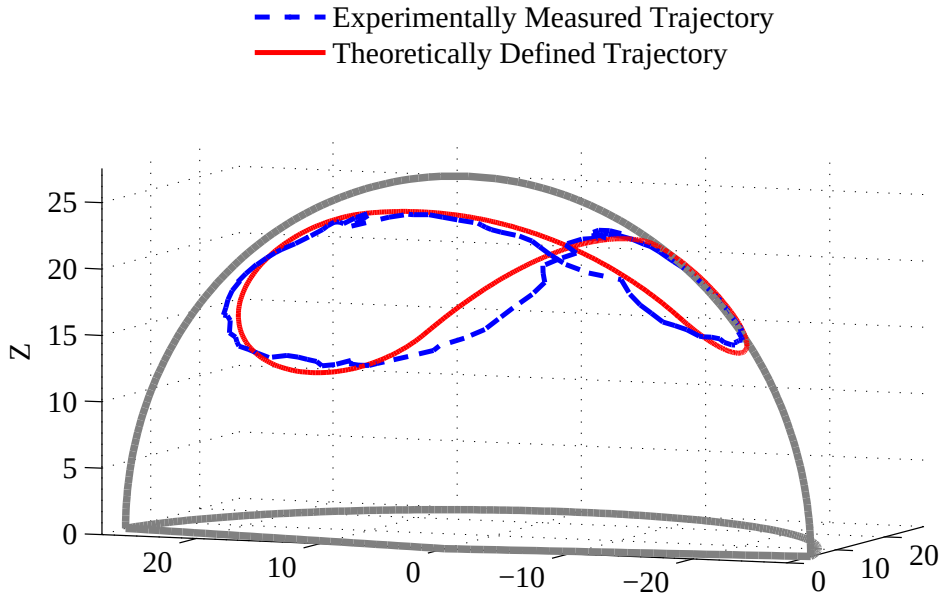

Figure 4.11 Experimental and theoretical trajectories

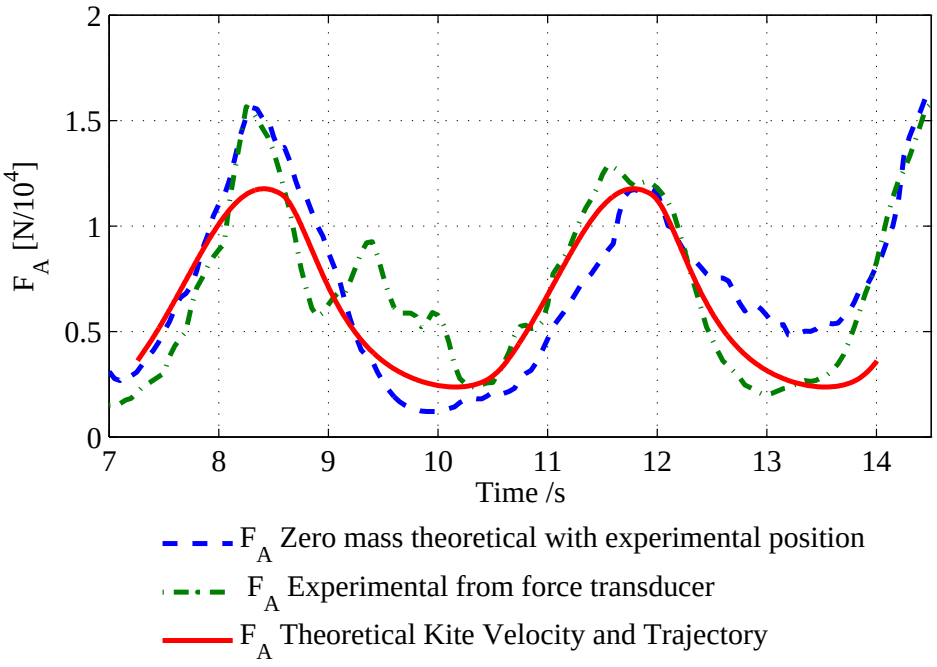

Figure 4.12 Theoretical and experimental force predictions compared to a base of time

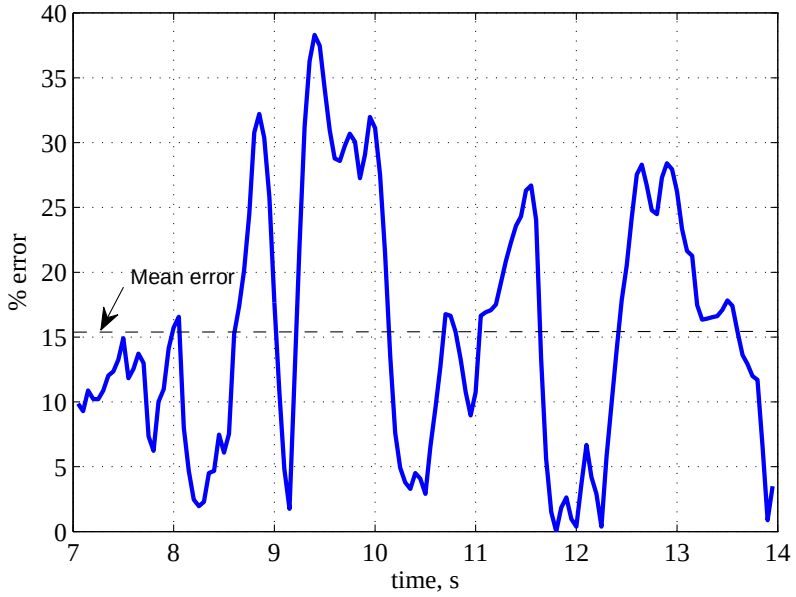

Figure 4.13 Percent error between experimental force and theoretical load based on experimental position

4.6 Determination of time averaged force polar

For predicting ship performance, a force polar diagram is required. The time averaged aerodynamic forces were calculated using equations 4.38 and 4.39 for each of the trajectories in table 4.1. This provides a range of forces corresponding to different mean wind angles. The following cases were considered, with results plotted in figure 4.14:

1. Initially, no consideration was given to the variation of wind with altitude. This hypothetical case was implemented for an even wind speed at all altitudes, $6.18\,\mathrm{ms}^{-1}$ (see results in figure 4.14 A);

2. to demonstrate the effect of the the Earths atmospheric boundary layer, the kite forces were computed with the inclusion of wind gradient according to equation 3.1. The wind speed at $Z = 10\mathrm{m}$ was $6.18\mathrm{ms}^{-1}$ (see figure 4.14 B);

3. the instantaneous kite force along the line $\theta = 15°$ was computed. This provides a benchmark to compare time averaged figure of eight trajectories against and thus illustrates the force reduction arising due to the practical requirement to traverse back and fourth (see figure 4.14 C);

4. Horizontal manoeuvre shapes centred on an elevation of 15° were found to yield the highest time averaged propulsive drive forces, most favourable for ship propulsion. This trajectory parameterisation is presented in the next section (see figure 4.14 D).

In figure 4.14, it is seen that a significant increase in line tension is achieved by virtue of the stronger winds at altitude. This added benefit is unique to kite propulsion systems and is not realised by conventional sails to the same extent. In this case, it is shown to increase the propulsive drive force by a factor of ~ 2 (see figure 4.14 A and B). The wind speed versus altitude according to equation 3.1 is plotted together with the hypothetical even wind speed ($6.18\mathrm{ms}^{-}1$) in figure 4.15.

The maximum possible line force can be achieved instantaneously during a straight pass across the flight envelope (see figure 4.14 C). The best elevation angle is later shown to be 15°, due to increasing wind strength with altitude. This maximum can be viewed alternatively as the force realised from a figure of eight trajectory centred at $\theta = 15°$ with infinitely long weightless lines, such that the full extent of the trajectory may be considered to remain at a single discreet value of azimuth and elevation. This result can not in practice be realised for a sustained period of time, however it shows the extent by which the propulsive drive force is reduced by traversing the kite around the trajectories that inevitably utilise non-optimal regions of the flight envelope.

There are a wide number of parameters that can potentially be varied in order to characterise the system for ship propulsion. The next section presents the sensitivity study that was carried to investigate these.

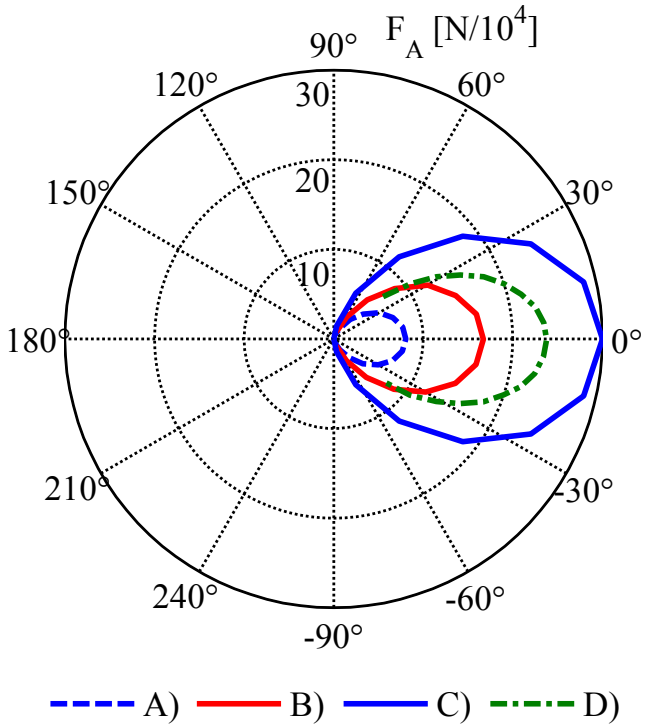

Figure 4.14 Horizontal component of kite force, $F_{A_{xy}}[\mathrm{N}/10^4]$ for different cases: (A) Time averaged vertical trajectories, wind speed = $6.18\,\mathrm{ms}^{-1}$, wind gradient off. (B) Time averaged vertical trajectories, wind speed = $6.18\,\mathrm{ms}^{-1}$ at $Z_{\mathrm{ref}} = 10\,\mathrm{m}$, wind gradient on. (C) Instantaneous kite force along straight horizontal trajectory $\theta = 15°$, wind speed = $6.18\,\mathrm{ms}^{-1}$ at $Z_{\mathrm{ref}} = 10\,\mathrm{m}$, wind gradient on. (D) Time averaged horizontal trajectories, wind speed $6.18\,\mathrm{ms}^{-1}$ at $Z_{\mathrm{ref}} = 10\,\mathrm{m}$, wind gradient on.

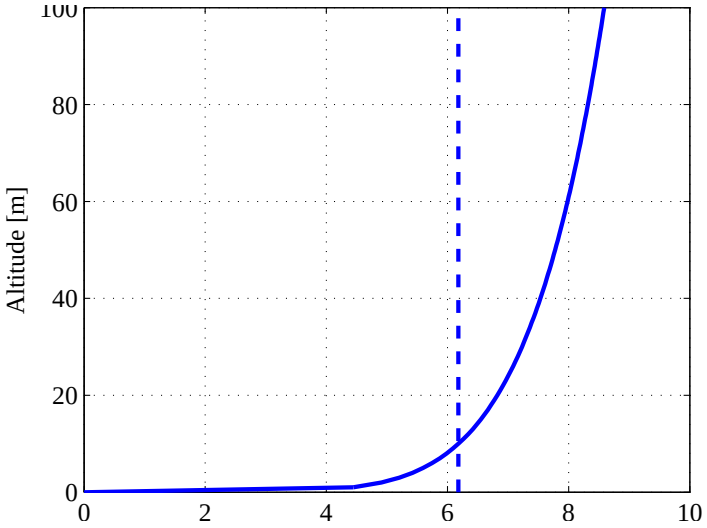

Figure 4.15 Wind profiles

4.7 Optimization and Sensitivity Study

Having defined a generic kite force polar diagram using a time averaged , investigations have been undertaken to establish factors which influence optimal trajectories. These factors include

1. the ideal elevation for maximizing line tension;
2. the ideal elevation to maximize the useful propulsive drive force;
3. kite aspect ratio;
4. angle of attack;
5. and manoeuvre pole separation and Pole circle size;

4.7.1 Ideal elevation for maximising absolute line tension

The effect of increased wind speed (V_A) with altitude tends to improve the dynamic onset velocity U. Thus, the influence is to increase F_A with elevation. However, a reduction to F_A occurs due to the influence of elevation (θ) in equation 3.16. There is an optimum elevation at which the line tension is maximized with respect to these effects. In order to find this optimum, equation 3.16 and 3.1 are combined with the altitude, expressed as ($Z = R\sin\theta$), to obtain the onset velocity (U) as a function of (θ),

$$U = V_{Tref}\left(\frac{R\sin\theta}{Z_{ref}}\right)^{n}\frac{\cos\theta\cos\phi}{\sin\varepsilon}. \tag{4.44}$$

The maximum onset velocity (and thus lift) occurs at an elevation value which is the solution to $\mathrm{d}\,U/\,\mathrm{d}\,\theta = 0$, subject to $\mathrm{d}^2U/\,\mathrm{d}\,\theta^2 < 0$. Differentiating equation 4.44 yields

$$n\left(\frac{R\sin\theta}{Z_{ref}}\right)^{n-1}\frac{R\cos^2\theta}{Z_{ref}} - \sin\theta\left(\frac{R\sin\theta}{Z_{ref}}\right)^{n} = 0. \tag{4.45}$$

Taking $n = 1/7$ for typical conditions at sea (Claughton *et al.*, 1998), $Z_{\mathrm{ref}} = 10\,\mathrm{m}$, $R = 300\mathrm{m}$ and $\varepsilon = 9.55°$, the solution to equation 4.45 is $\theta = 20.7°$. Therefore

in the presence of a wind gradient caused by the Earths boundary layer, the onset velocity and hence line tension can be maximised by maintaining a trajectory that is centred closely on this value of elevation, for $R = 300m$. This result is useful where the absolute value of the line tension magnitude is important, such as for producing electricity using kite power.

This solution is unique to $R = 300$m. Increased line length allows a lower mean elevation angle to be used for the same altitude such that the drive force component is improved.

4.7.2 Ideal elevation for maximising propulsive drive force

For ship propulsion, only the horizontal component of the line tension leads to useful propulsive force such that the ideal elevation is not the same as for largest absolute line tension. The horizontal component reduces with the cosine of elevation, so that the optimum is obtained by maximizing the value of $U\cos\theta$:

$$U\cos\theta = V_{Tref}\left(\frac{R\sin\theta}{Z_{ref}}\right)^{n}\frac{\cos^2\theta\cos\phi}{\sin\varepsilon} \tag{4.46}$$

Setting $\mathrm{d}(U\cos\theta)/\mathrm{d}\,\theta = 0$, subject to $\mathrm{d}^2U\cos\theta/\mathrm{d}\,\theta^2 < 0$ to find the maximum value gives,

$$n\left(\frac{R\sin\theta}{Z_{ref}}\right)^{n-1}\left(\frac{R}{Z_{ref}}\right)\cos^2\theta - 2\sin\theta\left(\frac{R\sin\theta}{.}Z_{ref}\right)^{n} = 0 \tag{4.47}$$

When solved numerically, equation 4.47 yields the maximum horizontal component of drive force where $\theta = 15.0°$. Hence for ship propulsion in the presence of a wind gradient, an optimal trajectory should centre closely to this elevation. In this respect, horizontally orientated figure of eight trajectories are preferential to vertical ones for downwind sailing, since elevation angles during the manoeuvre remain closer to the optimum value. However, for courses sailed close to the wind a vertically orientated trajectory must be used in order to maintain a close winded time averaged force, such as for trajectories 1 and 15 in table 4.1. Trajectories which reflect this optimization have been investigated using the default parameters

($\theta_1 = -25, \phi_1 = 7, \alpha_1 = 8, \theta_2 = 25, \phi_2 = 7, \alpha_2 = 8$). These have been transformed using equation 4.26 and table 4.2 such that manoeuvres are horizontally orientated and elevated to 15° (see figure 4.16). The time averaged horizontal force output for each trajectory is shown in figure 4.14(D). By comparing figure 4.14(B) with figure 4.14(D), horizontally orientated manoeuvres centred proximally to the optimum elevation are seen to make a significant improvement to the drive force compared to vertical ones.

Table 4.2 Euler rotation angles for horizontal trajectory manipulation.

Trajectory	$\eta 1$	$\eta 2$	$\eta 3$
1	0	15	48
2	0	15	40
3	0	15	32
4	0	15	24
5	0	15	16
6	0	15	8
7	0	15	0
8	0	15	8
9	0	15	16
10	0	15	24
11	0	15	32
12	0	15	40
13	0	15	48

4.7.3 Effect of kite aspect ratio

To investigate the effects of kite aspect ratio on aerodynamic force, the kite drag angle is expressed as a function of the lift to drag ratio using equation 1.12. Equation 3.16 and equation 1.7 are combined to yield an expression that relates the drag angle to aerodynamic force,

$$F_A = \frac{1}{2}\rho A \left(\frac{V_A \cos\theta \cos\phi}{\sin\varepsilon} \right)^2 C_F \tag{4.48}$$

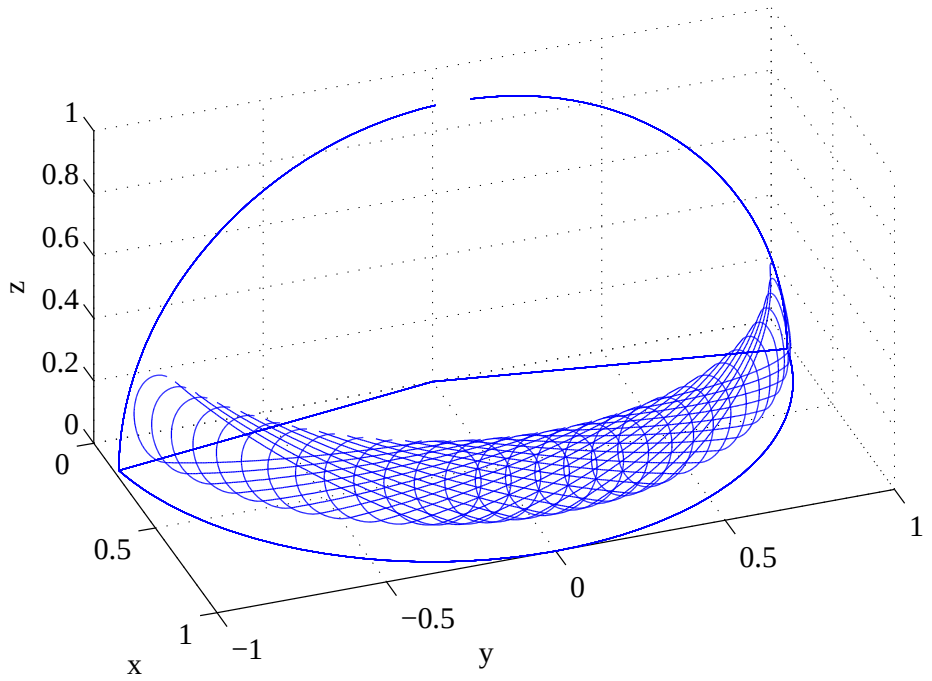

Figure 4.16 Horizontal trajectory parameterization

The drag coefficient of a kite with a dissimilar aspect ratio to that used in the present study can be calculated using

$$C_D{}' = C_D + \frac{{C_L}^2}{\pi}\left(\frac{1}{\mathcal{AR}'} - \frac{1}{\mathcal{AR}}\right) \tag{4.49}$$

where $C_D{}'$ corresponds to the drag coefficient of a wing of a new aspect ratio $\mathcal{AR}$ (Abbott & Doenhoff, 1959). It is assumed here that the kite is set so that the lift coefficient remains unchanged by the modified aspect ratio. The lift to drag ratio of a wing with modified aspect ratio is therefore given by

$$\frac{L}{D} = \frac{C_L}{C_D + \frac{{C_L}^2}{\pi}\left(\frac{1}{\mathcal{AR}'} - \frac{1}{\mathcal{AR}}\right)}, \tag{4.50}$$

To find the sensitivity of the kite system to aspect ratio, the derivative $\mathrm{d}\,F_A/\,\mathrm{d}(\mathcal{AR})$ is sought:

$$\frac{\mathrm{d}\,F_A}{\mathrm{d}(\mathcal{AR})} = \frac{\mathrm{d}\,F_A}{d\varepsilon} \cdot \frac{\mathrm{d}\,\varepsilon}{\mathrm{d}(L/D)} \cdot \frac{\mathrm{d}(L/D)}{\mathrm{d}(\mathcal{AR})} \tag{4.51}$$

for which equation 4.48, equation 1.12 and equation 4.50 are differentiated to obtain

$$\frac{\mathrm{d}\,F_A}{\mathrm{d}\,\varepsilon} = -\rho A C_F (V_A \cos\theta \cos\phi)^2 \frac{\cos\varepsilon}{\sin^3\varepsilon}, \tag{4.52}$$

$$\frac{\mathrm{d}\,\varepsilon}{\mathrm{d}(L/D)} = -\frac{1}{(L/D)^2 + 1}, \tag{4.53}$$

and

$$\frac{\mathrm{d}(L/D)}{\mathrm{d}(\mathcal{AR})} = \frac{{C_L}^3}{\pi \mathcal{AR}^2 \left[C_D + \frac{{C_L}^2}{\pi}\left(\frac{1}{\mathcal{AR}'} - \frac{1}{\mathcal{AR}}\right)\right]^2}. \tag{4.54}$$

where ε is in radians. Using, for example, $\rho = 1.19$, $A = 300\mathrm{m}^2$, $V_A = 6.18\mathrm{ms}^{-1}$, $\theta = 15°$, $\phi = 0°$, $C_L = 0.776$, $C_D = 0.128$, $C_F = 0.786$ and $\mathcal{AR} = 4.86$, table 4.3 was formulated using 4.51. The table shows $\mathrm{d}(FA)/\mathrm{d}\mathcal{AR}$ for a range of values of aspect ratio modified from the experimentally measured performance data in table 2.5.

Table 4.3 Effect of aspect ratio on aerodynamic force

$\mathcal{AR}$	$\varepsilon[°]$	L/D	FA $[10^4 N]$	d(FA)/d($\mathcal{AR}$) $[10^4 N]$
1	19.86	2.77	4.34	5.25
2	13.37	4.21	9.36	4.60
3	11.11	5.09	13.46	3.62
4	9.97	5.69	16.67	2.84
5	9.29	6.12	19.21	2.26
6	8.83	6.44	21.24	1.83
7	8.50	6.69	22.91	1.51
8	8.25	6.90	24.29	1.27
9	8.06	7.06	25.46	1.08
10	7.90	7.20	26.46	0.92

For the example input set, table 4 shows that increasing aspect ratio from 4 to 5 for example, results in a dramatically improved instantaneous aerodynamic force. 19.21×10^4 N is achieved instead of 16.67×10^4 N yielding 15% more aerodynamic force per unit increase in aspect ratio. There are other factors that require consideration in selection of kite aspect ratio, such as handling characteristics, stability and response in gusts. Anecdotal evidence (Hobbs, 1986) suggests that these are factors which would tend to favour lower aspect ratios.

4.7.4 Ideal angle of attack

The lift coefficient at which the kite operates has a significant influence on aerodynamic force; firstly through its direct influence on the lift generated, but also through a secondary effect due to the change in the operational L/D that accompanies a change in angle of attack. The optimum angle of attack for maximising aerodynamic force may be determined by considering Prandtl lifting line theory to establish a functional relationship that can be assessed analytically when combined with the zero-mass theory. If an increase in lift coefficient occurs together with an increase in lift to drag, the positive effect of each will be compounded. If an increase in lift coefficient accompanies a reduction in lift to drag, the effect will be negated. For a kite having a flat, eliptical planform, the optimum condition for maximised propulsive force occurs when

$$\frac{dF_A}{d\alpha} = \frac{\delta F_A}{\delta C_L}.\frac{\delta C_L}{\delta \alpha} + \frac{\delta F_A}{\delta (L/D)}.\frac{\delta (L/D)}{\delta \alpha} = 0 \tag{4.55}$$

From equations 1.7, 1.12 and 3.16,

$$\frac{\delta F_A}{\delta C_L} = \frac{1}{2}\rho A U^2 = \frac{1}{2}\rho A \left(V_A \frac{\cos\theta \cos\phi}{\sin\varepsilon} \right)^2 \tag{4.56}$$

and through combining equations 1.7, 1.12 and 4.50,

$$\frac{\delta F_A}{\delta (L/D)} = \left\{ -\rho A C_F (V_A \cos\theta \cos\phi)^2 \frac{\cos\varepsilon}{\sin^3\varepsilon} \right\} \cdot \left\{ -\frac{1}{(L/D)^2 + 1} \right\} \tag{4.57}$$

The 3D lift coefficient from Prandtl lifting line theory is

$$C_{L_\alpha} = C_{L0} + 2\pi \left(\frac{AR}{AR + 2} \right) \alpha. \tag{4.58}$$

The induced drag coefficient from Prandtl lifting line theory is

$$C_D = C_{D0} + \frac{{C_L}^2}{\pi AR e}. \tag{4.59}$$

Differentiating equation 4.58 gives

$$\frac{dC_L}{d\alpha} = 2\pi \left(\frac{AR}{AR+2} \right). \tag{4.60}$$

Then, combining equations 4.58 and 4.59 results in

$$L/D = \frac{C_{L0} + 2\pi \left(\frac{AR}{AR+2}\right) \alpha}{C_{D0} + \frac{\left(C_{L0} + 2\pi \left(\frac{AR}{AR+2}\right)\alpha\right)^2}{\pi ARe}}. \tag{4.61}$$

Differentiating equation 4.61 gives

$$\frac{d(L/D)}{d\alpha} = \frac{a-b}{c}, \tag{4.62}$$

where

$$a = \left(C_{D_O} + \frac{\left(C_{L_O} + 2\pi \left(\frac{AR}{AR+2}\right) \alpha\right)^2}{\pi ARe} \right) \cdot 2\pi \left(\frac{AR}{AR+2} \right). \tag{4.63}$$

$$b = \left(C_{L_O} + 2\pi \left(\frac{AR}{AR+2} \right) \alpha \right) \cdot \left(\frac{2C_{L_O} \cdot 2\pi \left(\frac{AR}{AR+2}\right)}{\pi ARe} + \frac{8\pi^2 \left(\frac{AR}{AR+2}\right)^2 \alpha}{\pi ARe} \right) \tag{4.64}$$

$$c = \left(C_{D_O} + \frac{\left(C_{L_O} + 2\pi \left(\frac{AR}{AR+2}\right) \alpha\right)^2}{\pi ARe} \right)^2 \tag{4.65}$$

Using $\mathcal{R} = 4.86$, $C_{D_0} = 0.05$, $C_{L_0} = 0.337$, $\rho_a = 1.19\text{kgm}^{-3}$, $A = 300\text{m}^2$, $V = 6.18\text{ms}^{-1}$, $\theta = 15°, \phi = 0°$, and $e = 0.9$, equation 4.55 was found to yield $\alpha = 15.28°$. This is the theoretical optimum as determined by Prandtl lifting line theory for these example input parameters, though there are other factors which might influence the best angle of attack for practical use. In particular, the way that the kite recovers from off-design flight conditions, such as stall, is likely to be significantly improved by mounting the kite to operate at a smaller angle of attack.

4.7.5 Pole separation and circle size

The effects of manoeuvre pole separation and pole circle size were investigated by comparing a series of different kite trajectories (See figure 4.17 and figure 4.18). Re-

sults were obtained through implementation of the flow chart in figure 4.6, including the effect of the wind gradient as determined by equation 3.1. The effect of increasing pole circle size and pole circle separation on time averaged force output is shown in figure 4.19 and in figure 4.20 respectively. These figures show that increasing pole circle size and separation both lead to a marked reduction of time averaged propulsive drive force since the manoeuvre is moved away from its optimal position for maximised propulsive effect. The limitation of these investigations is that no account is taken of the potential reduction in lift coefficient associated with canopy deformation and angle of roll during a tight turn. As yet, it has not been determined what the minimum turn radius might be, or what lift reduction could be expected during the turn.

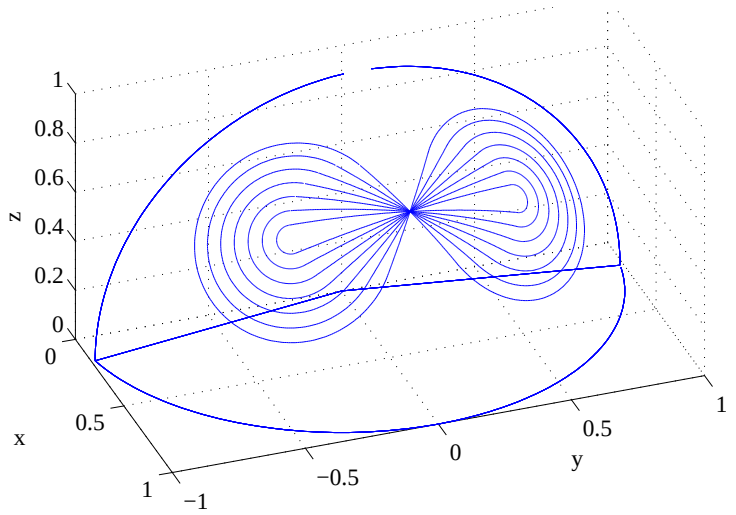

Figure 4.17 Trajectory shapes with different pole circle sizes

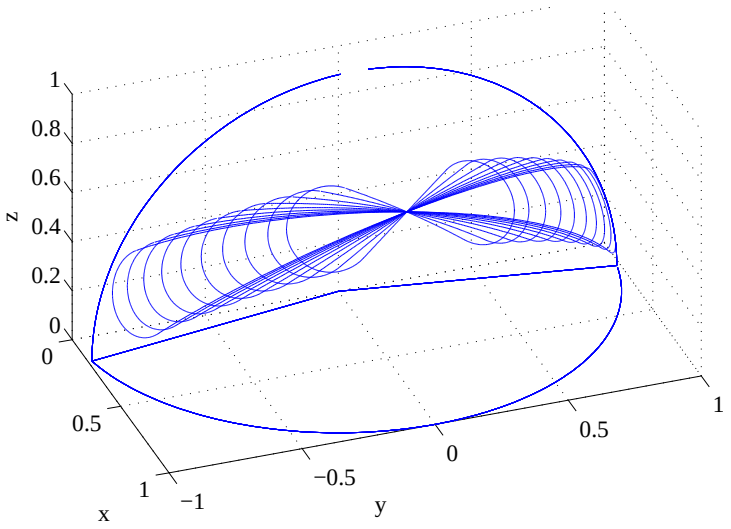

Figure 4.18 Trajectory shapes with different pole circle separation

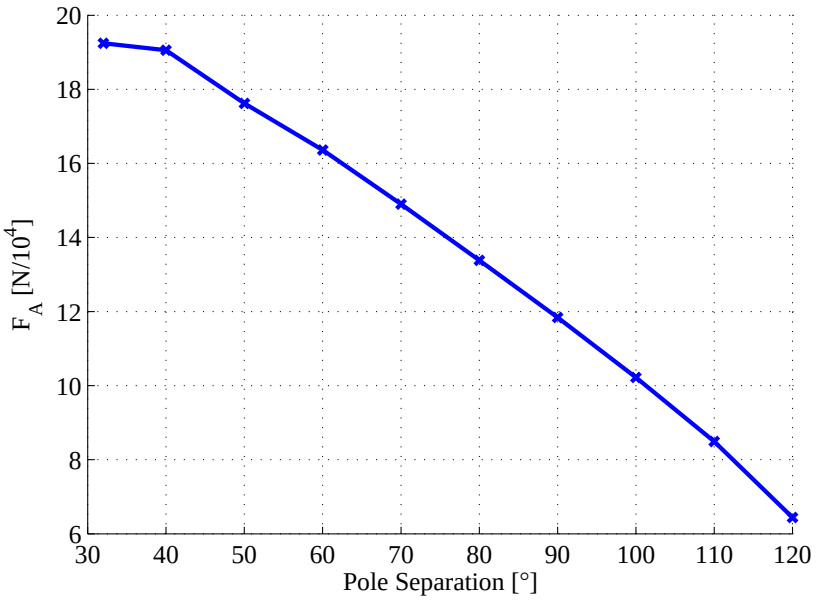

Figure 4.19 Force Reduction with circle size

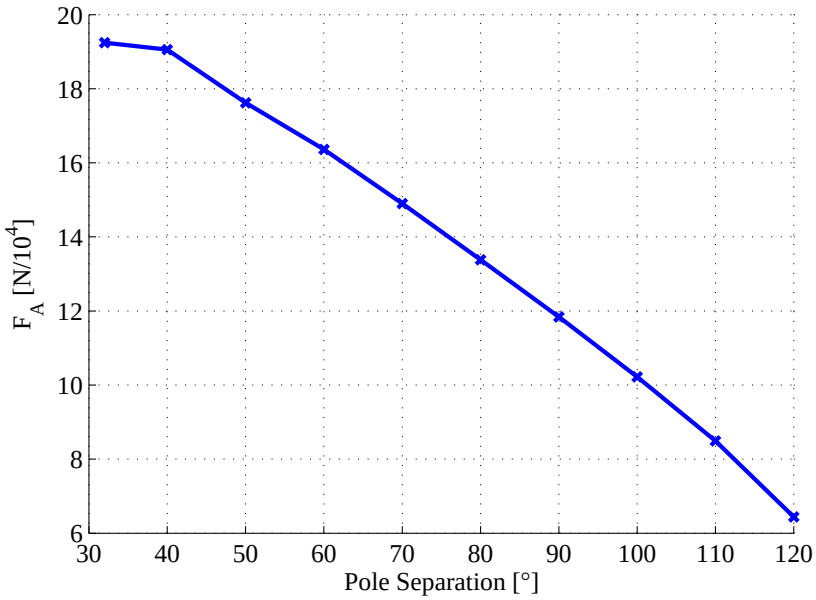

Figure 4.20 Force Reduction with Pole Separation

4.8 Conclusions

This chapter has presented a scheme for predicting time averaged kite forces together with a method for parameterising figure of eight shaped kite trajectories. The theoretical model was modified to allow a high degree of control over input manoeuvre paths in order to assess the effects of manoeuvre orientation, shape and true wind angle. The influence of the changing wind strength in the Earths natural boundary layer is included. The scheme has been implemented to show variation of onset velocity, kite velocity, onset angles and aerodynamic force for an example manoeuvre. In a case study with a 300m^2 kite, 300m long flying lines and 6.18ms^{-1} wind speed (at 10m), peak drive force up to 30×10^4N was predicted. A typical vertical figure of eight manoeuvre in the same conditions was shown to produce a time averaged horizontal drive force component 16.7 $\times 10^4$N. A complete force polar showing the horizontal component of aerodynamic force for different true wind angles has thus been obtained.

The calculation of kite velocity and the propagation of the kite around a theoretically defined manoeuvre have been validated by comparing a real recorded trajectory to a simulated one. The time scales for a theoretical and practical trajectory are shown to agree favourably, as do the magnitudes of minimum and maximum kite force.

The increase in wind with altitude is found to double the aerodynamic force compared to a hypothetical case with no wind gradient. Through considering the wind gradient in combination with kite motions, the optimum mean kite elevation angle for ship propulsion during dynamic flight was found to be 15°.

Horizontally orientated trajectories are shown to improve downwind performance by a factor of 1.4 compared to vertical ones, since the manoeuvre can remain closer to the optimum elevation angle for propulsion. Vertical manoeuvres are, however, preferred when good close winded performance is necessary.

By combining Prandtl lifting line theory with the zero-mass model, the derivative $dF_A/d\,(AR)$ was calculated at a variety of different aspect ratios. For the downwind dynamic flight condition, increasing the kite aspect ratio from 4 to 5, for example, was found to yield a 15% increase in drive force showing that force is highly sensitive to aspect ratio through its effect on kite L/D. Low aspect ratios may however be favourable to kite stability characteristics.

The angle of attack at which the kite operates modifies the aerodynamic force generated through its influence on lift and drag coefficients, but also through its effect on L/D. Optimising the angle of attack with respect to both of these yields $\alpha = 15.28°$.

Optimal trajectories were found to be those that are centred most closely to the best region of the flight envelope. Increasing both manoeuvre pole circle size and pole separation diminished the time averaged propulsive drive force arising. If the potential effect of reduced C_L during tight turns is negligible, the best manoeuvre is found to be a figure of eight shape with small circular ends and small pole separation, centred closely to an elevation of 15 degrees.

Chapter 5

Fuel Savings Prediction

This chapter describes the fuel savings prediction, due to a ship-borne kite propulsion system, using the kite performance models in chapters 3 and 4. Through consideration of kite dynamics, together with ship theory, the requirement was to establish the effect of various system parameters on the potential fuel saving benefit, and the financial performance of the kite propulsion system.

5.1 Background

Chosen ship speed is governed largely by ship operating economics (Buxton, 1971) such as commercial competition and fuel costs. Ship speed is therefore regarded as an *input* into the fuel savings calculation, to reflect commercial practice. The model is thus dissimilar to conventional *velocity prediction programs* such as that presented by Claughton *et al.* (1998). The fuel savings were computed according to the relative engine power reduction for the same speed.

In order to assess the fuel savings that can be achieved using auxiliary kite propulsion, a direct comparison is made between the rate of fuel consumption using engine only and the rate of fuel consumption when using kite and engine together. Molland & Hawksley (1985) discuss two possible modes of sailing for wind assisted propulsion; that of constant speed, and that of constant power. If two cases are compared for same engine power with and without wind assistance, ship speed will be increased due to wind assistance however the monetary fuel savings may not be realised unless there is a significant cost benefit for arriving sooner. Maintaining the same speed with wind assistance allows greater fuel savings to be directly realised since engine thrust is reduced, however this may be associated with reduced propeller efficiency. In the present study, fuel savings are computed for constant ship speed since the potential cost benefit of arriving sooner for constant power is less easily quantified.

The ship axis are defined according to a right hand rule, with the X axis along the centreline, and the Z axis vertically upwards. The force imparted to the ship via the kite line can be considered in terms of its components, F_x, F_y and F_z, along the X,Y and Z axis respectively and the moments, M_x, M_y and M_z, about the X,Y and Z axis respectively. Only the component of force which is along the ships track, F_x is considered to provide direct useful force for substituting engine thrust. The effective wind power, P_E is calculated according to Comstock (1967)

$$P_E = F_x V_s \tag{5.1}$$

Forces and moments that do not directly contribute to the drive force include the side force, F_Y, the lift force, F_Z, the yaw moment, M_Z, the pitching moment, M_Y, and the rolling moment, M_X. These components modify ship motions and therefore have a secondary effect on the resistance of the ship and thus influence the fuel saving.

The influence of the pitching motions due to M_Y and the rolling motions M_X on resistance are not considered in the present study. However, for real applications it will be important to quantify their effect on ship motions for safety.

The vertical component of kite force, F_Z, to some extent reduces the displacement of the ship and leads to a reduction in ship resistance. This influence is dependant on the particular trajectory adopted and the point of sailing relative to the wind. For large ships, where the lift force is very small in comparison to the weight, the effect on reduced displacement, and thus on ship resistance, is small and is therefore neglected.

The side force component F_Y must be reacted by the ship's hull requiring the generation of hydrodynamic lift which is associated with induced drag and therefore increases the ships resistance; the amount will vary depending on the chosen kite trajectory and sailing conditions.

The yaw moment M_Z is caused by the mounting position for the kite at the ships bow (Wrage, 2007a); this is longitudinally displaced from the centre of lateral resistance and will tend to yaw the ship to leeward. This moment must be counteracted by an equal and opposite turning moment created by a lift force at the ships rudder. This lift force is associated with an additional induced drag component.

Optimum engine fuel efficiency, for a given design speed, requires that the lowest feasible hull resistance is achieved together with the highest propulsive efficiency, thus the propeller design speed must be properly matched to that of the ship (Comstock,

1967). When an additional thrust is provided by the kite system, the propeller will operate at non-optimal thrust coefficient. A reduction in engine efficiency, due to the operation at lower power, will reduce the fuel saving attributable to the kite propulsion system.

5.2 Ship resistance components

Because equation 5.1 is not dependant on the ship resistance, obtaining the *absolute* value of the ship resistance is not of direct importance to the calculation of the kite substituted power and fuel saving. However, the *additional* hull resistance that is due to the presence of the kite must be accounted for. These components of resistance must be overcome by the combined kite drive force and engine thrust. Because the additional drag arises from deployment of the kite, this resistance force is subtracted from the kite drive force, F_X, before evaluating the fuel saving.

5.2.1 Influence of Froude number and Reynolds number

A dimensional analysis is presented by Comstock (1967) for obtaining three non-dimensional parameters on which the ship resistance is found to depend. These are the Reynolds number, Re= $\frac{\rho V L}{\mu}$, and the Froude number, Fn=$\frac{V}{\sqrt{gL}}$. For an ideal fluid, in which forces associated with the fluid viscosity do not exist, the residuary resistance, C_R (accounting for all non-viscous components), is found to be dependant only on the Froude number such that

$$C_R = \frac{R_R}{\frac{1}{2}\rho S V^2} = f\left(\frac{V}{\sqrt{gL}}\right), \tag{5.2}$$

where R_R is the residuary resistance, and S is the reference area. The gravitational constant, g, in the Froude number governs the wave pattern occurring at the free surface such that the part of resistance which is dependent on Fn is primarily associated with wave making effects. An alternative situation can be considered in which

there are only viscous forces and no wave making effects. This actually applies to a body deeply submerged in a real fluid, such that no surface waves are created. The resistance, R_F, associated with the fluids viscosity is found to be dependant only on the Reynolds number such that

$$C_F = \frac{R_F}{\frac{1}{2}\rho S V^2} = f_2\left(\frac{\rho V L}{\mu}\right). \tag{5.3}$$

A ship operating at the free surface, in a real fluid, has resistance components that are dependent on both Re and Fn. Furthermore, there are interactions between the resistance components such that the skin friction, which is primarily due to viscosity, exhibits some dependence on Fn, and wave patterns are to some extent modified by skin friction due to Re. However, in general, these interactions represent a small part of the total ship resistance. In experimental tests, model wave making resistance coefficients are approximately the same as a geometrically similar full scale ship provided the test is conducted at the same value of Fn, whilst resistance coefficients dependant on the viscosity are approximately the same as a full scale ship provided that tests are conducted at the same value of Re.

The total ship resistance can be considered as the sum of the components due to viscous friction, and the remainder which is predominantly due to wave making (equation 5.4). Energy dissipation through wave making can be equated to the energy in the wave pattern created by the ship, whilst energy lost to viscous friction and eddy making can be related to the rate of change of momentum supplied to the wake.

$$C_T = C_R + C_F \tag{5.4}$$

It is not possible to chose model scale values of both V and L that allow the full scale Re and Fn to be matched simultaneously at model scale. Various approaches are used to separate the resistance components and scale each independently. The most commonly used methods are due to Froude, and due to Hughes (these methods are given in detail by Molland *et al.* (2011)).

5.2.2 Froude scaling approach

To predict the full scale ship resistance, the practice first proposed by Froude is to conduct model resistance tests at the same Fn as the full scale ship to measure the total model ship resistance coefficient C_T. The component, C_F, is assumed to be only dependant on Rn and can be obtained based on experimental data for the skin friction on flat plates. The residuary component of resistance, C_R, is then obtained through use of equation 5.4. If it is assumed that the residuary component is predominantly due to wave making effects and only dependant on the Froude number, then the residuary coefficient obtained at model scale is unchanged at full scale. The full scale skin friction resistance can again be calculated using data from flat plates and added back to full scale C_R to obtain the full scale total ship resistance, C_T.

5.2.3 Hughes scaling Approach

Hughes recognised that the viscous resistance on three dimensional body is not identical to the viscous resistance on a two dimensional flat plate. He improved Froudes approach by introducing a factor $(1 + k)$ to the skin friction to account for the three dimensional influence of the form of the hull on the viscous resistance. When this method is used, part a of Froudes residuary resistance is considered to be due to viscous effects and is scaled accordingly with Rn, rather than Fn. Hughes' total resistance breakdown is given by

$$C_T = C_V + C_W = (1 + k)C_F + C_W \tag{5.5}$$

5.2.4 Scaling induced lift and drag

Neither Froude's nor Hughes' approach makes allowance for an induced component of resistance which arises due to the application of side force on the ship's hull. If side force is applied, such as that due to an oblique kite trajectory, the ships hull will tend to move laterally such that the hull adopts an angle of leeway. This leeway angle

is requisite to the generation of hydrodynamic lift. If a net sideways force exists on the kite and ship in combination, then the ships lateral motion and the leeway angle increase until the lateral aerodynamic and the lateral hydrodynamic forces are again in equilibrium. The lift is created at the expense of induced drag associated with circulation and the formation of shed vortices that modify the pressure distribution over the hull. Energy is dissipated in the wake due to viscous effects and some energy may be dissipated in the modified wave pattern. The induced drag, to some extent, negates the useful thrust from the forwards component of kite line tension and is later deducted from the drive force created by the kite.

A total resistance component breakdown is given by Molland *et al.* (2011) to include the induced drag, wave drag, viscous form drag and the skin friction drag separately, from which it can be put in coefficient form that

$$C_T = C_I + C_W + C_V + C_F \tag{5.6}$$

The way that these compoenents can be scaled is of particular interest to the present study so that model test results can be used to evaluate full scale resistance with the inclusion of induced drag.

5.2.5 Reynolds number scale effect on induced resistance

A study of the effects of flow past hulls at leeway has been carried out by Bradbury (1985) who investigated the influence of beam, draft and trim using a systematic series of hull like blocks to obtain the lift, drag and moment coefficients at different angles of leeway. Bradbury (1985) recorded the flow patterns around the hull using oil on models painted with a suspension of French chalk powder. It was found that the component C_I (found in equation 5.6) has a dependency on Re. This dependence was attributed to modified flow separation patterns. It is thought that this dependence of resistance on flow shape at leeway prevents accurate application of scaling laws for predicting full scale resistance based on model scale results. Whilst the viscous

component of resistance due to skin friction can be calculated in the usual way, the nature of flow separation and the resulting influence on the energy lost in the wake may be much harder to predict at full scale. Bradbury (1985) argues that the Reynolds number scale effect on C_I is likely to be small if either the flow separation patterns can be shown to be virtually unchanged for model and ship, or if the flow patterns can be contrived to remain unchanged. For the purposes of the current research, fuel saving calculations are made for a ship operating at typical Reynolds numbers Re= 10^9, whilst the model tests conducted by Bradbury (1985) are conducted at Reynolds numbers Re=10^6. Therefore, errors are likely to acrue by application of model scale test results at full scale.

5.2.6 Froude number scale effect on induced resistance

The experiments conducted by Bradbury (1985) were carried out using a double model in a wind tunnel and as such, there were no free surface effects or wave making resistance. The possible dependence of C_I on Fn is therefore of significant interest. Sharma & Bellows (1976) looked at the wave making of a ship moving along at an oblique angle of drift at speeds of $0.25 < \text{Fn} < 0.66$. They concluded that the asymmetric wave pattern did not appear to contribute at all to the extra drag at non-zero drift angles, however they comment that further tests such as wake surveys behind deeply submerged double models may be necessary to fully isolate free-surface effects due to circulation at leeway. Bradbury (1985) quotes the work of Gill (1979) who put 'it is interesting to note that forces are apparently not affected by Froude number in this range of angles of leeway up to 15°'.

From the preceding discussion, it is likely that the dependence of induced drag on Froude number will be small, however the dependence of induced drag on Reynolds number is likely to be significant, particularly at larger angles of leeway. The unknown

dependence of C_I on Re for the case study carried out in the present research remains a limitation that leads to some degree of uncertainty for the predicted fuel savings. However, if the induced drag is shown to represent a small percentage of the total drag, the error introduced in the fuel saving calculation by this uncertainty will also be small.

5.3 Ship propeller performance

With additional power supplied by the kite assistance the operating point of the propeller, and hence its efficiency, are altered. A discussion of these issues is given by (Molland & Hawksley, 1985). This potential change in propeller performance can be improved through use of variable pitch propellers, however in most cases the cost benefit is not likely to be worthwhile. Molland & Hawksley (1985) considered an example in which 50% of the thrust is derived through wind assistance, which leads to an increase in engine power of 7% for the same thrust, due to the propeller running in its off design condition (i.e. engine power was reduced by 43% rather than 50%). Conversely, the case study reported by Naaijen & Dallinga (2006) indicates an increase in propeller efficiency of 6.8%, for a study in which 32% of thrust is derived through wind assistance. The difference between these two cases is attributable to the different operating points of the propeller, before kites are deployed.

In the present study, An investigation of propeller performance is conducted to assess the potential impact of kite assistance on the operation of the ships engine. Propeller characteristics, corresponding to a Wageningen B4.40 propeller suitable for low speed ship forms, are assumed. Non dimensional performance coefficients for propeller thrust (K_T), torque (K_Q) and open water propeller efficiency (η_o) are each evaluated for different operating conditions as defined by the advance ratio, J, where the non-dimensional coefficients are defined by

$$J = \frac{V_a}{nD} \tag{5.7}$$

$$K_T = \frac{T}{\rho n^2 D^4} \tag{5.8}$$

$$K_Q = \frac{Q}{\rho n^2 D^5} \tag{5.9}$$

$$\eta_o = \frac{J K_T}{2\pi K_Q} \tag{5.10}$$

Assuming a pitch-diameter ratio $P/D = 0.8$, the approximate $K_T - K_Q - J$ design charts are constructed using Molland *et al.* (2011), who give

$$K_T = 0.320 \left[1 - \left(\frac{J}{0.9}\right)^{1.30}\right] \tag{5.11}$$

and

$$K_Q = 0.0360 \left[1 - \left(\frac{J}{0.98}\right)^{1.60}\right]. \tag{5.12}$$

The $K_T - K_Q$ propeller performance design chart is shown in figure 5.1.

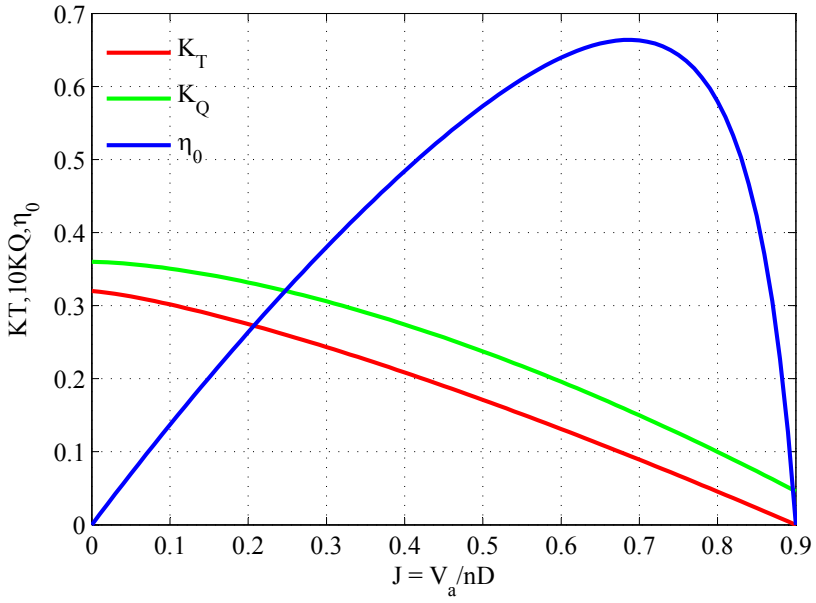

Figure 5.1 Wageningen B4.40 $K_T - K_Q$ propeller chart ($P/D = 0.8$)

Two initial propeller operating points are considered for the ship in the unassisted case. Firstly, the advance ratio, $J = 0.685$ is selected for peak efficiency at $V_S =$

11.5Kts. This speed corresponds to the average speed of the case study ship presented in this chapter. Secondly a reduced advance ratio, $J = 0.625$, is considered corresponding to a propeller that is pitched for greater ship speed. Different relative propeller revolution rates (n/n_1) are defined, where n is the possible revolution rate with kite assistance, and n_1 is the revolution rate without kite assistance. For constant ship speed, propeller diameter and sea density, the change in the advance ratio $(J/J_1{=}\eta_o/\eta_{o1})$ is obtained using equation 5.7. The relative change in the thrust coefficient, (K_T/K_{T1}) is established using equation 5.11. Re-dimensionalising this gives the relative propeller thrust reduction (T/T_1) corresponding to (n/n_1). Similarly, Q/Q_1 and η_o/η_{o1} are established through equations 5.12 and 5.10. The engine power reduction is obtained using

$$\frac{P}{P_1} = \frac{nQ}{n_1 Q_1} \tag{5.13}$$

Figure 5.2 shows the influence of kite propulsion on the engine performance characteristics by plotting the relative change in power, relative engine revolution rate, relative open water efficiency, and relative engine torque versus the fractional level of kite thrust assistance, established using

$$\frac{F_X}{R_{tot}} = 1 - \frac{T}{T-1}. \tag{5.14}$$

With increasing thrust assistance due to the kite, the engine revolution rate diminishes, together with the power and the torque (figure 5.2). In the case where the propeller is pitched at J = 0.685, the open water efficiency ratio $(\eta_o/\eta_o 1)$ remains close to 1 for $F_X/R_{tot} < 0.2$, falling by only $\sim 1.5\%$ compared to the unassisted case. For greater levels of thrust assistance, the open water propeller efficiency falls more rapidly. At $F_X/R_{tot} = 0.5$, efficiency is 12% lower than the unassisted cases. This reduction is however dependent on the initial operating point on the KT-KQ-J chart.

If the initial propeller operating point is with $J = 0.625$ the efficiency increases initially, as the kite thrust increases, and remains higher than the unassisted case

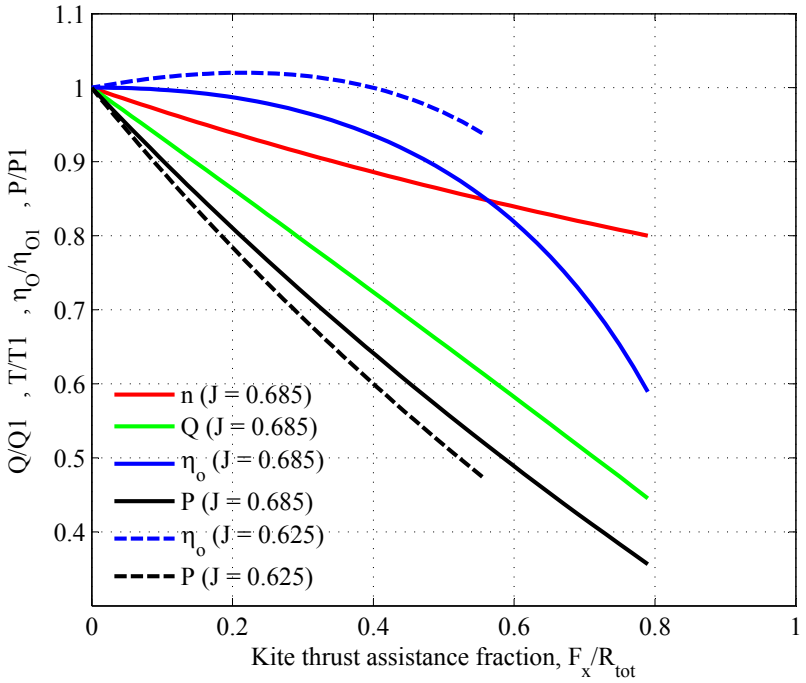

Figure 5.2 Effect of kite thrust on propeller revolution rate, on propeller torque, on open water efficiency, and engine Power (hence on fuel saving) for Wageningen B4.40 propeller ($P/D = 0.8$)

until $F_X/R_{tot} = 0.4$. This improvement is reflected in the corresponding relative power output shown in figure 5.2.

Additional to the influence of kite assistance on propeller performance characteristics, the specific fuel consumption at which the engine operates is also likely to be modified to a small extent. The work done by Chapman (2009) shows the specific fuel consumption increasing by 2.5%, for 10% thrust assistance level. The accurate determination of this influence on fuel saving will depend on the type of ship propulsion and requires careful consideration of the whole system.

5.4 Method for Calculating fuel Saving

This section presents the mathematical models and input parameters required to conduct the fuel saving calculation. Where data is not available, appropriate as-

sumptions are made to permit the calculation to proceed. The findings are therefore hypothetical, however they are sufficient to demonstrate the fuel saving performance in the general case. It is also suitable for establishing parameters which are of importance for maximising the efficiency of a kite propulsion system.

5.4.1 Input data

This fuel savings analysis is is structured in such a way that data from ships log books can be used to perform it. These data are

1. ships course, C [Compass]
2. ship speed, V_s [Kts]
3. wind direction, γ_c [Compass]
4. wind speed V_t [Beaufort].

Course and wind angles are in compass axis such that 0° corresponds to North. Similarly, vectors are presented in compass axis; the first term describes the Northing, and the second term describes the Easting. Wind direction bearings correspond to where the wind has come *from*, rather than where the wind is going *to*. For evaluation of the power saving, wind direction and ships course is converted using table 5.1, and wind speed is converted from wind Beaufort to [ms^{-1}] using equation 5.15 (Beer, 1997).

$$V_{t[ms^{-1}]} = 0.836 \times V^{3/2}_{t\,[\text{Beaufort}]} \tag{5.15}$$

5.4.2 Wind velocity triangle

The apparent wind speed vector, $\mathbf{V_A}$, located at the kite tether attachment is required to determine feasible kite trajectories and the possible corresponding propulsive forces. Specifically, the apparent wind velocity magnitude, V_A, is used in equation

Table 5.1 Conversion from compass rose to compass bearing [°]

Compass [Rose]	Compass [°]
N	0
NNE	22.5
NE	45
ENE	67.5
E	90
ESE	112.5
SE	135
SSE	157.5
S	180
SSW	202.5
SW	225
WSW	247.5
W	270
WNW	292.5
NW	315
NNW	337.5

3.16 for computing the kite onset velocity, whilst the direction of the apparent wind vector relative to the ship, β, determines the relative direction of the mean kite force. The apparent wind vector, $\mathbf{V_A}$, is the vector sum of the true wind, $\mathbf{V_T}$, and the wind due to ship speed, $-\mathbf{V_S}$, as shown in figure 5.3. The ships velocity vector is, in terms of the compass course, C, is

$$\mathbf{V_{sc}} = [V_s \cos(C), V_s \sin(C)]\,, \tag{5.16}$$

and the wind velocity vector in compass axes is

$$\mathbf{V_{tc}} = -[V_t \cos\gamma_C, V_t \sin\gamma_C]. \tag{5.17}$$

The apparent wind velocity vector is given by

$$\mathbf{V_{ac}} = \mathbf{V_{tc}} - \mathbf{V_{sc}}, \tag{5.18}$$

and its magnitude is

$$V_a = \mid \mathbf{V_{tc}} - \mathbf{V_{sc}} \mid . \tag{5.19}$$

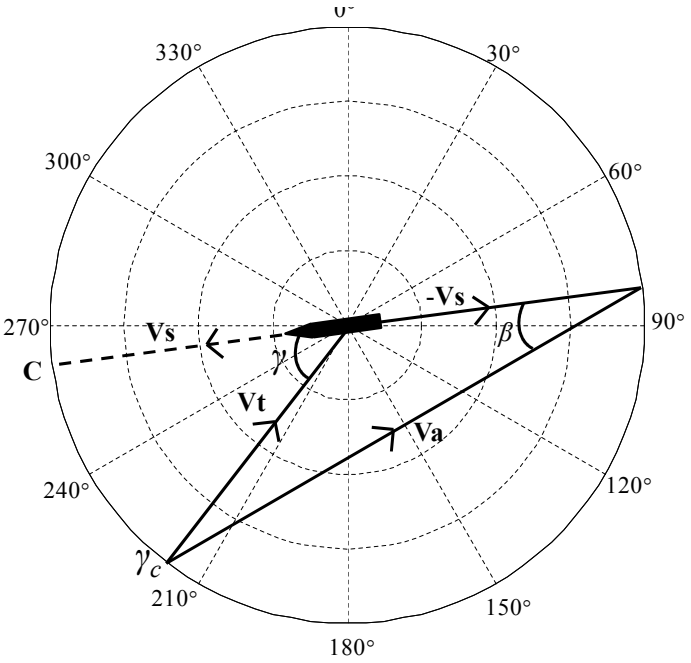

Figure 5.3 Relation of vectors in the wind triangle

For detemrination of relative forces, the true wind angle is converted into ships axis using

$$\gamma = \gamma_c - C \pm 360n, \tag{5.20}$$

where n is chosen such that γ lies in the range $-180 < \gamma \leq 180$. Lastly, the apparent wind angle in ship axis is given by

$$\beta = \cos^{-1}\left(\frac{\mathbf{V_{sc}} \bullet \mathbf{V_{ac}}}{V_{sc}V_{ac}}\right). \tag{5.21}$$

5.4.3 Force amplification coefficient for dynamic flight

Having determined the apparent wind components. It is required to establish possible relative kite forces corresponding to various trajectories.

Simplification can be achieved by using an unchanging kite force vector that is equivalent to the true time varying force that arises during dynamic kite flight. However, the power ouput according to equation 5.1 depends on a dynamically changing

kite thrust F_X, and also on the dynamically changing V_S, which varies as a function of F_X and ship dynamics. The simplifying assumption is made that the mass of the ship is large such that the ship speed is unchanging during the kite manoeuvre. Therefore, with V_S in equation 5.1 being steady, the time averaged kite force, F_X, can be used for calculating power output.

To avoid re-calculation of the time averaged kite force corresponding to different kite trajectories, a non dimensional force amplification coefficient, C_A, is defined,

$$C_A = \frac{F \cos\theta}{F_s}, \tag{5.22}$$

where the static kite force, F_S, is obtained using wind speed at an altitude of 10m; the dynamic kite force, F, is obtained using the altitude corrected wind speed from equation 3.1. The force amplification coefficient therefore takes wind gradient effects into account. The term $\cos\theta$ is used so that only the horizontal component of the time averaged kite force is considered.

Force amplification coefficients were obtained for two input sets; performance set 1 and performance set 2 (see table 5.2), where

1. for case 1 —Kite performance values were taken directly as those obtained experimentally for the test kite, Flexifoil blade III (see table 3.1). For consideration of a 320m^2 kite, Re scale effects were neglected such that C_L and C_D values were assumed unchanged.

2. for case 2 —The experimental data set in case 1 was modified to better represent a kite of aspect ratio used currently on commercial ships. The experimental data in (table 3.1) was modified to match the aspect ratio of the Skysails SKS320 system ($\mathcal{AR} = 2.5$) using equations 3.37 and 3.38. The kite is assumed to be trimmed to operate at the same C_L as for kite performance set 1.

	Case 1	Case 2
Span [m]	3.8	28.3
Area [m2]	2.98	320
$\mathcal{AR}$	4.86	2.5
Bridle [m]	41.6	-
Line Length [m]	28	300
Bridle diameter [mm]	1	-
$\varepsilon[^\circ]$	9.55	12.02
L/D	6.07	4.70
C_F	0.786	0.79
C_L	0.776	0.78
C_D	0.128	0.17

Table 5.2 Performance parameters for two different kite geometries

The trajectory shapes were selected on the basis of the optimised elevation described in section 4.7. No attempt was made to reduce pole circle size and pole circle separation because the practical minimum limits for these are not known. The defining parameters are shown in table 5.3 and the resulting trajectory shapes are shown in figure 5.4. The trajectory candidates are formed of 13 horizontal manoeuvres distributed between the theoretical limits (shown blue) and 6 vertical manoeuvres for providing propulsive force for courses sailed close to the wind (shown red).

Table 5.3 Input parameters for defining candidate manoeuvre shapes

Trajectory	θ_1	ϕ_1	α_1	θ_2	ϕ_2	α_2	η_1	η_2	η_3
1	0	-25	8	0	25	8	75	35	-61
2	0	-25	8	0	25	8	78	35	-55
3	0	-25	8	0	25	8	80	35	-45
4	0	-25	8	0	25	8	0	15	-42
5	0	-25	8	0	25	8	0	15	-35
6	0	-25	8	0	25	8	0	15	-28
7	0	-25	8	0	25	8	0	15	-21
8	0	-25	8	0	25	8	0	15	-14
9	0	-25	8	0	25	8	0	15	-7
10	0	-25	8	0	25	8	0	15	0
11	0	-25	8	0	25	8	0	15	7
12	0	-25	8	0	25	8	0	15	14
13	0	-25	8	0	25	8	0	15	21
14	0	-25	8	0	25	8	0	15	28
15	0	-25	8	0	25	8	0	15	35
16	0	-25	8	0	25	8	0	15	42
17	0	-25	8	0	25	8	100	35	45
18	0	-25	8	0	25	8	102	35	55
19	0	-25	8	0	25	8	105	35	61

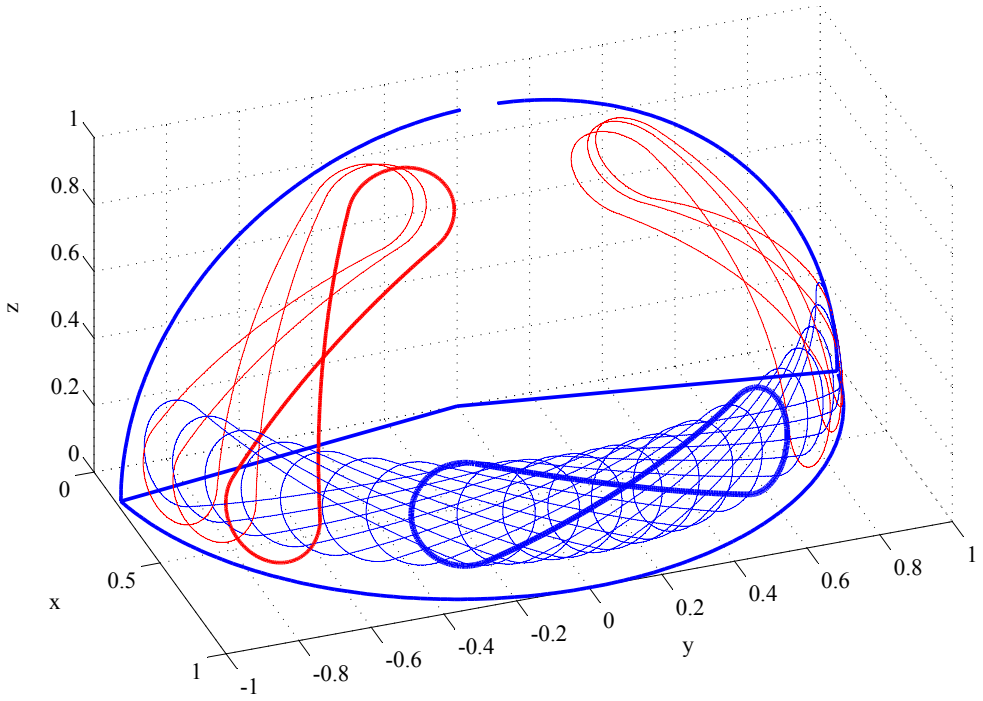

Figure 5.4 Candidate manoeuvres

For a given wind condition (β,V_A), the appropriate trajectory was to be selected from table 5.3 as that which produced the best fuel saving. For this, a lookup table representing the time averaged position angles (θ, ϕ), and the corresponding force amplification factor (C_A) was produced for each of the trajectory candidates, following a similar process to that described in section 4.3. The resulting force outputs are presented in table 5.4. The force amplification coefficients are plotted figure 5.5 for case 1, and for case 2.

Table 5.4 output position angles and force amplification coefficient for manoeuvres in table 5.3

	case1			case2		
No	θ	ϕ	C_A	θ	ϕ	C_A
1	56.3	59.3	4.56	61.9	60.2	1.95
2	51.2	53.8	7.37	52.9	53.9	4.30
3	44.5	44.3	12.86	45.5	44.2	7.90
4	18.9	37.8	17.18	19.4	39.5	9.83
5	17.6	31.6	24.93	17.8	32.3	15.58
6	16.7	25.6	31.44	16.8	26.0	19.95
7	16.0	19.4	36.90	16.1	19.8	23.54
8	15.6	13.3	41.07	15.6	13.5	26.28
9	15.3	7.0	43.73	15.3	7.1	28.03
10	15.2	0.7	44.74	15.2	0.7	28.69
11	15.3	-5.7	44.02	15.2	-6.0	28.13
12	15.5	-12.1	41.45	15.5	-12.4	26.52
13	16.1	-18.3	37.52	15.9	-18.7	23.89
14	16.7	-25.6	31.44	16.8	-26.0	19.95
15	17.3	-29.8	26.02	17.4	-30.6	16.22
16	18.5	-36.1	18.09	18.9	-37.9	10.32
17	44.5	-44.3	12.8	5 45.5	-44.3	7.90
18	51.2	-53.9	7.34	52.9	-53.9	4.27
19	56.4	-59.3	4.53	62.0	-60.2	1.94

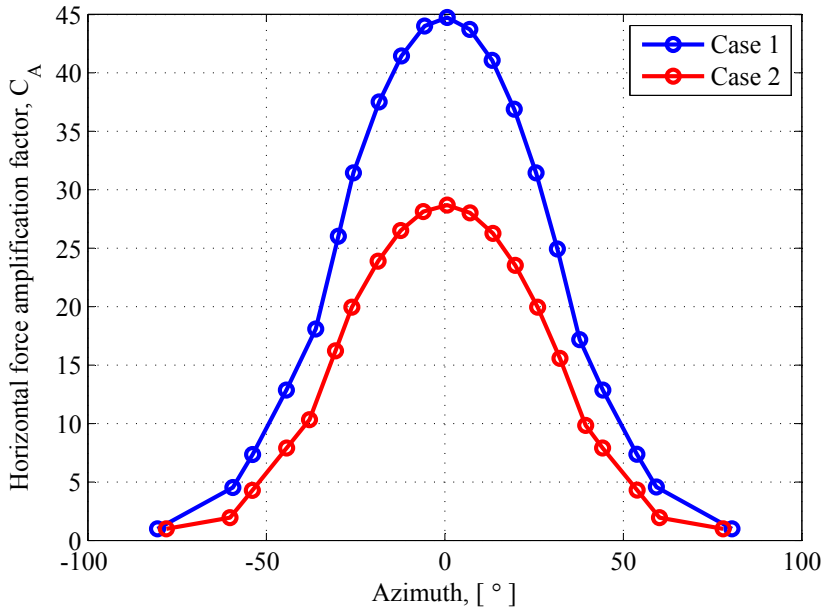

Figure 5.5 Force amplification coefficient for candidate manoeuvres

5.4.4 Ship performance data

Having defined the apparent wind, and the output forces for a variety of candidate manoeuvres, it was next required to characterise the expected performance of the ship hydro dynamically. This was achieved by assuming the results of Bradbury (1985), which were discussed together with possible limitation of scaling in section 5.2.6. These data provide side force coefficients, resistance coefficients and centre of effort for different hull dimensions using a systematic series based on a *mariner* hull form. Owing to the aforementioned limitations associated with scale effect on C_I, these data are only sufficient to establish the relative importance of induced drag for a typical kite ship combination. For a full investigation for a particular kite and a particular ship it is recommended that tank tests be conducted.

The length to beam ratio for the model is 6.87 and the length to draft ratio is 20.7. These are similar to the length to beam ratio and length to draft ratio for the ship used in the case study, 6.72 and 21.0 respectively. Similitude of these pa-

rameters is important since both are shown to influence the induced lift and drag characteristics of the hull (Bradbury, 1985). The assumed side force coefficient (C_S) and corresponding drag coefficients (C_D) are shown in figure 5.6. These coefficients are non-dimensionalised using $\left(\frac{1}{2}\rho_A V^2\right) \times \left(\frac{\rho_A}{\rho_H} L^2\right)$, where ρ_a is the density of air, ρ_H is the density of sea water and L is the characteristic length of the ship. Non-dimensionalising with these parameters is not conventional, however Bradbury (1985) had used this method to simplify his analysis.

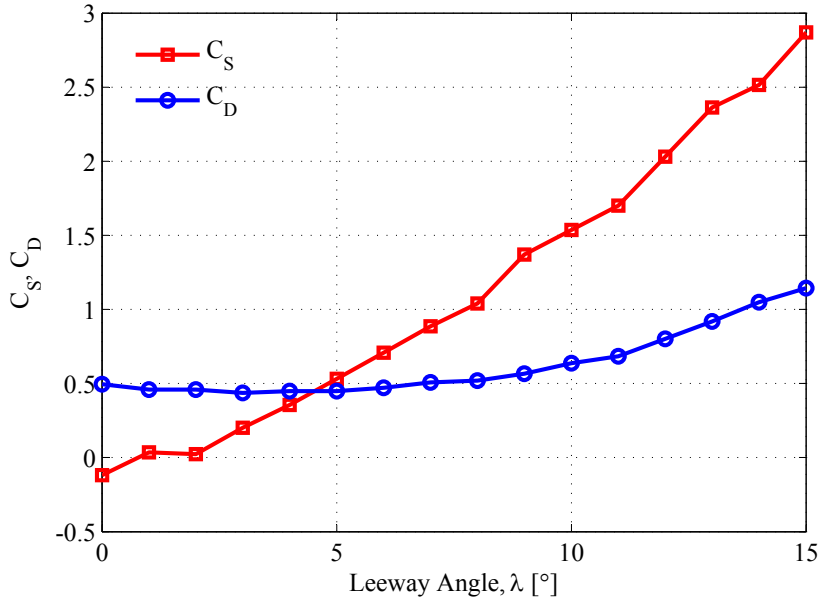

Figure 5.6 Lift and drag coefficients for Mariner ship hull at different angles of Leeway, data due to (Bradbury, 1985)

According to Prandtl lifting line theory, the induced drag is proportional to the square of the lift. This is corroborated in figure 5.7, where C_D is plotted with C_S^2. This enables a linear equation to be established from which the induced drag component can be determined according to the slope of the curve (figure 5.7) (Claughton *et al.*, 1998). If the ship is sailing at steady state, equilibrium of aerodynamic and hydrodynamic forces can be assumed such that the lateral aerodynamic force, and the lateral hydrodynamic force are in balance (i.e. $C_S = C_Y$). The induced drag can therefore be expressed as a function of lateral aerodynamic force by

$$C_I = 0.088C_S^2 = 0.088C_Y^2. \tag{5.23}$$

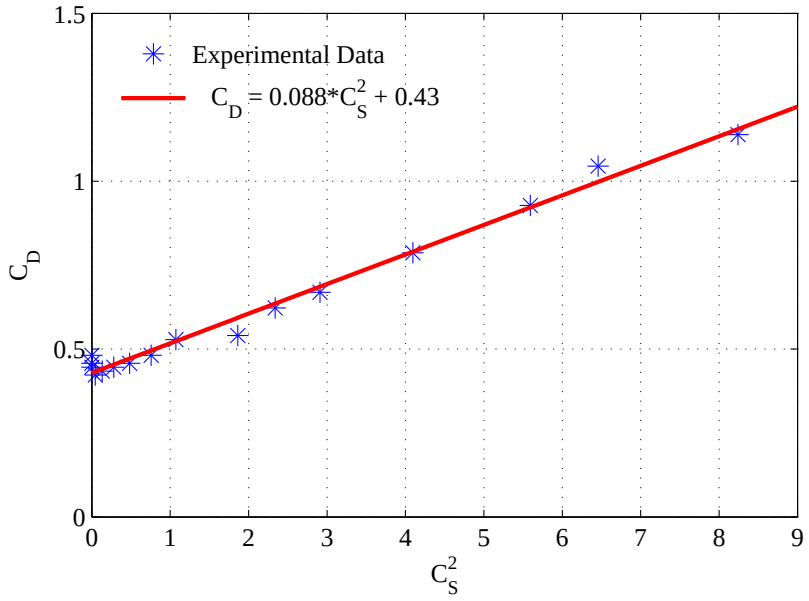

Figure 5.7 C_D versus C_S^2 for determination of induced drag ($C_{Di} = 0.088C_S^2$)

Note that the drag at $C_S^2 = 0$ (seen in figure 5.7) is discounted. This component of drag is present for the ship whether or not the kite is utilised; it is only the *difference* in drag due to the kite that is of interest for adjusting the relative fuel saving for additional kite induced drag.

5.4.5 Rudder loading and associated drag

Because the rudder is used to balance the yaw moment, M_Z, it was now required to estimate the contribution to drag due to the rudder deflection. The following rudder particulars were assumed: Section - NACA 0015; $\mathcal{AR} = 3$; taper ratio = 0.45; sweep angle = 0; tip shape $\sim$ square; and area = 92m^2. Experimental performance data for this rudder are presented in figure 5.8 (Wicker & Fehlner, 1958).

Prandtl lifting line theory provides a reasonably accurate means for predicting the effect of aspect ratio on lift and drag based on elliptical plan forms, however the

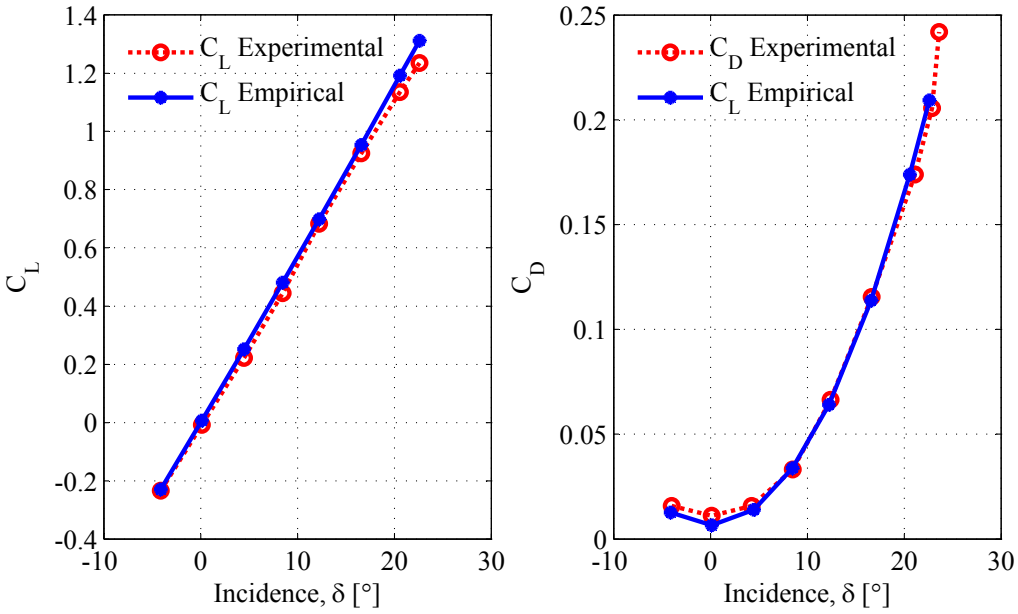

Figure 5.8 Lift and drag coefficients at different angles of incidence

work done by Wicker & Fehlner (1958) shows that the performance characteristics are dependent on additional factors such as sweep angle, effective aspect ratio, taper ratio and the Oswald span efficiency. Improved semi-empirical formulae are given to take these effects into account. The lift coefficient is given by

$$C_L = \left(\frac{\partial C_L}{\partial \alpha}\right)\alpha + \frac{C_{Dc}}{a}\left(\frac{\alpha}{57.3}\right)^2 \tag{5.24}$$

where

$$\left(\frac{\partial C_L}{\partial \alpha}\right)_{\alpha=0} = \frac{(0.9)(2\pi)a}{57.3\left[\left(\cos\Lambda\sqrt{\frac{a^2}{\cos^4\Lambda}+4}\right)+1.8\right]}$$

The drag coefficient is given by

$$C_{DR} = C_{d0} + C_{IR} = C_{d0} + \frac{C_L^2}{\pi a e} \tag{5.25}$$

The rudder lift and the corresponding induced drag are established through use of equation 5.24 and equation 5.25. These are plotted together with experimental results (Wicker & Fehlner, 1958) for the same rudder in figure 5.8 and are seen to agree favourably.

For a straight and steady ship, the net moments of forces acting on the ship hull are zero. Thus, the rudder loading required to balance the kite induced yaw moments is dependent upon the location of the hydrodynamic centre of effort; the hydrodynamic forces are balanced about this point. The centre of effort, non-dimensionalised by the water line length, for different angles of leeway is shown in figure 5.9 (Bradbury, 1985). A modification to these data was made because measurements for leeway angles $0° < \lambda \leq 3°$ were seen to display a large degree of scatter thought to be associated with poor measurement accuracy at very low side force. These were replaced with assumed data points based on a linear fit to the good part of the experimental data.

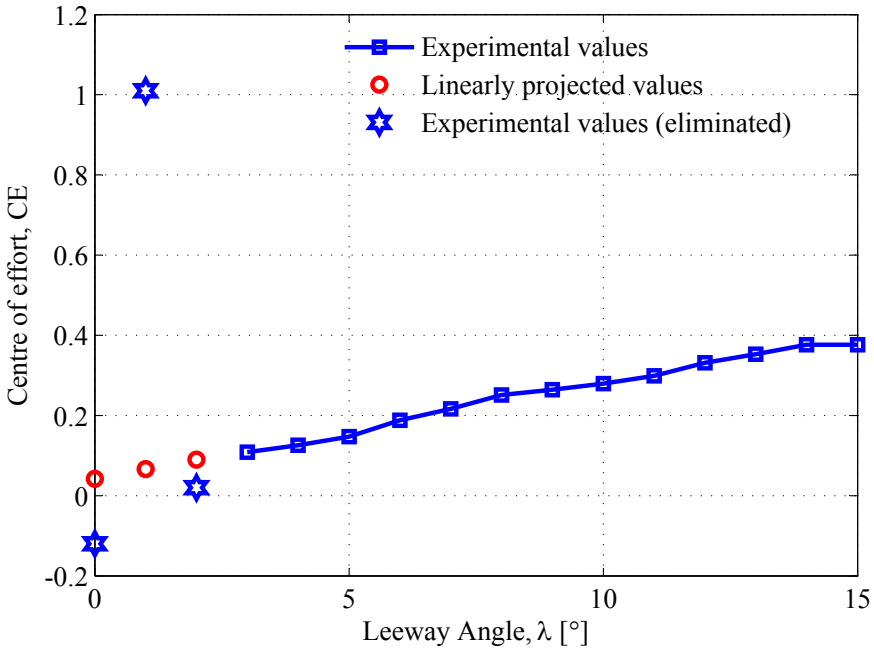

Figure 5.9 C_D versus C_L^2 for determination of induced drag

Commercial practice is to attach the kite to the ships bow, thus by taking moments about the centre of effort and non-dimensionalising the force using $\left(\frac{1}{2}\rho A_R V_S^2\right)$, the rudder lift coefficient required to balance the yaw moment is given by

$$C_{LR} = \frac{F_Y C_{CE}}{(1 - C_{CE})\left(\frac{1}{2}\rho A_R V_s^2\right)}, \tag{5.26}$$

For a given side force coefficient, the leeway at which the ship operates was established by means of a lookup table based on the data in figure 5.6. Then, based on that leeway angle, the centre of effort in equation 5.26 was obtained according to the data in figure 5.9.

The induced drag coefficient due the rudder deflection is then calculated using equation 5.25.

5.4.6 Kite delivered power

The physical components of induced resistance do not directly influence the kite thrust, however their effect is to reduce the fuel savings by increasing the resistance of the hull. This can be dealt with by considering that the effect of increased hull resistance is equivalent to a reduction in the thrust. The drive force due to the kite, the induced resistance due to the hull and the induced resistance due to the rudder are each re-dimensionalised and combined to yield the equivalent net drive force, on which the fuel savings calculation is based.

$$F_X = C_F \left(\frac{1}{2}\rho A_k V_A^2\right) \mathbf{f1} C_A - \left(\frac{1}{2}\rho_A V^2\right) \times \left(\frac{\rho_A}{\rho_H} L^2\right) C_I - \left(\frac{1}{2}\rho A_R V_S^2\right) C_{RI}. \quad (5.27)$$

Having considered wind effects, kite trajectory forces, and ship resistance components, these elements are combined in order to establish the fuel savings for a given wind condition (β, V_A). The unit apparent wind vector in ship axis is given by

$$\mathbf{v} = [-\cos\beta, -\sin\beta] \quad (5.28)$$

Selecting one manoeuvre from table 5.4, the unit direction vector for the time averaged horizontal force in ship axis is given by

$$\mathbf{f} = \mathbf{w} \bullet \begin{bmatrix} \cos\phi & \sin\phi \\ -\sin\phi & \cos\phi \end{bmatrix}, \tag{5.29}$$

and the magnitude is given by

$$F = \frac{1}{2}\rho_A A_K V_A^2 C_F C_A \tag{5.30}$$

The lateral aerodynamic force coefficient, C_Y is given by

$$C_Y = \frac{F\mathbf{f_2}}{\frac{1}{2}\rho A_K V_A^2} \tag{5.31}$$

The drive force coefficient, C_X is given by

$$C_X = \frac{F\mathbf{f_1}}{\frac{1}{2}\rho A_K V_A^2} \tag{5.32}$$

The drive force is modified to account for the induced resistance owed to the generation of lift from the ship and rudder.

$$F_X = \frac{1}{2}\rho A V_A^2 C_X - R_I - R_{IR} \tag{5.33}$$

The power delivered to the ship is then determined using

$$P = F_x V_s \tag{5.34}$$

The energy saved through substituting engine thrust is

$$E = P_E \times t \tag{5.35}$$

The fuel saving is calculated using a typical specific fuel consumption of *sfc*=0.25 litres/KWh delivered (Schlaak *et al.*, 2009). The *sfc* applies to the delivered power (P_D) at the tail shaft, however further propulsion losses are incurred before it can be equated to the effective power, P_E. The effective power is equivalent to that attained from the horizontal kite thrust. The quasi propulsion coefficient (η_D) accounts for the overall losses;

$$\eta_D = \eta_O \eta_H \eta_R = \frac{P_E}{P_D} \tag{5.36}$$

where η_O is the open water propeller efficiency discussed in section 5.3. η_H accounts for the effect of the hull on the inflow velocity and the influence of the propeller on the ships resistance, and η_R is the relative rotative efficiency accounting for the increased turbulence and the non-uniform flow field in the presence of the hull. Details for obtaining η_D are given by Molland *et al.* (2011). For the present study, a typical value $\eta_D = 0.625$ is used. From equation 5.36, the effective engine power is given by

$$P_D = \frac{P_{Ek}}{\eta_D} \tag{5.37}$$

therefore, using *sfc*=0.25litres/KWh,

$$F = \frac{sfc.E}{\eta_D} = \frac{0.25E}{0.625} \tag{5.38}$$

where the energy, E, is expressed in units of KWh and F is the kite equivalent fuel saving, output in litres.

5.5 Implementation and Results

This section presents the implementation of section 5.4 to investigate;

1. the properties of the wind triangle and important features that influence fuel saving potential;
2. the net drive force output by the kite when in combination with a ship for a general case;
3. the influence of ship speed on propulsion;
4. the influence of wind speed on propulsion.

5.5.1 Properties of the wind triangle

The properties of the wind triangle and their likely influence on fuel saving is considered independently of the other elements in the fuel saving prediction program. This enables those features which are exclusively due to apparent wind effects to be identified.

The investigation follows the implementation flow diagram in figure 5.10, based on the theory in section 5.4.2. The apparent wind *angle*, β, and the apparent wind *speed*, V_A, were calculated for different values of the true wind angle, γ. The calculation was repeated for different ship speeds, expressed as a fraction of the wind speed, $\frac{V_s}{V_t}$. The input true wind speed was 8.97ms^{-1}, chosen to match the case study presented later in this chapter. The results are displayed in figure 5.11 and figure 5.12, which shown β versus γ and V_A versus γ respectively.

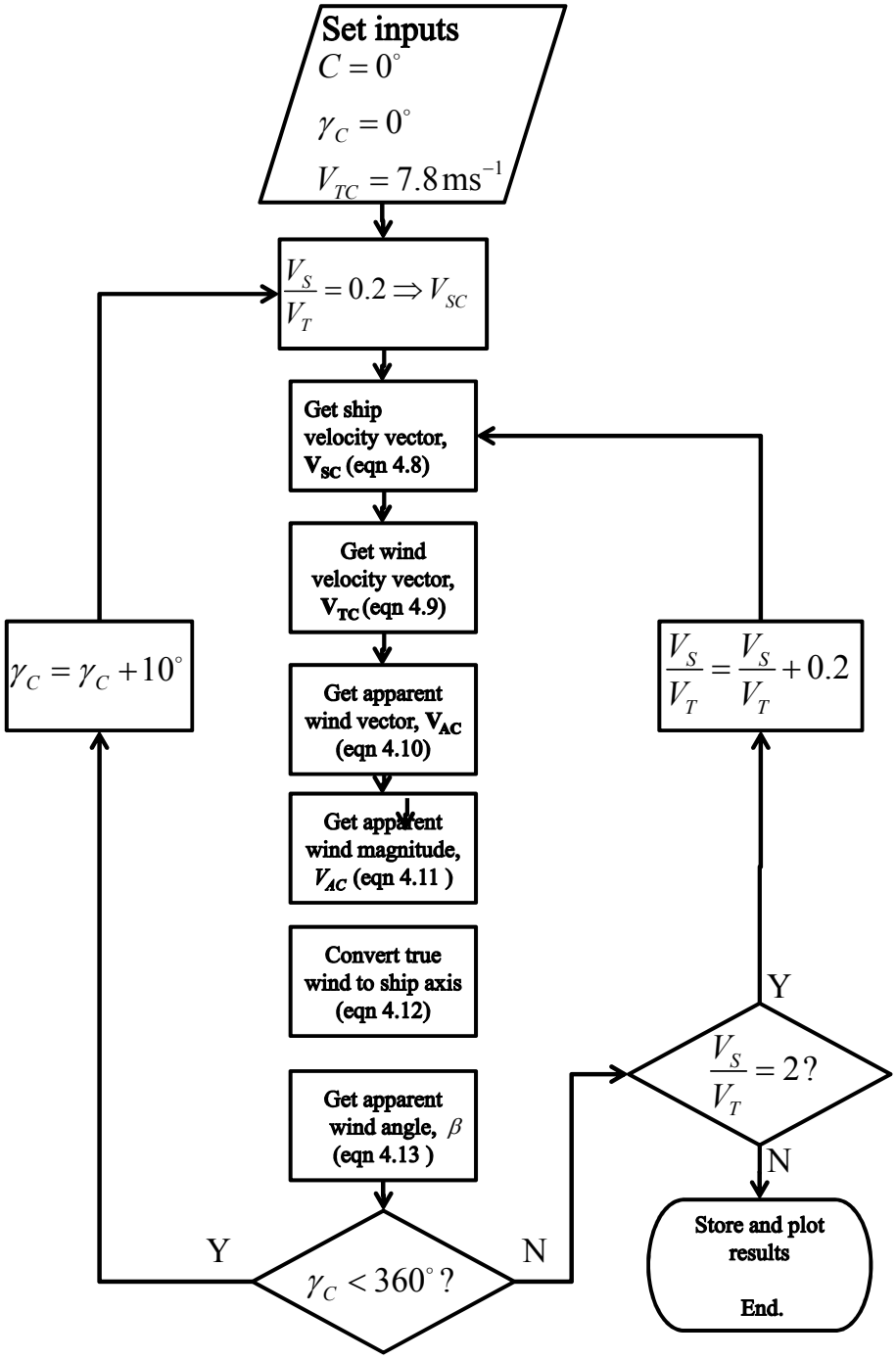

Figure 5.10 Flow diagram for implementation of apparent wind effects investigation

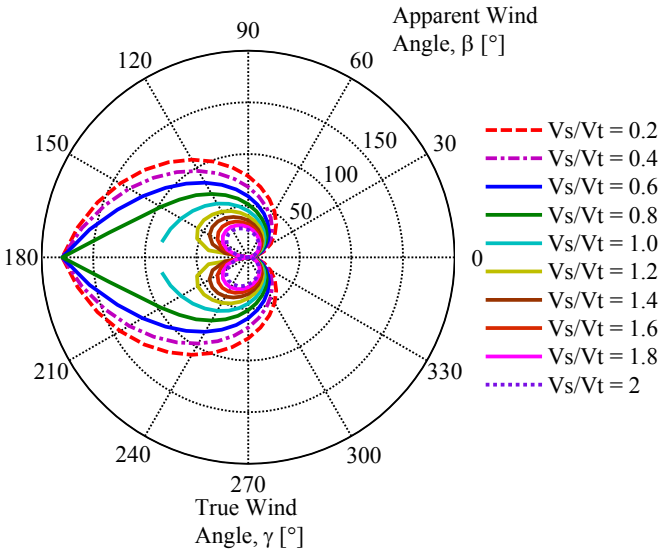

Figure 5.11 Apparent wind angles for different true wind angle and $\frac{V_s}{V_t}$ ratio

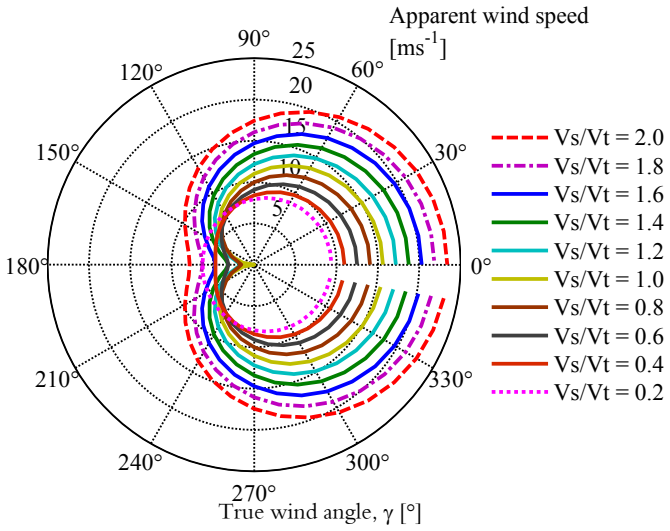

Figure 5.12 Apparent wind speed at $V_t = 8.97\text{ms}^{-1}$ for different true wind angle and $\frac{V_s}{V_t}$ ratio

The effect of the V_S/V_T ratio on apparent wind *angle* is shown in figure 5.11. It is seen that for faster ships with $\frac{V_s}{V_t} > 1$, the apparent wind angle, β, remains low for all true wind angles such that the wind is predominantly from ahead. Propulsive benefit and hence fuel saving is expected to be less for these faster ships because the apparent wind angle, β, is likely to fall within the usable range less often. For example, figure 5.11 shows that, if a typical kite system is limited to operating in $\beta > 50°$, it will never be used if $\frac{V_s}{V_t} > 1.2$. However, a more favourable apparent wind angle can be achieved by choosing a lower ship speed.

The effect of the V_S/V_T ratio on apparent wind *speed* is seen in figure 5.12. The apparent wind speed is adversely reduced by increasing ship velocity where the true wind angle is approximately in the range $120° < \gamma < 240°$. However for courses that are sailed closer to the wind, the apparent wind speed is increased favourably by increasing ship speed.

The influence of ship speed on apparent wind angle and speed affect the expected savings by their influence on equation 3.16, both via changes to V_A and changes to the kite azimuth angle, ϕ. To quantify the achievable savings in terms of fuel consumed or in monetary terms, these apparent wind effects are considered as inputs to the fuel savings program in the next section.

5.5.2 Net fuel effective drive force

The implementation flow diagram shown in figure 5.5.2 is used to establish the kite thrust, the induced resistance components and the net drive force for the input kite performance parameters shown in table 5.2. Two cases are investigated according to the input sets in table 5.5. Results are presented in figure 5.14). '[0:10:180]' is used in 5.7 to denote 10° increments between 0° and 180°.

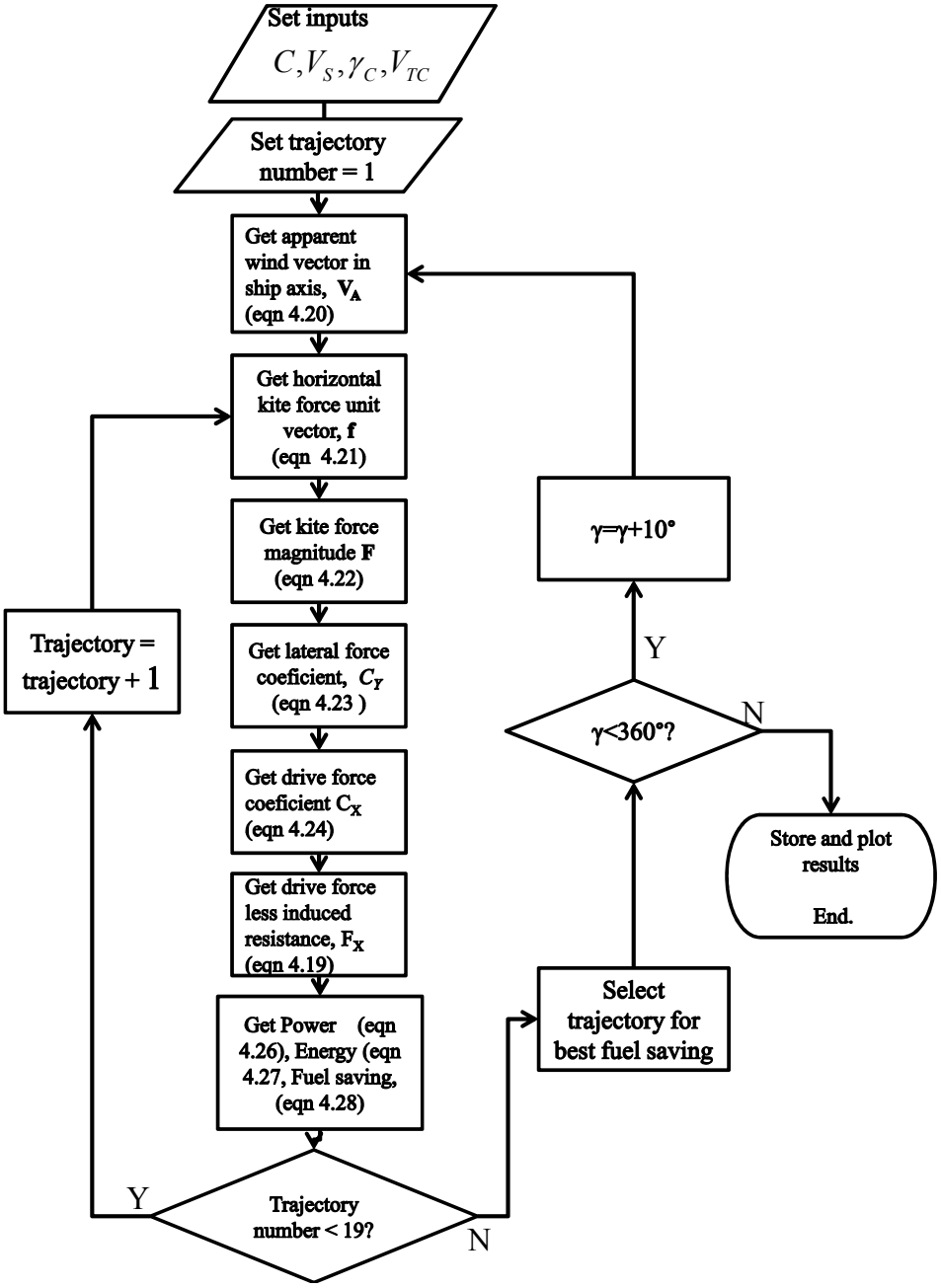

Figure 5.13 Flow diagram for implementation of fuel saving investigation

Table 5.5 Inputs for investigating influence of kite input parameters on effective thrust

$C[^\circ]$	V_S [Kts]	V_S [ms^{-1}]	V_T [ms^{-1}]	V_S/V_T	γ_C [°]	Kite Inputs
0	8	4.1152	8.97	0.46	[0:10:180]	Case 1
”	”	”	”	”	”	Case 2

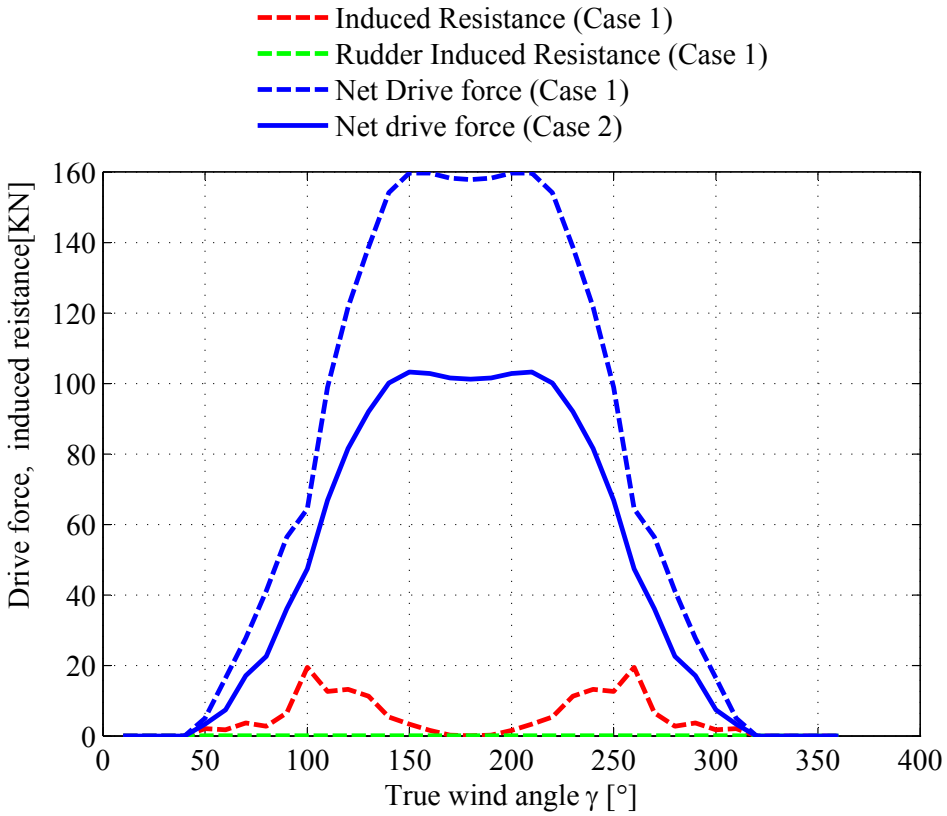

Figure 5.14 Net drive force and induced resistance components

The net fuel effective drive force was established for kite performance input sets 'case 1' and 'case 2', presented in figure 5.14. The net drive force is plotted for different true wind angles according to equation 5.27. The relative magnitudes of the hull and rudder induced resistance components are established via equation 5.23 (red) equation 5.25 (green) respectively.

The induced hull resistance varies with true wind angle. For $\gamma = 180^\circ$ the induced resistance is 0KN since there is no side force. The maximum absolute induced resis-

tance (7.5KN) occurs at $\gamma = 100°$ and accounts for a reduction to the thrust of 11%. This coincides with the maximum leeway angle (not shown) which is = 2.5°. For true wind angles sailed closer to the wind ($\gamma < 100°$) the absolute value of induced resistance diminishes, however it represents an increasingly large proportion of the net thrust, accounting for a reduction of 17.5% at $\gamma = 50°$, where the kite ceases to become effective.

The induced resistance arising due to rudder deflection is negligible and accounts for only 0.12% at its maximum value, owing to its small area compared to the hull and the close proximity to the bow of the lateral centre of effort.

Taking the induced resistance components into account, the net drive force for kite input set 'case 1' is found to be 160KN, whilst the net drive force for 'case 2' is 104KN. Although significantly greater power and fuel savings could be achieved using a kite having performance characteristics represented by case 1, these correspond to a high performance sports kite for which stability is not of paramount importance. For ship operation, in which kites must be reliably launched and retrieved using an automatic process, commercial practice appears, at present, to favour lower performance kites in favour of stability. All further performance calculations have made use of kite performance input set 'case 2' to take account of these observations.

5.5.3 Effect of ship speed on drive force, power, and fuel saving

The net drive force, the effective power and the fuel savings were calculated for all true wind angles, repeated for different *ship speeds*, V_S. The calculations follow the implementation flow diagram shown in figure 5.5.2 and are conducted for each of the input sets shown in table 5.6. Results are displayed in figures 5.15, 5.16 and 5.17.

Table 5.6 Inputs for investigating influence of increasing ship speed

C[°]	V_S [Kts]	V_S [ms-1]	V_T [ms-1]	V_S/V_T	γ_C [°]	Kite Inputs
0	10	5.144	8.97	0.57	[0:10:360]	Case 2
”	12	6.1728	8.97	0.69	”	Case 2
”	16	8.2304	8.97	0.92	”	Case 2
”	18	9.2592	8.97	1.03	”	Case 2
”	20	10.288	8.97	1.15	”	Case 2
”	22	11.3168	8.97	1.26	”	Case 2

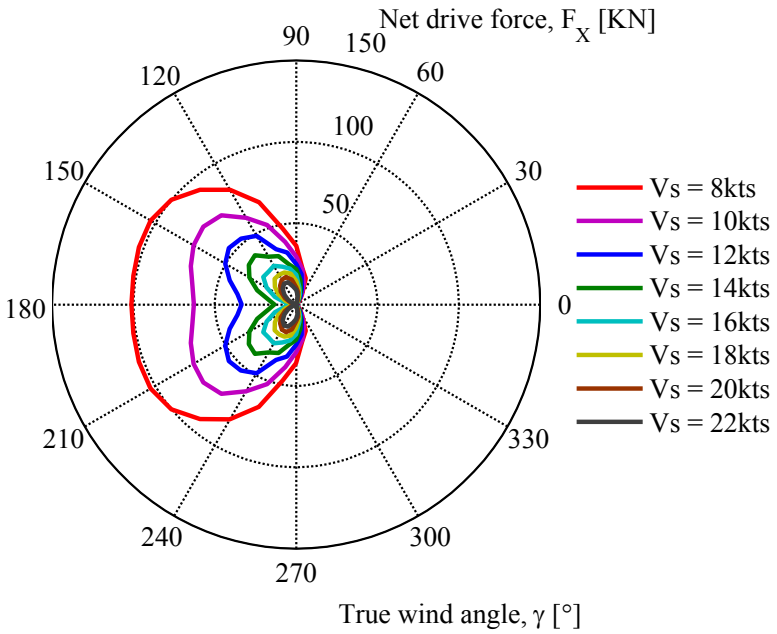

Figure 5.15 Drive force versus true wind angle for different ship speeds (see table 5.6)

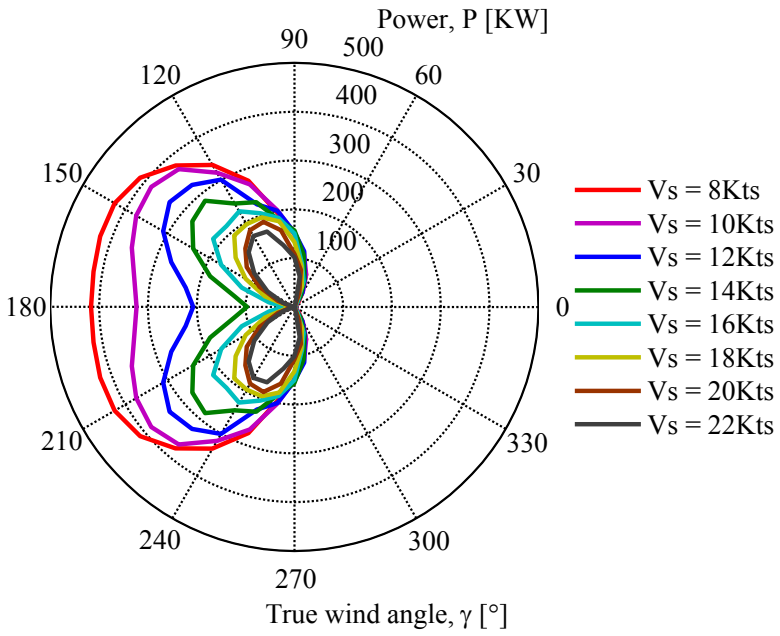

Figure 5.16 Kite delivered power versus true wind angle for different ship speeds (see table 5.6)

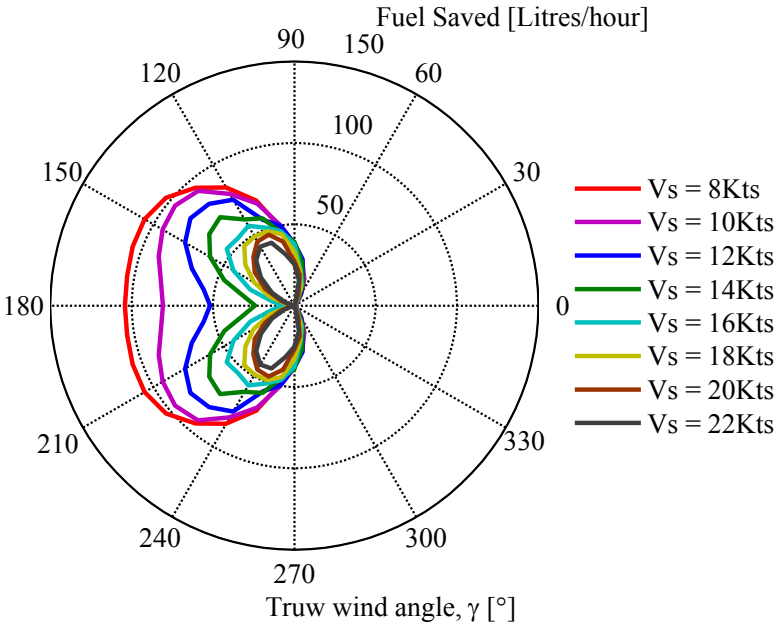

Figure 5.17 Fuel saving versus true wind angle for different ship speeds (see table 5.6)

The drive force is seen to reflect the findings from the apparent wind analysis; namely that faster ships suffer from reduced apparent wind speeds when sailing down wind and close winded performance is diminished compared to slower ships due to the influence of ship speed on apparent wind angle. For a ship operating at 22kts, the best achievable windward angle is 70° whilst for a ship sailing at 8kts, the best achievable angle to windward is 50°.

The figure shows that whilst windward course angles are feasible, the relative drive force compared to downwind course angles is small; for a ship sailing at $V_S = 8$kts, 3.2KN drive force is achieved at true wind angle $\gamma = 50°$ whilst 104KN is achieved at $\gamma = 180°$. The difference reflects the dynamic force amplification factors shown in table 5.4.

For low ship speeds, $V_S = 8$kts the drive force remains large for $240° < \gamma < 120°$, however for faster ship speeds, 12kts $< V_S <$ 22kts, there is a clear reduction in the range of true wind angles for which significant propulsive benefit can be derived. A ship sailing at 12kts is able to achieve net drive force $F_X > 50KN$ for $120° < \gamma < 150°$, however the thrust diminishes significantly outside this range owing to apparent wind effects. These limitations for higher speed wind assisted ships are not unique to kite propulsion however, the effects occur for almost all forms of wind assisted propulsion. The limitation iterates the importance of maintaining low ship velocities for improving propulsive benefit.

Figure 5.16 shows the kite delivered power. It is noteworthy that although the net drive force is significantly reduced by higher ship speeds, the power is reduced to a much smaller extent, owing to the contribution of the ship velocity in equation 5.34. This is also reflected in the fuel savings shown in figure 5.20.

Not taking into account loss of propeller efficiency, and using a typical specific fuel consumption of 0.25 litres per KWh, the figure shows that a ship operating at 12kts

sailing down wind is able to save 50 litres per hour. Whilst sailing at $\gamma = 130°$ a fuel savings rate of 81 litres/hour can be achieved. Reducing the ship velocity to 8kts allows a saving of approximately 111 litres per hour, for $\gamma = 130°$. These figures are obtained using a wind speed that is representative of average fuel saving conditions.

It is noteworthy that substantial fuel saving benefit is only achievable between $100° < \gamma < 260°$. This range accounts for 44.4% of the full 360° range of possible true wind angles and thus represents the percentage utilisation for a ship that sails on a truly randomised course with respect to true wind angles. Ships operating on regular routes will however be subject to prevailing wind conditions in that area, such that this utilisation rate will change accordingly. The case study in section 5.6 processes fuel saving calculation data based on real ships log operating conditions and therefore provides a precise indication of utilisation rate for that particular journey.

5.5.4 Effect of wind speed on drive force, power, and fuel saving

Drive force, power and fuel saving are calculated at all true wind angles and repeated for different *wind speeds*, V_T. The calculations are according to the flow diagram in 5.5.2 and use the inputs shown in table 5.7. Results are shown in figure 5.18, figure 5.19 and figure 5.20.

Table 5.7 Inputs for investigating influence of true wind speed

C[°]	V_S [Kts]	V_S [ms-1]	V_T [ms-1]	V_S/V_T	γ_C [°]	Kite Inputs
0	12	6.1728	4	1.54	[0:10:360]	Case 2
”	12	6.1728	6	1.03	”	Case 2
”	12	6.1728	8	0.77	”	Case 2
”	12	6.1728	10	0.62	”	Case 2
”	12	6.1728	12	0.51	”	Case 2
”	12	6.1728	14	0.44	”	Case 2
”	12	6.1728	16	0.39	”	Case 2

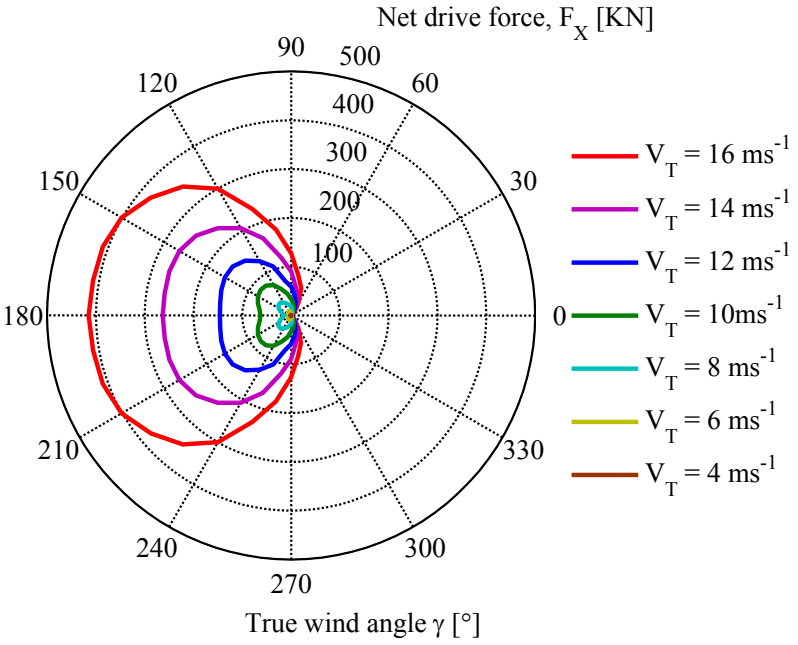

Figure 5.18 Drive force versus true wind angle for different true wind strengths (see table 5.7)

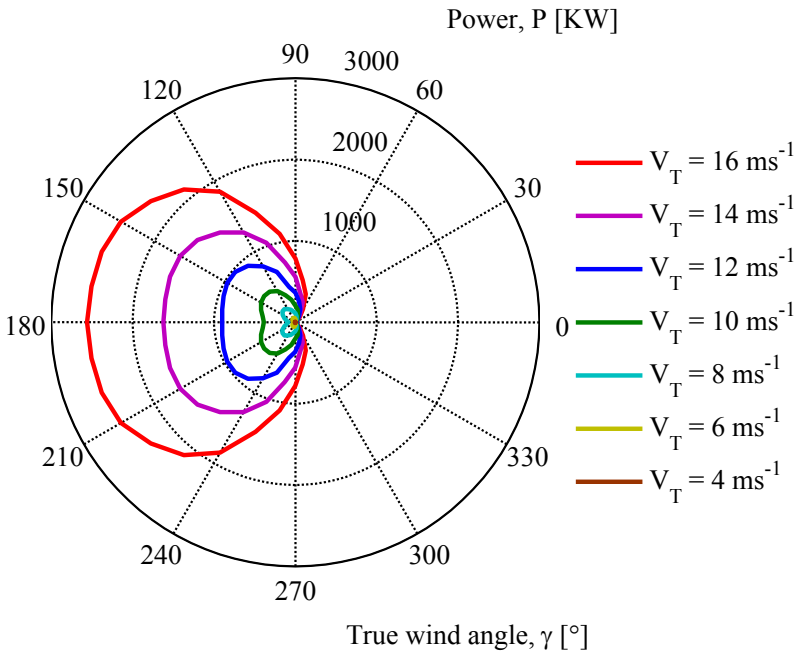

Figure 5.19 Kite delivered power versus true wind angle for different true wind strengths (see table 5.7)

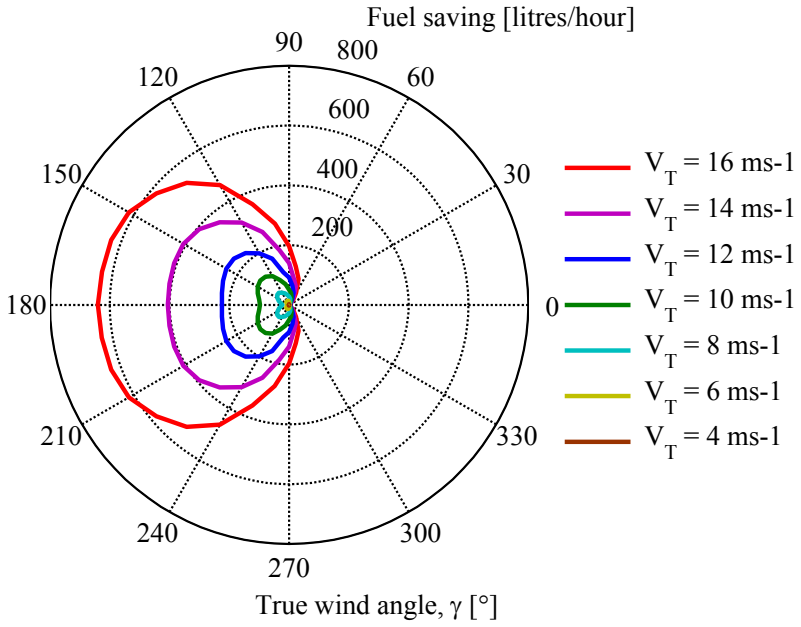

Figure 5.20 Fuel saving versus true wind angle for different true wind strengths (see table 5.7)

The power and fuel saving is seen to be highly sensitive to the wind speed such that for a wind speed of 16ms^{-1}, peak line tensions reach 414KN, Peak delivered power reaches 2.6MW and peak fuel savings can reach 640 litres per hour. These high wind speeds occur infrequently. However, the peak values are of interest for structural design of connecting elements. In practice, the peak line tensions can be moderated by elevating the kite trajectory. This upper wind speed corresponds to Beaufort force 7, which is deemed by Skysails to be the upper operational limit for use of the kite system (Wrage, 2007b).

5.6 Ship performance case study

This section presents the findings of the case study for fuel savings performance on the case study ship during her voyage from Loch Striven, UK, to Norfolk, Virginia, USA. The calculations are based on real data from the ships log during her voyage. The log data, together with the prossessed apparent wind parameters are shown in appendix B. These logged data are used to derive the ships position, together with the apparent wind strength and direction using the process shown in figure 5.10. The subsequent calculation of fuel savings are obtained by following the logic shown in figure 5.5.2. The ships hydrodynamic performance assumes that of section 5.4.4 and the kite performance characteristics correspond to case 2 (table 5.2). The force amplification coefficients are adjusted to correspond to a non-standard wind measurement altitude of 41m; the parameter Z_{ref}=41m in equation 3.1 leads to different amplification coefficients compared to when Z_{ref}=10m. The process is carried out for the outbound voyage according to the presented log data, and also for a hypothetical return voyage, in which the velocity vectors corresponding to each log entry were reversed. This is done to compare the performance for the ship sailing in opposite directions with respect to the winds prevailing on that voyage. The results arising from the analysis are presented in figures 5.21 to figure 5.30.

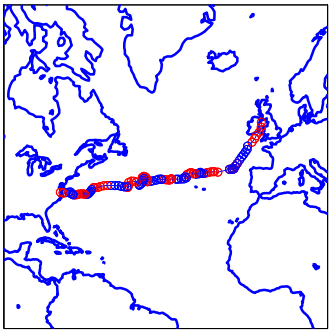

Figure 5.21 Shipping route

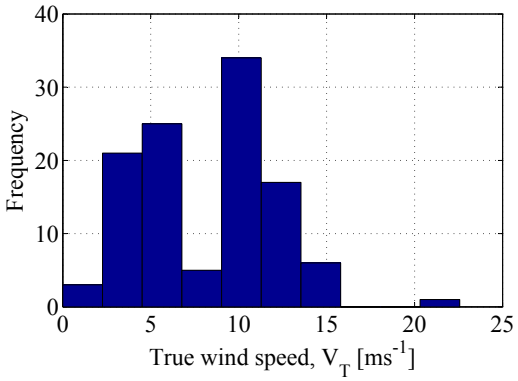

Figure 5.22 True wind speed frequency

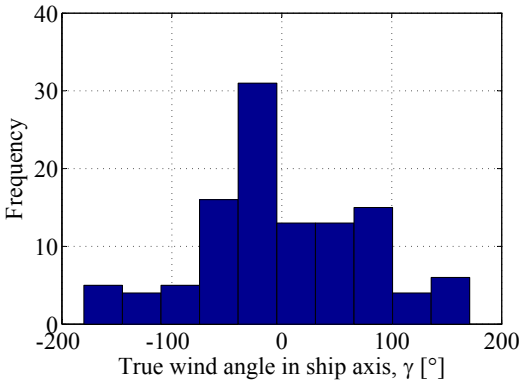

Figure 5.23 True wind angle (outbound)

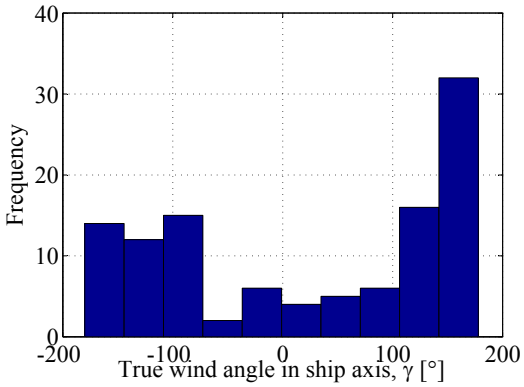

Figure 5.24 True wind angle (return)

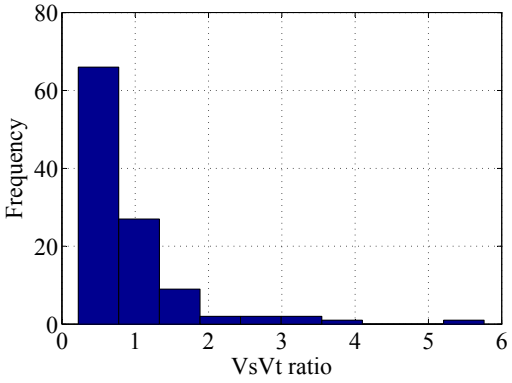

Figure 5.25 V_S/V_T frequency distribution

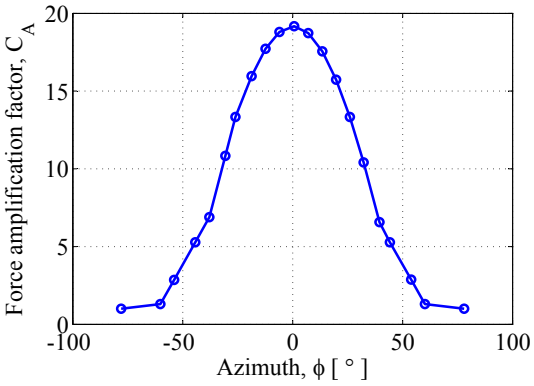

Figure 5.26 Amplification factor, C_A

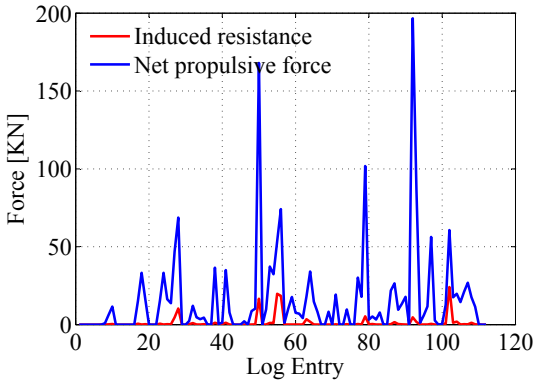

Figure 5.27 Net drive force (outbound)

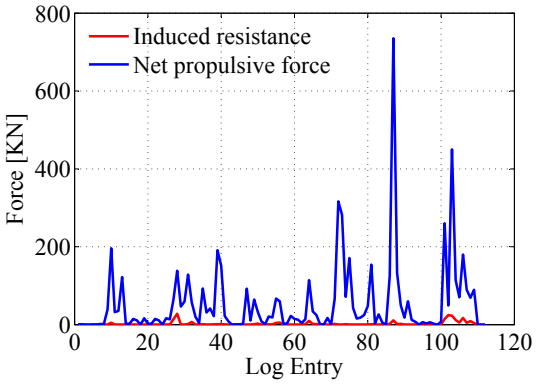

Figure 5.28 Net drive force (return)

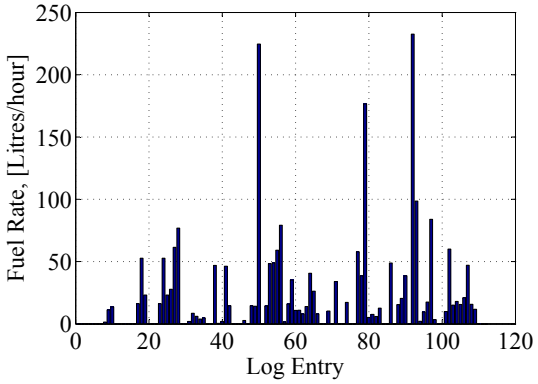

Figure 5.29 Fuel savings (outbound)

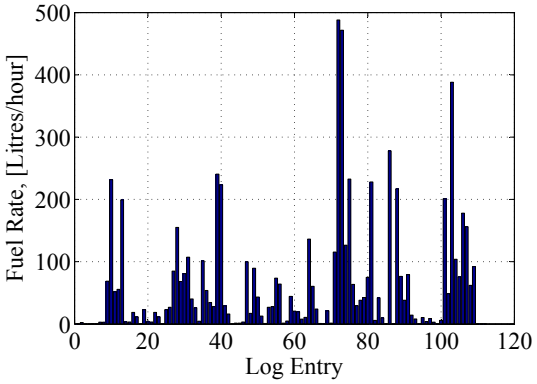

Figure 5.30 Fuel savings (return)

Figure 5.21 shows the ships position at 4h intervals with consecutive days plotted in red and blue. The wind data corresponding to each log entry are sorted into bins in order to present conditions for the journey in the form a frequency distribution. For reasons given in the previous paragraph, the wind strength is identical for both journey directions and is as presented in 5.22. Wind angle frequency distributions in ship axis are shown in figures 5.23 and 5.24 for the outbound and reciprocal journeys respectively. It is seen that the outbound true wind angle distribution is less favourable due to the high proportion of head winds occuring during the journey. Conversely the hypothetical reciprocal journey displays a high proportion of tail winds. The frequency distribution for $\frac{V_S}{V_T}$ is favourable for saving fuel owing to the larger proportion of the data having $\frac{V_S}{V_T} < 1$ (figure 5.25). The mean ship speed is 11.5 kts (5.9ms^{-1}) whilst the mean wind speed is 11.9ms^{-1} leading to a mean $\frac{V_S}{V_T}$ ratio of 0.5. Note that the log entries for which the kite is not usable, due to head winds, are empty in figure 5.29.

The force amplification coefficients are shown in figure 5.26. These data are dissimilar to those in figure 5.5 because the wind in the ships log is defined for an altitude of 41m, rather than the standard 10m. The net drive force for the outbound and reciprocal journeys are shown in figure 5.27 and figure 5.28 (note that Y axis scales are different). The outbound journey exhibits lower peaks (200KN versus 750KN) but is seen to incur a higher proportion of induced resistance due to close winded course angles. These differences reflect the dissimilar wind distributions for the outbound and reciprocal journeys. Figure 5.29 and figure 5.30 display the fuel savings corresponding to each log entry, with results corresponding to wind speeds in excess of Beaufort force 7 removed (note again the different Y axis scales). The mean fuel saving, including down time in which the kite is not used at all, is for the outbound journey is 45.4 litres/hour whilst for the return journey, it is 153.8 litres/hour leading to an average fuel savings rate for the round trip of 99.6 litres per hour. The total outbound fuel saving during the 19 day voyage is 20.4 tons, whilst the total return fuel saving is 68.9 tons.

5.6.1 Analysis of mean winds in the North Atlantic

In addition to using the real recorded log data. Typical winds at sea have been investigated for the months of April, July, October and January in order to give some indication of the fuel savings that may be expected in other months in the year. In all cases the identical route was followed for both outbound and reciprocal journeys. Mean wind trends for different positions along the shipping route were obtained using the Pilot Charts for the North Atlantic (NIMA, 2001). These data show wind direction frequency distributions binned into eight compass angles, each having a corresponding average wind speed for the month. Data are presented at every 5° intervals of latitude and longitude in the North Atlantic, and for each month in the year, based on historical data records (see figure 5.31). A computer script was implemented using Matlab plotting tools (Mathworks, 2009) to facilitate the conversion of these graphical chart data into numerical form using photographs. Initially April, the month of the voyage described in section 2, was analysed.

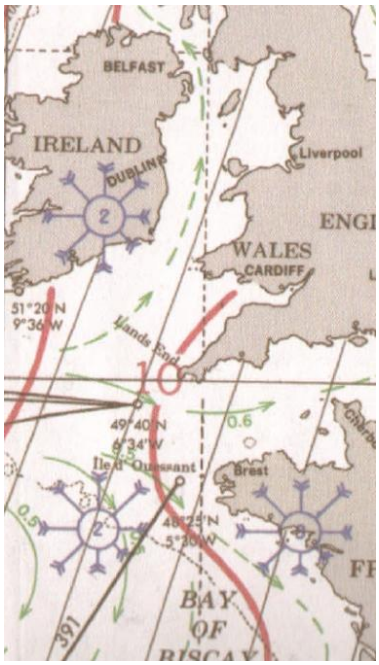

Figure 5.31 Wind strength and direction represented using wind roses, in which arrow length represents direction frequency distribution and number of feathers represents average Beaufort wind force. The number in the circle centre represents the frequency of flat calms (LighthousePress, 2001).

The kite thrust, (and hence power and fuel saving for fixed ship speed) varies with the *square* of the wind velocity; a unit increase in wind velocity above the mean influences the fuel saving to a greater extent than a unit decrease below. Therefore, in a fluctuating wind environment, to calculate results that are representative of average fuel savings, the root mean square (RMS) wind speed should be used, rather than the mean wind speed. The RMS value depends on the shape of the wind speed frequency distribution, not presented in LighthousePress (2001). Burton *et al.* (2001) find that typical winds at sea approximate a Weibull distribution having a shape factor $k = 2$. By evaluating the root mean square of this distribution, the RMS value is found to lie above the mean by a factor 1.15. This factor was applied to the LighthousePress (2001) data such that

$$RMS\left(V_T\right) = 1.15\bar{V_T}. \tag{5.39}$$

For the route shown in figure 5.21, a computer script was programmed to identify the closest wind rose according to the ships logged position, shown in the appended table B.9. Each wind rose along the route was used to establish the frequency distribution of wind direction, corresponding to each location along the route (see appended tables B.1, B.2, B.3, and B.4) and the corresponding mean wind strength (see appended tables B.5, B.6, B.7 and B.8). Mean kite drive force was established using the theory in section 5.4. The fuel savings were calculated based on a weighted average approach. A factor of 1.15 was applied to wind strength distributions to obtain the RMS wind strength for average fuel saving conditions. For example, the drive force in April during a 100 minute period for a ships position closest to rose number 1 for the month of April in tables B.1 and B.5 was be obtained as the mean drive force during:

- 9 minutes in Northerly wind at $6.69\times1.15\text{ms}^{-1}$
- 6 minutes, North Easterly at $6.69\times1.15\text{ms}^{-1}$
- 7 minutes, Easterly at $6.69\times1.15\text{ms}^{-1}$
- 12 minutes, South Easterly at $6.69\times1.15\text{ms}^{-1}$

- 18 minutes, Southerly at 6.69×1.15ms^{-1}
- 21 minutes, South Westerly at 6.69×1.15ms^{-1}
- 15 minutes, Westerly at 9.35ms×1.15ms^{-1}
- 11 minutes, North-westerly at 9.35ms×1.15ms^{-1}
- 1 minute, flat calm

The analysis of wind rose data was repeated for the months of July, October and January. The projected fuel savings for these months for the same journey are presented in table 5.9, together with fuel savings predictions for the real log data. The mean wind strength for all months was found to be 7.8ms^{-1}. Using equation 5.39, the RMS wind strength is found to be $V_T = 8.97\,\mathrm{ms}^{-1}$. The total journey duration was 18.6 days.

Table 5.8 Mean power for the case study ship for the voyage from Loch Striven, UK, to Norfolk, Virginia, USA, based on ships log data and re-processed for historic average wind distributions in the months of April, July, October and January. Total journey duration 18.6 days

Month and direction	Mean Power [KW] (320sqm kite)	Mean Power [KW] (600sqm kite)
April log outbound	91.0	170.6
April log reciprocal	307.8	577.1
April outbound	181.5	340.3
April reciprocal	341.3	640.0
July outbound	107.3	201.2
July reciprocal	60.5	113.5
October outbound	174.6	327.4
October reciprocal	302.7	567.6
January outbound	322.9	605.5
January reciprocal	778.0	1458.7
Mean outbound	196.6	368.6
Mean reciprocal	370.6	694.9
Mean power	283.6	531.8

Table 5.9 Fuel savings for the case study ship on her voyage from Loch Striven, UK, to Norfolk, Virginia, USA based on ships log data and re-processed for historic average wind distributions in the months of April, July, October and January.

	Fuel saving (320m^2 kite)		Fuel saving (600m^2 kite)	
Month and direction	tons	% fuel	tons	% fuel
log outbound (April)	16.3	2.37	30.6	4.4
log reciprocal (April)	55.2	8.02	103.4	15.0
April outbound	32.5	4.72	61.0	8.8
April reciprocal	61.2	8.90	114.7	16.7
July outbound	19.2	2.80	36.1	5.2
July reciprocal	10.8	1.58	20.3	3.0
October outbound	31.3	4.54	58.7	8.5
October reciprocal	54.2	7.89	101.7	14.8
January outbound	57.9	8.42	108.5	15.8
January reciprocal	139.4	20.26	261.4	38.0
Mean outbound	35.2	5.1	66.0	9.6
Mean reciprocal	66.4	9.7	124.5	18.1
Mean daily fuel save rate	2.7	7.39	5.1	13.9

5.7 Financial outlook using break even analysis

This section presents the findings for the fuel saving estimation using break even analysis, used to establish the estimated payback period for the kite propulsion system. German company 'Skysails' were contacted to establish estimated costs for system installation on which the analysis is based. Fixed costs include the initial outlay for system installation and one 320sqm kite. Variable costs include maintenance and kite replacement costs per year. The contribution is the average daily fuel saving for the year less the maintenance and kite replacement costs amortised over an estimated utilisation of 200 days per year. This utilisation rate accounts for days in which the ship is not in open waters and therefore not able to use the kite, even if wind conditions are suitable. This contribution determines the daily net return that can be considered to contribute towards the initial capital outlay. The average fuel saving conditions are for the 320sqm kite are those determined using table 5.9 using only historical average winds to establish a mean propulsive power value. System costs and are outlined in table 5.10.

Table 5.10 Fixed costs, Variable costs and contribution for 320sqm Kite

Fixed costs	£
Procurement and installation:	832,000
320sqm kite	83,200
Variable costs	£
Annual running costs, inc. Kite replacement and maintenance:	83,200
variable cost [£/day] (amortised over 200 days):	415
Daily Return from fuel saved	£
Price of fuel [/ton]: (on 22/02/2012) (IFO 380)	448
Tons fuel per day:	2.72
Daily fuel saving:	1220

The total cost incurred with time, TC, is estimated as the fixed costs plus the daily amortised variable costs, VC (annual variable costs / 200), times the number of days of utilisation, D,

$$TC = FC + \frac{VC}{200} \times D \tag{5.40}$$

The fuel saving revenue with time, R, is the average daily fuel saving, f, times the number of days utilised, D,

$$R = f \times D. \tag{5.41}$$

The revenue is additionally determined for 30% reduction of system utilisation (i.e. 140 days per year),

$$R_{70\%} = f \times D \times 0.7. \tag{5.42}$$

The total cost, TC, the Revenue, R, and 70%R have been plotted in figure 5.32. The break even points for R and 70%R can be identified at the intersection with the total cost line, TC.

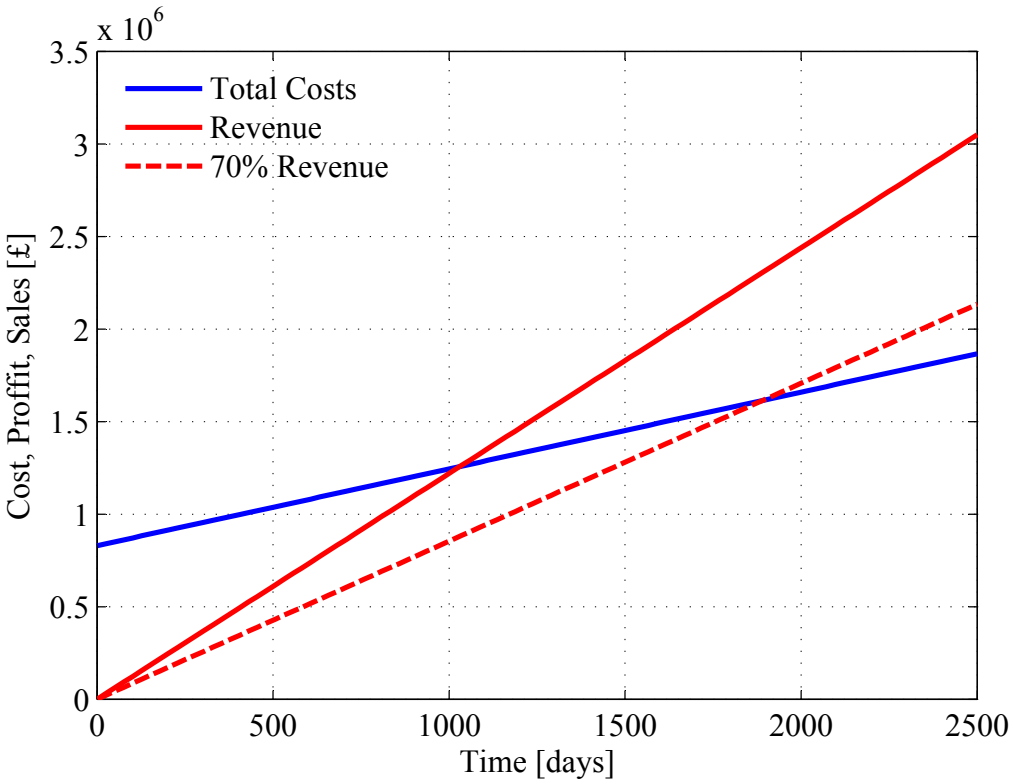

Figure 5.32 Break even analysis (LighthousePress, 2001)

With the predicted fuel savings potential being realised, the kite system is seen to break even after 1031 days. This would occur after approximately 5 years at a

utilisation rate of 200 days per year. For continued use thereafter, the system is seen to increase the profitability of the ship by (1220 - 415) 805 per day, compared to the unassisted case.

For the case where utilisation, or equivalently the price of oil, is reduced to 70%, the breakeven point occurs after 1890 days. At a utilisation rate of 200 days per year, the breakeven point would be reached in approximately 9.5 years. Thereafter, further profits would accrue at a rate of (0.7(1220) -415) 439 per day.

5.7.1 Discussion

Schlaak *et al.* (2009) studied the fuel saving potential on global shipping routes. The predictions were based on real kite force measurements taken during a period of one year, aboard the ship 'MS Michael A' using an 80m^2 kite. It was found that for a similar transatlantic route from the UK to the US, the mean outbound kite power was 180KW and the mean homebound power was 640KW leading to mean kite delivered power of 400KW. The present study has predicted an equivalent mean power of 284KW for similar conditions (see figure 5.9). The parameters which could account for these differences are numerous, however likely contributing factors are itemized as follows:

1. The present study has been conducted without directly knowing the kite performance characteristics for the skysails system. It has been shown in the optimisation study of section 4.7 that the results are highly sensitive to factors such as the kite aspect ratio and the lift coefficient. Small differences in the aspect ratio can lead to a relatively large difference in the kite thrust and hence calculated fuel saving. These are indicated by the value of $DF_A/D\text{Æ}R$ in table 4.3.

2. Differences in trajectory shape also lead to significant changes to the force amplification that can be derived. The trajectory shapes in this study have been optimised with respect to elevation and position for a given course angle sailed, however the pole circle separation and pole circle size have been arbitrarily chosen to reflect conservatively realistic values that were typical for the test kite flown on 28m flying lines. It is likely that for a kite on very long flying lines much tighter trajectories could be sustained. The advantages to this are illustrated in figures 4.17 and 4.17.

3. Schlaak *et al.* (2009) have not considered the effects of induced drag caused by the modified hydrodynamic performance. The induced drag diminishes for increasing downwind courses such that the additional resistance is minimum where kite drive force is maximum. The effect of neglecting it is therefore likely to small.

4. Although the shipping route adopted for the study is similar, the route studied by Schlaak *et al.* (2009) is further north such that prevailing wind conditions are unlikely to be the same. Further more, the respective studies have used different sources of wind data for fuel savings calculations.

Although the power performance estimation in the present study is 29% lower than that given by Schlaak *et al.* (2009) for similar conditions, with the above factors considered the difference is within the limits of uncertainty on system inputs.

5.8 Conclusions

The power delivered through kite assistance can be established as function of kite force and ship velocity such that the power and subsequent fuel savings can be obtained without directly knowing the complete ship resistance characteristics. However, the ship resistance is modified by induced drag whose value is dependent on hull shape, thus tow tank or wind tunnel experiments for a particular hull shape are required for accurate determination of induced drag. Experimental results for a mariner

hull shape have been used to determine the importance of induced drag in the overall force balance for a kite propelled ship. For downwind kite trajectories, the induced drag is negligible, however for cross wind courses ($\gamma = 100°$) where the induced drag is maximum, induced drag was shown to account for approximately 11% of the total ship resistance in this case study. The rudder deflection that is required to balance yawing moments is found to be small such that the added rudder resistance can be reasonably neglected for fuel saving calculations. The low additional induced rudder resistance was attributed to the close proximity of the kite attachment to the ships centre of lateral resistance such that yaw imbalance is relatively minor.

An investigation into the likely effect of kite assistance on propeller performance was conducted. It was found that in the case where 50% of the thrust is derived through kite assistance, the propeller efficiency is reduced by 12% compared to the unassisted ship at the same speed. However for a case where 20% of thrust is derived through kite assistance, propeller efficiency is not reduced by more than 1.5%. These values have been shown to depend on the initial operating point for the propeller. If the propeller is operating to the left of the optimum on a KT-KQ-J chart, and increase in propeller efficiency could feasibly be obtained for moderate levels of kite assistance.

The effect of operating at different ship speed to wind speed ratios has been considered. It is found that the propulsive benefit and hence fuel saving is less for faster ships due to reduced apparent wind angles with increasing ship speed and due to reduced apparent wind strength in following winds. It is found that for typical kite ship combinations, fuel saving benefit is restricted to ships operating slower than $V_S/V_T = 1$ and further fuel saving benefit is derived by operating at reduced ship speed.

The rate of utilisation for kite propulsion is dependent on the frequency of suitable wind strengths and wind angles. It is found that for a ship sailing on a truly randomised course with respect to true wind direction, an utilisation rate of 44% is

typical; however, this value will vary depending on prevailing wind conditions for a particular journey.

A case study has been implemented for a 32,000 dead weight ton ship using real recorded log data. Outbound and return fuel savings were found to be 20.4 tons and 68.9 tons respectively during the 18.6 day voyage. A study of typical wind conditions during the year was conducted by considering historical winds on the same journey. Annual average fuel savings for outbound and return voyage were calculated to be 2.7 tons per day, leading to a financial pay back rate of £1220 per day at the current day oil price of £448/ton. By considering commercial system costs, this leads to a financial break even period for the system of approximately five years.

Chapter 6

Conclusions

6.0.1 Original contributions and summary

Experimental methods have been newly implemented for measurement of static flight performance characteristics and for recording dynamic flight time histories. Measurement error was found to be less than 0.73% for kite position angles and 1.36% percent for load measurement over the operable range, identified with 95% confidence.

For the test used in the current study (Flexifoil blade III 3m^2), the static performance parameters are lift to drag ratio, $L/D = 6.07 \pm 0.5$, and lift coefficient $C_L = 0.77 \pm 0.05$. These are established with 95% confidence. It has been shown that higher L/D induces higher onset velocities, favourable to generating line tension, but potentially with detriment to favourable stability characteristics.

The importance of mass in the analysis of kite flight was newly investigated by comparing two kite flight models with, and without, the inclusion of mass terms. It was concluded that mass alters dynamic behaviour of kites when flight is not fully initiated to its natural velocity at which close equilibrium of line tension and aerodynamic force occurs; this applies during launch and during aerodynamic stall. However for fully initiated kite flight, where equilibrium of forces is closely obtained, mass can be neglected for approximating line tension during dynamic kite flight. Neglecting mass brings with it some important simplifications that allow kite flight to be modelled in a computationally in-expensive way, which is likely to be beneficial for the implementation of kite control algorithms in real time.

Using a new theoretical model, that included the effects of mass, the variation of individual flight performance parameters during launch were newly established. These included kite lift to drag ratio, L/D, kite velocity and onset wind velocity, lift and drag coefficients, and line tension.

It was shown that the exclusion of mass terms implies that the lift to drag ratio, L/D, and the lift coefficient, C_L, remain constant during dynamic kite flight. Using the obtained values L/D and C_L, the experimentally measured line tensions during dynamic kite flight was shown to compare favourably to those obtained theoretically. This comparison, together with the investigation two kite performance models, has lead to the first validation of a mathematical model for predicting dynamic kite line tensions during dynamic kite flight.

A scheme for parameterising figure of eight kite flight trajectories has been presented, together with a model for integrating dynamic line tensions around theoretically defined trajectories in order to obtain a time averaged force. The rate of progression, around the manoeuvre due to the calculated kite velocity was validated by comparison to experimental results. This lead to the determination of a new kite force polar diagram based on theoretically defined manoeuvres.

A new optimisation study was carried out in which it was determined that the optimum mean kite elevation angle, for ship propulsion during dynamic kite flight, was found to be 15°. Horizontal manoeuvres were found to increase the time averaged propulsive drive force compared to vertical ones, however vertical figure of eight trajectories were required for providing good performance on windward sailing courses. Line tension was found to be increased for kites having higher aspect ratios due to influence on lift to drag ratio. The optimum angle of attack for maximising line tensions during dynamic flight was found to be 15.28°.

The power derived by application to a ship was theoretically obtained using a newly developed fuel savings prediction scheme, without directly knowing the complete ship resistance characteristics. The relative importance of induced drag was established, together with losses due to rudder deflection and due to potentially reduced propeller efficiency. At its maximum value, induced drag, due to lateral kite forces, was found to be approximately 11% of the drive force due to the kite. Losses due to rudder deflection were shown to be negligible, and the altered propeller performance was shown to either increase, or decrease depending on the initial operating condition for the unassisted ship.

A case study was implemented for a 32,000 dead weight ton ship using ships log data. Outbound and return fuel savings were found to be 20.4 tons and 68.9 tons respectively during the 18.6 day voyage. A study of typical wind conditions during the year was conducted by considering historical winds on the same journey. Annual average fuel savings for outbound and return voyage were calculated to be 2.7 tons per day, leading to a financial pay back rate of £1220 per day at the current day oil price of £448/ton. By considering system costs, it was estimated that for a ship operating in the North Atlantic, the payback period for the capital outlay on the kite propulsion system was found to be 5 years.

6.0.2 Future Work

Having identified a mathematical model with experimental validation, further work could be conducted to minimise the errors that have been attributed to spatial and temporal wind variations that occur in natural, non-zero winds. This would require a testing program to be conducted exclusively on days of zero wind. One has to take the opportunity to conduct testing when ideal near-zero winds arise and this necessitates having a test facility that is always ready. The elimination of variation due to the natural wind would significantly improve the quality of the results obtained and enable the accuracy of the mathematical models to be determined more accurately. The work in this theses has focused exclusively on kite dynamics for a given set of statically determined flight performance characteristics. It would be beneficial to examine how the geometry of the kite itself can be modified in order to maximise propulsive benefit. Additionally, further work could be conducted to establish the turning characteristics of the kite theoretically, rather than imposing pre-defined kite trajectories. This would be a required step to enable kite autopilot design.

6.0.3 Concluding Remarks

The aim of the work was to establish a validated mathematical model for evaluating the flight performance of tethered kites when flown around three dimensional trajectories. This has been achieved by comparing two dissimilar theoretical models with experimental results. The subsequent aim was to establish an additional model that determines the fuel saving potential when a kite propulsion system is applied to a ship for assisted propulsion. This was achieved by considering the power output by the kite when applied to a moving ship, with further investigation to establish the reductions that might occur due to the influence of the kite on ship resistance characteristics and ship machinery.

References

Abbott, I. H. & Doenhoff, A. E., 1959. *Theory of Wing Sections*, Dover Publications.

Alexander, K. & Stevenson, J., 2001. A test rig for kite performance measurement, *Proceedings of the Institution of Mechanical Engineers Part B-Journal of Engineering Manufacture*, **215**(4), 595–598.

Alexander, K. & Stevenson, J., 2001. Kite equilibrium and bridle length, *Aeronautical Journal*, **105**(1051), 535–541.

Beer, T., 1997. *Environmental oceanography*, CRC Press.

Bradbury, W., 1985. An experimental investigation of the flow past hulls at leeway, *Journal of Wind Engineering and Industrial Aerodynamics*, **20**, 227–263.

Breukels, J. & Ockels, W., 2007. Design of a large inflatable kite plane, in *48th AIAA/ASME/ASCE/AHS/ASC Structures, Structural Dynamics, and Materials Conference*.

Bryant, L. W. & Brown, W. S., 1942. Collected researches on the stability of kites and towed gliders, *National Physics Lab.*, Rept. 2303.

Burton, T., Sharpe, D., Jenkins, N., & Bossanyi, E., 2001. *Wind energy handbook*, John Wiley and Sons Ltd.

Buxton, I. L., 1971. Engineering economics and ship design, Tech. rep., The British Ship esearch ASsociation, Wallsend Research Station, Wallsend, Tyne and Wear, NE286UY.

Calvert, J. R. & Farrar, R. A., 1999. *An Engineering Data book*, Palgrave Macmillan, New York.

Chapman, T., 2009. Operational aspects of kite auxiliary propulsion systems for merchant vessels, *Southampton University Masters Thesis*, Southampton, Hampshire, GB, SO171BJ.

Claughton, A. R., Shenoi, R. A., & Wellicome, J. F., 1998. *Sailing Yacht Design Theory*, vol. 1, Addison Wesley Longman.

Comstock, J., 1967. *Principles of Naval Architecture*, The Society of Naval Architects Marine Engineers.

Crowdy, E., 1980. The economics of sail, in *Symposium on Wind Propulsion of Commercial Ships*, pp. 51–65, The Royal Institution of Naval Architects.

Dadd, G. M., 2005. Development and validation of a testrig for kite performance, *Southampton University Masters Thesis, GB*, Southampton, Hampshire, GB, SO171BJ.

Duckworth, R., 1985. The application of elevated sails for fuel saving auxiliary propulsion of commercial vessels, *Proceedings of the International Symposium on Windship Technology, Southampton, U.K*, (Part B), 297–315.

Erhard, M. & Struch, H., 2012. Control of towing kites for seagoing vessels, *Cornell University e-prints*, (arXiv:1202.3641v1), 1–10.

Gill, A., 1979. The analysis and synthesis of ship manoeuvring, *Royal Institution of Naval Architects*, **121**(1), 209–220.

Green, R. & McD Galbraith, R., 1985. Dynamic recovery to fully attached aerofoil flow from deep stall, *AIAA Journal*, **33**(8), 1433–1443.

Hobbs, S. E., 1986. *A Quantitative Study of Kite Performance in Natural Wind with Application to Kite Anemometry*, Ph.D. thesis, Ecological Physics Research Group, Cranfield Institute of Technology.

Hoerner, S. F., 1965. *Fluid Dynamic Drag: Practical Information on Aerodynamic Drag and Hydrodynamic Resistance*, Hoerner Fluid Dynamics (Jun 1993).

Jackson, P. S., 2005. Optimal loading of a tension kite, *AIAA Journal*, **43**(11), 2273–2278, doi:10.2514/1.3543.

Lansdorp, B., 2005. Design of a 100mw laddermill for wind energy generation from 5km altitude, in *7th World Congress on Recovery*, Recycling and Reintegration, Beijing.

LighthousePress, 2001. Atlas of pilot charts: North atlantic ocean, *National Imagery and Mapping Agency*, **1**, 1–12, NVPUP 106.

Lloyd, M. L., 1980. Crosswind kite power (for large-scale wind power production), *AIAA Journal of Energy*, **4**, 106–111.

Mathworks, 2009. Matlab, mathmatics laboratory, software package.

Mcroskey, W., 1982. Unsteady airfoils, *Ann. Rev. Fluid Mech*, **14**, 285–309.

Molland, A. & Hawksley, G., 1985. An investigation of propeller performance and machinery applications in wind assisted ships, *Proceedings of the International Symposium on Windship Technology*, **4**, 143–168.

Molland, A., Turnock, S., & Hudson, D., 2011. *Ship Resistance and Propulsion, Practical Estimation of Ship propulsive Power*, Cambridge University Press, NY 10013-2473, USA.

Naaijen, P, K. V. & Dallinga, R. P., 2006. On the power savings by an auxiliary kite propulsion system, *International Shipbuilding Progress*, **53**(2-3), 255.

Ockels, W. J., 2001. Laddermill, a novel concept to exploit the energy in the airspace, *Aircraft Design*, **4**, 81–97, doi:10.1016/S1369-8869(01)00002-7.

Podgaets, A. R. & Ockels, W. J., 2006. Three dimensional simulation of a laddermill, in *Proceedings of the Third Asian Wind Power Conference*, pp. 116–121, Wind Power Asia, Beijing.

Schlaak, M., Kreutzer, R., & Elsner, R., 2009. Simulating possible savings of the skysails-system on international merchant ship fleets, *Transactions of the Royal Institution of Naval Architects, Part A International Journal of Maritime Technology*, **151**(A4), 207–219, doi:10.3940/rina.ijme.2009.a4.161.

Sharma & Bellows, G., 1976. Experiments on the wavemaking of a drifting ship, *International seminar on wave resistance*, pp. 369–372.

Stevenson, J., Alexander, K., & Lynn, P., 2005. Kite performance testing by flying in a circle, *Aeronautical Journal*, **109**(1096), 269–276.

Stevenson, J. C. & Alexander, K. V., 2006. Circular flight kite tests: converting to standard results, *Aeronautical Journal*, **110**(1111), 605–614.

Tangler, J. L., 1984. Horizontal axis wind turbine post stall airfoil characteristics synthesization, SERI/TP-257-4400.

TheWeek, 2012. Cosing the strit of hormuz, *Magazine, The Week - the best of british and foreign media*, (857).

Wellicome, J. F., 1985. Some comments on the relative merits of various wind propulsion devices, *Journal of Wind Engineering and Industrial Aerodynamics*, **20**, 111–142.

Wellicome, J. F. & Wilkinson, S., 1984. Propulsive kites - an initial study, *Univ. of Southampton, Southampton, England, U.K.*, Rept. SSSU 19.

Wicker, L. & Fehlner, L., 1958. Characteristics of a family of low aspect ratio control surfaces, *DTMB Report 933*.

Williams, P., L. B. & Ockels, W., 2007. Flexible tethered kite with moveable attachement points, part ii: State and wind estimation, in *Atmospheric Flight Mechanics Conference and Exhibit*.

Williams, P., 2006. Optimal wind power extraction with a tethered kite, in *Guidance, navigation and Control Conference and Exhibit*, doi:10.2514/1.30089.

Williams, P., Lansdorp, B., & Ockels, W., 2007. Optimal trajectories for tethered kite mountd on a vertical axis generator, in *Modeling and Simulation Technologies Conference and Exhibit*.

Williams, P., Lansdorp, B., & Ockels, W., 2007. Optimal cross-wind towing and power generation with tethered kites, in *Guidance, Navigation and Control conference and Exhibit*.

Williams, P., Lansdorp, B., & Ockels, W., 2007. Modeling and control of a kite on a variable length flexible inelastic tether, in *Modeling and Simulation Technologies Confernce and Exhibit*.

Williams, P., Lansdorp, B., & Ockels, W., 2007. Flexible tethered kite with moveable attachment points part i: Dynamics and control, in *Atmospheric Flight Mechanics Conference and Exhibit*.

Wrage, S., 2007. Positioning device for a free-flying kite-type wind-attacked element in a wind-powered watercraft, *U.S. Patent No. 20007/0272141 A1*.

Wrage, S., 2007. Skysails technology information, SkySails GmbH, Veritaskai 3, 21079 Hamburg, Germany.

WUMTIA, 1986. Turbo ad, data aquisition, software package.

www.kiteship.com, 2012. Innovation in tethered flight.

www.oilprice.com, 2012. Historic oil price.

www.Skysails.com, 2012. Skysails company website.

Appendix A

Statistical Formulae

The statistical forumulae shown here are those which have been used in support of the arguments in this thesis. They are printed as quoted by Calvert & Farrar (1999).
The sample mean is given by

$$\bar{x} = \frac{1}{n} \sum x_i \tag{A.1}$$

The sample variance is

$$\sigma^2 = \frac{1}{n-1} \sum (x_i - \bar{x})^2 \tag{A.2}$$

The sample Standard Deviation is

$$\sigma \tag{A.3}$$

The 95% conficence limit is given by

$$\bar{x} \pm 1.96 \frac{\sigma}{\sqrt{n}} \tag{A.4}$$

The 99% confidence limit is given by

$$\bar{x} \pm 2.58 \frac{\sigma}{\sqrt{n}} \tag{A.5}$$

Appendix B

Data Tables for Fuel savings calculation

Table B.1 Frequency distribution of wind direction for selected wind roses along route in the month of April

LAT	LON	rose	N	NE	E	SE	S	SW	W	NW	CALM
37.5	-37.5	1	9	6	7	12	18	21	15	11	1
37.5	-42.5	2	9	6	6	9	18	21	17	13	1
37.5	-47.5	3	11	7	4	7	18	21	17	14	1
37.5	-52.5	4	12	8	5	6	16	20	17	15	1
37.5	-57.5	5	14	8	5	5	13	17	19	18	1
37.5	-62.5	6	15	8	7	3	12	14	18	22	1
37.5	-67.5	7	15	11	5	6	12	17	15	18	1
37.5	-72.5	8	14	11	8	7	15	17	12	13	3
42.5	-12.5	9	22	18	6	4	7	13	13	15	2
42.5	-17.5	10	13	14	9	7	10	15	16	15	1
42.5	-22.5	11	12	10	8	8	12	17	17	15	1
42.5	-27.5	12	9	7	9	11	16	18	15	14	1
42.5	-32.5	13	7	6	6	10	17	20	18	15	1
42.5	-37.5	14	10	7	6	9	17	18	17	15	1
42.5	-42.5	15	10	5	6	9	17	17	18	17	1
42.5	-47.5	16	13	7	7	9	17	16	15	15	1
47.5	-12.5	17	13	12	9	8	11	15	16	15	1
47.5	-7.5	18	14	16	11	6	8	14	14	15	2
52.5	-7.5	19	11	12	8	9	14	15	15	14	2

Table B.2 Frequency distribution of wind direction for selected wind roses along route in the month of July

LAT	LON	rose	N	NE	E	SE	S	SW	W	NW	CALM
37.5	-37.5	1	9	10	11	9	12	20	14	9	6
37.5	-42.5	2	7	7	10	9	16	22	16	8	5
37.5	-47.5	3	7	7	7	8	18	26	16	7	4
37.5	-42.5	4	7	7	10	9	16	22	16	8	5
37.5	-57.5	5	5	4	5	6	19	32	21	6	2
37.5	-62.5	6	6	5	4	5	19	32	19	8	2
37.5	-67.5	7	7	8	6	6	16	30	17	7	3
37.5	-72.5	8	7	10	8	7	20	28	12	5	3
42.5	-12.5	9	29	15	4	4	3	9	14	20	2
42.5	-17.5	10	20	15	4	4	5	13	17	20	2
42.5	-22.5	11	15	13	5	4	6	16	19	19	3
42.5	-27.5	12	11	9	7	6	9	18	19	17	4
42.5	-32.5	13	9	8	8	8	13	22	17	12	3
42.5	-37.5	14	7	6	7	8	16	25	17	11	3
42.5	-42.5	15	7	5	5	7	19	28	18	9	2
42.5	-47.5	16	6	5	6	8	22	27	14	8	4
47.5	-12.5	17	14	9	5	4	8	16	22	20	2
47.5	-7.5	18	14	12	6	4	7	16	19	19	3
52.5	-7.5	19	10	6	5	5	12	20	23	16	3

Table B.3 Frequency distribution of wind direction for selected wind roses along route in the month of October

LAT	LON	rose	N	NE	E	SE	S	SW	W	NW	CALM
37.5	-37.5	1	13	12	10	9	14	16	12	13	1
37.5	-42.5	2	13	11	10	8	14	17	14	12	1
37.5	-47.5	3	13	12	9	9	15	16	12	12	2
37.5	-52.5		14	11	9	7	15	16	15	12	1
37.5	-57.5	5	13	10	9	8	14	16	15	13	2
37.5	-62.5	6	15	10	9	8	14	12	14	16	2
37.5	-67.5	7	9	17	11	8	10	12	14	17	2
37.5	-72.5	8	18	17	11	7	9	10	11	15	2
42.5	-12.5	9	18	17	7	6	9	13	13	15	2
42.5	-17.5	10	13	10	8	8	12	15	15	17	2
42.5	-22.5	11	15	9	8	9	12	16	13	17	1
42.5	-27.5	12	13	9	8	8	12	16	16	17	1
42.5	-32.5	13	12	8	8	9	14	15	16	17	1
42.5	-37.5	14	13	10	8	7	14	15	15	17	1
42.5	-42.5	15	13	9	8	7	13	12	18	19	1
42.5	-47.5	16	16	9	8	8	12	12	15	19	1
47.5	-12.5	17	11	9	10	9	13	15	17	15	1
47.5	-7.5	18	9	10	12	10	10	16	16	15	2
52.5	-7.5	19	10	6	8	10	14	16	19	15	1

Table B.4 Frequency distribution of wind direction for selected wind roses along route in the month of Janruary

LAT	LON	rose	N	NE	E	SE	S	SW	W	NW	CALM
37.5	-37.5	1	10	7	7	8	15	21	17	14	1
37.5	-42.5	2	10	6	5	7	14	21	19	17	1
37.5	-47.5	3	13	6	5	6	14	19	19	18	0
37.5	-52.5		12	6	4	5	13	18	22	20	0
37.5	-57.5	5	13	6	5	6	12	15	22	21	0
37.5	-62.5	6	15	6	4	6	11	13	20	24	1
37.5	-67.5	7	17	8	6	4	9	11	20	24	1
37.5	-72.5	8	19	8	5	4	9	13	15	26	1
42.5	-12.5	9	11	12	7	7	14	19	16	12	2
42.5	-17.5	10	7	7	7	10	15	21	19	13	1
42.5	-22.5	11	7	5	6	11	17	21	19	13	1
42.5	-27.5	12	7	6	6	10	17	21	19	13	1
42.5	-32.5	13	9	5	5	8	16	21	20	15	1
42.5	-37.5	14	9	6	6	8	15	18	20	18	0
42.5	-42.5	15	11	7	4	6	13	14	22	23	0
42.5	-47.5	16	12	6	6	8	15	11	18	23	1
47.5	-12.5	17	7	5	8	10	15	21	20	13	1
47.5	-7.5	18	8	8	9	9	13	20	18	14	1
52.5	-7.5	19	7	6	8	8	16	21	21	13	0

Table B.5 Wind speed [ms-1] at 10m altitude for selected wind roses along route in the month of April

LAT	LON	rose	N	NE	E	SE	S	SW	W	NW
37.5	-37.5	1	6.69	6.69	6.69	6.69	6.69	6.69	9.35	9.35
37.5	-42.5	2	6.69	6.69	6.69	6.69	6.69	9.35	9.35	9.35
37.5	-47.5	3	6.69	6.69	6.69	6.69	9.35	9.35	9.35	9.35
37.5	-52.5	4	9.35	6.69	6.69	6.69	9.35	9.35	9.35	9.35
37.5	-57.5	5	9.35	6.69	6.69	6.69	9.35	9.35	9.35	9.35
37.5	-62.5	6	9.35	6.69	6.69	6.69	9.35	9.35	9.35	9.35
37.5	-67.5	7	9.35	6.69	6.69	6.69	9.35	9.35	9.35	9.35
37.5	-72.5	8	6.69	6.69	6.69	6.69	6.69	6.69	6.69	6.69
42.5	-12.5	9	6.69	9.35	6.69	6.69	6.69	6.69	6.69	6.69
42.5	-17.5	10	6.69	6.69	6.69	6.69	6.69	9.35	9.35	9.35
42.5	-22.5	11	6.69	6.69	6.69	6.69	6.69	6.69	9.35	9.35
42.5	-27.5	12	6.69	6.69	6.69	6.69	6.69	9.35	9.35	9.35
42.5	-32.5	13	6.69	6.69	6.69	6.69	9.35	9.35	9.35	9.35
42.5	-37.5	14	9.35	6.69	6.69	6.69	9.35	9.35	9.35	9.35
42.5	-42.5	15	9.35	6.69	6.69	9.35	9.35	9.35	9.35	9.35
42.5	-47.5	16	9.35	6.69	6.69	6.69	6.69	9.35	9.35	9.35
47.5	-12.5	17	6.69	6.69	6.69	6.69	6.69	9.35	9.35	9.35
47.5	-7.5	18	6.69	6.69	6.69	6.69	6.69	6.69	6.69	6.69
52.5	-7.5	19	6.69	6.69	6.69	6.69	6.69	6.69	6.69	6.69

Table B.6 Wind speed [ms-1] at 10m altitude for selected wind roses along route in the month of July

LAT	LON	rose	N	NE	E	SE	S	SW	W	NW
37.5	-37.5	1	4.34	4.34	2.36	2.36	4.34	4.34	4.34	4.34
37.5	-42.5	2	4.34	4.34	4.34	4.34	4.34	6.69	2.36	2.36
37.5	-47.5	3	4.34	4.34	4.34	4.34	6.69	6.69	6.69	4.34
37.5	-42.5	4	4.34	4.34	4.34	4.34	4.34	6.69	2.36	2.36
37.5	-57.5	5	6.69	4.34	4.34	4.34	6.69	6.69	6.69	6.69
37.5	-62.5	6	6.69	4.34	2.36	4.34	6.69	6.69	6.69	6.69
37.5	-67.5	7	6.69	6.69	4.34	4.34	6.69	6.69	6.69	6.69
37.5	-72.5	8	4.34	6.69	4.34	6.69	6.69	6.69	2.36	4.34
42.5	-12.5	9	5.47	6.69	2.36	4.34	6.69	6.69	5.47	6.69
42.5	-17.5	10	6.69	6.69	4.34	4.34	6.69	6.69	6.69	6.69
42.5	-22.5	11	6.69	4.34	2.36	4.34	4.34	6.69	6.69	6.69
42.5	-27.5	12	4.34	4.34	4.34	4.34	6.69	6.69	6.69	6.69
42.5	-32.5	13	6.69	4.34	4.34	4.34	6.69	6.69	6.69	6.69
42.5	-37.5	14	6.69	4.34	4.34	4.34	6.69	6.69	6.69	6.69
42.5	-42.5	15	6.69	6.69	4.34	4.34	6.69	6.69	6.69	6.69
42.5	-47.5	16	4.34	6.69	4.34	4.34	6.69	6.69	6.69	6.69
47.5	-12.5	17	6.69	6.69	4.34	4.34	6.69	6.69	6.69	6.69
47.5	-7.5	18	4.34	4.34	4.34	4.34	6.69	6.69	6.69	6.69
52.5	-7.5	19	4.34	4.34	4.34	6.69	6.69	6.69	6.69	6.69

Table B.7 Wind speed [ms-1] at 10m altitude for selected wind roses along route in the month of October

LAT	LON	rose	N	NE	E	SE	S	SW	W	NW
37.5	-37.5	1	6.69	6.69	6.69	6.69	6.69	6.69	6.69	9.35
37.5	-42.5	2	6.69	6.69	6.69	6.69	6.69	6.69	6.69	9.35
37.5	-47.5	3	9.35	6.69	6.69	6.69	6.69	6.69	6.69	9.35
37.5	-52.5	4	9.35	6.69	6.69	6.69	6.69	6.69	9.35	9.35
37.5	-57.5	5	9.35	6.69	6.69	6.69	6.69	9.35	9.35	9.35
37.5	-62.5	6	9.35	6.69	6.69	6.69	6.69	9.35	9.35	9.35
37.5	-67.5	7	6.69	6.69	6.69	6.69	6.69	6.69	6.69	9.35
37.5	-72.5	8	6.69	6.69	6.69	6.69	6.69	6.69	6.69	6.69
42.5	-12.5	9	6.69	6.69	6.69	6.69	6.69	6.69	6.69	6.69
42.5	-17.5	10	6.69	6.69	6.69	6.69	6.69	6.69	9.35	9.35
42.5	-22.5	11	6.69	6.69	6.69	6.69	6.69	9.35	9.35	9.35
42.5	-27.5	12	9.35	6.69	6.69	6.69	6.69	9.35	9.35	9.35
42.5	-32.5	13	9.35	6.69	6.69	6.69	9.35	9.35	9.35	9.35
42.5	-37.5	14	9.35	9.35	6.69	6.69	9.35	9.35	9.35	9.35
42.5	-42.5	15	9.35	9.35	6.69	6.69	9.35	9.35	9.35	9.35
42.5	-47.5	16	9.35	6.69	6.69	6.69	6.69	6.69	9.35	9.35
47.5	-12.5	17	9.35	6.69	6.69	6.69	6.69	9.35	9.35	9.35
47.5	-7.5	18	6.69	6.69	6.69	6.69	6.69	6.69	9.35	9.35
52.5	-7.5	19	9.35	6.69	6.69	6.69	9.35	9.35	9.35	9.35

Table B.8 Wind speed [ms-1] at 10m altitude for selected wind roses along route in the month of Janruary

LAT	LON	rose	N	NE	E	SE	S	SW	W	NW
37.5	-37.5	1	9.35	9.35	6.69	6.69	9.35	9.35	9.35	12.29
37.5	-42.5	2	9.35	9.35	6.69	6.69	9.35	12.29	12.29	12.29
37.5	-47.5	3	9.35	9.35	6.69	6.69	9.35	12.29	12.29	12.29
37.5	-52.5	4	9.35	6.69	6.69	6.69	12.29	12.29	12.29	12.29
37.5	-57.5	5	9.35	9.35	6.69	9.35	12.29	12.29	12.29	12.29
37.5	-62.5	6	9.35	9.35	6.69	9.35	9.35	12.29	12.29	12.29
37.5	-67.5	7	9.35	6.69	6.69	6.69	9.35	12.29	12.29	12.29
37.5	-72.5	8	9.35	6.69	6.69	6.69	6.69	9.35	9.35	9.35
42.5	-12.5	9	6.69	6.69	6.69	6.69	9.35	9.35	9.35	9.35
42.5	-17.5	10	9.35	6.69	6.69	6.69	9.35	9.35	9.35	9.35
42.5	-22.5	11	9.35	6.69	6.69	6.69	9.35	9.35	9.35	9.35
42.5	-27.5	12	9.35	6.69	6.69	9.35	9.35	6.69	6.69	9.35
42.5	-32.5	13	9.35	6.69	6.69	9.35	9.35	12.29	12.29	12.29
42.5	-37.5	14	9.35	9.35	9.35	9.35	12.29	12.29	12.29	12.29
42.5	-42.5	15	12.29	9.35	6.69	9.35	12.29	12.29	12.29	12.29
42.5	-47.5	16	9.35	9.35	6.69	9.35	9.35	9.35	12.29	12.29
47.5	-12.5	17	9.35	6.69	9.35	9.35	9.35	9.35	12.29	9.35
47.5	-7.5	18	9.35	6.69	6.69	6.69	9.35	9.35	9.35	9.35
52.5	-7.5	19	6.69	6.69	9.35	6.69	9.35	9.35	9.35	9.35

Table B.9 Inputs for investigating influence of kite input parameters on effective thrust

DATE	LAT [N] DEG [°]	LAT [N] MIN [']	LON DEG[°]	LON MIN [°‘]	LON E/W	V_S [KTS]	V_T [BFort]	γ_C [ROSE]	γ [°]	β_S [°]	V_A [ms^{-1}]
THU 22ND APR	55	8.8	4	22.3	W	16.5	2	S	40	8.4	10.4
FRI 23RD APR	54	8.3	5	8.5	W	15.7	4	SSW	-19.5	-8.8	14.6
	53	6.3	5	14.1	W	16	2	S	2	0.4	10.6
	52	2.5	5	54.3	W	16.5	2.5	SW	-5	-1.4	11.8
	51	14.6	6	57.4	W	15.3	3	SSW	17.5	6.2	12.1
	50	34.7	7	32.6	W	15.1	3	SW	-11	-3.9	12.1
	49	46	8	26.8	W	15.8	3	S	35	12	11.9
SAT 24TH APR	48	53.1	10	1.9	W	13.8	3	S	38	14.3	10.9
	48	6.2	10	13.5	W	13.8	5	S	35	20	15.7
	47	30.8	10	50.7	W	9.2	6	S	35	25.5	16.4
	46	50.6	11	30.4	W	12.6	5	SW	-8	-4.7	15.8
	46	17	12	6.6	W	12.4	5	SW	-10	-5.9	15.7
	45	31.8	12	52	W	12.7	6	SW	-8	-5.2	18.8
SUN 25TH APR	44	39.9	13	44.1	W	12.5	4	SW	-11	-5.6	13.1
	43	59.6	14	24.4	W	12	4	SW	-7	-3.6	12.8
	43	20.6	14	49.7	W	9.9	4	S	-20	-11.4	11.6
	43	8.6	15	28.8	W	8.3	4	S	96	61.8	7.6
	43	19.7	15	32.7	W	12.3	5	S	-180	-180	3
	43	12.2	16	25.1	W	11.1	4.5	S	90	54.4	9.8
MON 26TH APR	44	39.9	13	44.1	W	12.5	4	SW	-11	-5.6	13.1
-	43	59.6	14	24.4	W	12	4	SW	-7	-3.6	12.8
-	43	20.6	14	49.7	W	9.9	4	S	-20	-11.4	11.6
-	43	8.6	15	28.8	W	8.3	4	S	96	61.8	7.6
-	43	19.7	15	32.7	W	12.3	5	S	-180	-180	3
-	43	12.2	16	25.1	W	11.1	4.5	S	90	54.4	9.8

DATE	LAT [N] DEG [°]	LAT [N] MIN [']	LON DEG[°]	LON MIN [°']	LON E/W	V_S [KTS]	V_T [BFort]	γ_C [ROSE]	γ [°]	β_S [°]	V_A [ms^{-1}]
TUE 27TH APR	42	27.4	20	34.6	W	15.7	4.5	S	102	50.6	10.1
	42	34.4	21	49.5	W	10.2	6	S	83	61.1	13.9
	42	35.7	22	19	W	8.7	6.7	S	80	63.9	15.9
	42	30.6	23	10.4	W	11.5	5	WSW	12.5	7.7	15.2
	42	22.8	24	4.9	W	10.6	5	W	-15	-9.5	14.7
	42	12.5	24	52.7	W	6.5	5	W	-23	-17	12.5
WED 28TH APR	42	6	25	32.6	W	5.5	4.5	NW	-68	-51.8	9.4
	42	9	26	17.9	W	10	4	W	42	23.9	11.1
	42	24.8	26	45.5	W	8.8	3	W	-62	-30.3	7.6
	42	2	27	11.6	W	8.5	5	SW	29	19.9	13.3
	42	15.1	27	5	W	13.5	5	W	20	11.5	16
	41	54.5	28	14.1	W	6.5	4	SW	-10	-6.7	10
THU 29TH APR	42	5	28	25.8	W	10	5	WSW	98.5	67.9	10
	42	2.7	29	21.7	W	9.8	6	W	18	12.8	17.2
	42	21.4	30	3.6	W	11.5	6	W	20	13.5	18
	42	8.4	30	36.4	W	10.3	5	WNW	-97.5	-66.2	10.1
	41	50.7	31	27	W	14.5	4	W	-59	-27.7	12.3
	40	59.6	32	8	W	14.8	2	W	-30	-7	9.7
FRI 30TH APR	41	14.4	32	11.8	W	16.5	3	SW	-24	-8.1	12.6
	40	55.8	31	46	W	16.4	4	SW	16	7.1	15
	40	41.4	32	34.4	W	10.2	3	SW	45	20.2	8.9
	40	37.2	33	28.5	W	8.4	5	SW	-9	-6.2	13.6
	40	36	34	36.5	W	13	4	SSW	67.5	33.8	11.1
	40	36.3	35	18.2	W	10.8	5	SW	45	28.5	13.9

DATE	LAT [N] DEG [°]	LAT [N] MIN [']	LON DEG[°]	LON MIN [°']	LON E/W	V_S [KTS]	V_T [BFort]	γ_C [ROSE]	γ [°]	β_S [°]	V_A [ms^{-1}]
SAT 1ST MAY	40	40.2	36	54	W	10.4	6.5	SSE	113.5	90.8	12.7
	40	38	37	7.8	W	11.1	4	W	-19	-10.3	12.2
	40	35.5	37	21.3	W	11.5	4	SW	-155	-92.9	2.8
	40	20.7	37	49.3	W	10.1	5	S	100	68.8	9.9
	40	24.4	38	49.8	W	11.8	5	S	100	64.2	10.2
	40	28.8	39	28.8	W	8.6	6	S	90	70.2	13.1
SUN 2ND MAY	40	28.7	40	29.4	W	8.3	6	S	94	74.4	12.7
	40	37.7	40	39.7	W	10.5	2	S	-110	-25.8	5.1
	40	34.3	41	30	W	12.2	4	NE	-145	-78.2	3.9
	40	20.4	42	23.1	W	15.5	5	S	80	43.8	13.3
	40	9	43	35.4	W	11.2	4	NW	-59	-31.9	10.8
	39	58	44	29.2	W	12.1	4	NW	-55	-28.6	11.5
MON 03 MAY	39	53.3	45	31.4	W	15.1	3	N	-74	-25	9.9
	40	17.6	45	34.2	W	6	4	W	96	70.2	7.1
	40	44.8	45	44.7	W	9.3	6	NE	-73	-54.5	14.4
	41	10	46	9.8	W	13.8	5	NW	60	34.5	14.3
	41	20.7	46	47.4	W	7.7	4	NW	-69	-44.5	8.9
	41	3.1	47	17.8	W	12.1	2	NW	-45	-11.9	8.1
TUE 4TH MAY	40	47	46	46.1	W	9.1	3	S	-9	-4.3	9
	40	19.4	47	8.6	W	9.7	4	S	67	39	9.8
	39	44.9	47	12	W	13.5	3	SW	-25	-9.6	11
	39	21	47	40.2	W	13.7	5.5	W	-60	-36.9	15.6
	38	56.3	48	19.2	W	12	7	W	-2	-1.4	21.6
	39	7.8	48	24.6	W	13	7	W	-10	-7	22.1

DATE	LAT [N] DEG [°]	LAT [N] MIN [']	LON DEG[°]	LON MIN [°']	LON E/W	V_S [KTS]	V_T [BFort]	γ_C [ROSE]	γ [°]	β_S [°]	V_A [ms^{-1}]
WED 5TH MAY	39	48.8	49	26	W	13.8	5.5	N	-37	-22.4	17
	40	2.5	50	14.6	W	10.6	6	W	-6	-4.2	17.7
	40	5.2	51	12	W	11.5	5	W	0	0	15.3
	39	39.3	52	7	W	14.9	5	NW	-118	-68.4	8.9
	38	49.1	52	13	W	16.8	5	W	-89	-46.7	12.8
	38	17.8	52	29.1	W	13.5	6	W	120	85.7	10.7
THU 6TH MAY	38	32.5	52	44.6	W	12.2	5	WNW	-27.5	-16.5	15.2
	38	30.4	53	41.3	W	11.5	6	WNW	-25.5	-17.3	17.8
	38	38	54	44.5	W	14.2	3	SW	60	21.6	10.2
	38	51.6	55	46.7	W	12.6	4.5	NW	-46	-25.5	13.3
	38	49.5	56	58.1	W	16	5	W	-2	-1.1	17.6
	38	53.7	58	21.7	W	15.4	4	W	-5	-2.3	14.6
FRIDAY 7TH MAY	38	52	59	41.4	W	17.4	6.5	SW	44	27	21.2
	38	48.8	61	0	W	15.6	9	SW	29	21.5	29.8
	38	33.5	62	12.6	W	12.7	6	W	-32	-21	18.2
	38	18.3	63	5.1	W	12	5	W	55	33.6	13.8
	38	15.4	63	59.3	W	16.8	5	W	-89	-46.7	12.8
	38	17.8	64	29.1	W	10.3	5	W	0	0	14.7
SAT 8TH MAY	37	43	65	12.4	W	9.2	6	SW	144.2	126.1	8.9
	37	17.7	65	35.9	W	8.8	5	SW	143.8	118.6	6.3
	36	57.5	65	54.5	W	14.1	3	SW	149.1	32.3	4.2
	36	41.6	66	10.1	W	12.6	3.5	W	102.6	45.3	7.5
	36	27.4	66	34.4	W	11.7	4	SW	146.7	83.3	3.7
	36	21.5	67	2.3	W	11.6	5	SW	146.6	109.6	5.5

DATE	LAT [N] DEG [°]	LAT [N] MIN [']	LON DEG[°]	LON MIN [°']	LON E/W	V_S [KTS]	V_T [BFort]	γ_C [ROSE]	γ [°]	β_S [°]	V_A [ms^{-1}]
SUN 9TH MAY	36	26.1	67	39.9	W	10	3	N	-134	-55.8	3.8
	36	29.2	68	13.6	W	9.4	1	NW	-122	-9.2	4.5
	36	33	68	54.2	W	6.4	3	NW	-25	-14.2	7.5
	36	28.8	69	48.2	W	6	6	NW	-38	-30.6	14.8
	36	15.7	70	30.7	W	7.7	6	NW	-92	-74	12.8
	36	14.2	71	5.8	W	6.7	7	NW	-35	-28.8	18.4
MON 10TH MAY	36	14.6	71	45.9	W	7.1	5.5	NNW	-65.5	-50.4	12.7
	36	25.2	71	58.7	W	8.4	5	NNW	-63.5	-44.6	11.9
	36	32.8	72	31	W	7.7	6	SW	55	42.4	14.9
	37	2.6	72	41.4	W	13.6	6	NW	-68	-44.5	16.3
	37	0.8	73	19	W	7	5	NW	-70	-52.3	11.1
	36	53.2	74	18.7	W	8	5	NW	-50	-35.3	12.4
TUE 11 MAY	36	43.2	75	14.3	W	10	2.5	NE	171	15.3	2
	36	50.4	75	24.1	W	11.5	0	NaN	-94	0	5.9
	36	58	76	20.2	W	7.8	0	NaN	-173	0	4
SECURE PORT SIDE PIER 5 NORFOLK NAVAL STN											